THE UNIVERSITY OF OKLAHOMA

GRADUATE COLLEGE

AUTOMATION OF ADVANCED SCANNERS FOR RF METROLOGY

A THESIS

SUBMITTED TO THE GRADUATE FACULTY

in partial fulfillment of the requirements for the

Degree of

MASTER OF SCIENCE

By

TOM BRACHTENBACH
Norman, Oklahoma
2020

AUTOMATION OF ADVANCED SCANNERS FOR RF METROLOGY

A THESIS APPROVED FOR THE
SCHOOL OF ELECTRICAL AND COMPUTER ENGINEERING

BY THE COMMITTEE CONSISTING OF

Dr. Jorge L. Salazar-Cerreño, Chair

Dr. Mark Yeary

Dr. Zeeshan Qamar

# Acknowledgements

I would like to thank everyone that helped me in the writing of this thesis. I would like to thank my advisor, Dr. Jorge Salazar-Cerreño, who took a chance on me when I was an undergraduate student and has never stopped believing in and supporting me. I want to thank Dr. Zeeshan Qamar, without his tireless effort and assistance I would not have been able to complete my work. Thanks to Alex Stringer and Joel Love for the work that they did on the original anisotropic scanner, I am grateful for the wonderful job they did that made my project much more doable. I would like to thank all the other current and former members of the PAARD, who I have enjoyed working with immensely and whose collaboration and help was invaluable in completing this work. This includes Dr. Nafati Aboserwal, Dr. Rodrigo Lebron, Jose Diaz, Arturo Umeyama, Javier Ortiz, Kevin Constien, Nim Ccoillo, Alex Oblitas, Syed Jehangir, and Jesus Roque.

I would also like to dedicate this thesis to my family. My parents, Darin and Corrine, and my sister Molly have supported me throughout my time in school, and without their encouragement I would not have been able to complete this work. Thank you so much for the love, wisdom, and guidance you shared with me, I am forever grateful.

# Table of Contents

# List Of Figures

# List Of Tables

# Abstract

The characterization of the constitutive properties of materials is an important step in the development of modern RF devices, especially at mm-wave frequencies or in systems that incorporate materials whose performance varies with frequency or the angle of the impinging electrical field. This thesis discusses the implementation of three material characterization systems designed by the Phased Array Antenna Research and Development (PAARD) group at the Advanced Radar Research Center (ARRC) for taking material measurements under different test configurations. For each system, the majority of the work done was in creating a graphic user interface (GUI) in Labview that would facilitate rapid measurements by providing an intuitive control software for the user. The three systems work for a variety of different applications: an S-band waveguide setup for measuring isotropic materials, a C-band three-probe free-space system for measuring anisotropic materials, and a W-band free-space system. All three systems utilize the Nicolson-Ross-Weir (NRW) or Smith algorithm for material parameter extraction. Various other methods exist for material characterization but the NRW method provides relatively precise measurements over a broad band with minimal computational requirements. The importance of material parameters and the definitions of isotropy/anisotropy will be discussed first, followed by the method through which the material parameters are calculated. After this the specifications for each system that was developed are discussed including the physical test setup, the algorithm(s) that are used, the formation of the control software, the calibration techniques used, and the results of material tests.

# Chapter 1

# Introduction

## 1.1 Motivation

As technology has improved in the field of radio engineering and systems operate at increasingly higher frequencies designs require better performance in a smaller package. This has led engineers to carefully consider the performance of the substrates used in RF devices and antennas, as well as manipulate materials to operate optimally over a frequency or angular range. By introducing anisotropic or frequency-selective behavior into a dielectric, engineers can meet more stringent requirements or create heretofore unrealizable devices. A byproduct of these new material technologies is the necessity for material-characterization systems that can provide accurate and timely measurements over the frequency band of interest. In each case, the performance of the materials is quantified by its electric permittivity and magnetic permeability, both of which are important considerations for engineers designing an RF device. When using the NRW method, these two parameters are extracted from the transmitted and reflected components of an incident electromagnetic wave. The three characterization systems that will be discussed each cover a different band and are specialized for a specific application. One of the scanners, the three-probe anisotropic scanner, was previously designed by Alex Stringer [2] and upgraded by Joel Love [10]. The author's

primary contribution to this system was the control software that transformed this system from a specialized tool usable only with a thorough understanding of its operation and consultation with an instruction manual to a system that is ubiquitous at the ARRC. The mm-wave scanner was originally designed for characterization and calibration of automotive radar, and the author modified its software to allow for material measurements in addition to its original functionality. The waveguide setup was implemented by the author and other members of the PAARD group specifically for material characterization. For each of these systems an emphasis was placed on ease of use, expedited measurements, and reliability.

## 1.2    Literature Review

Determining the constitutive parameters of a material, the complex permittivity and permeability, is paramount for understanding how electromagnetic waves will propagate through it. Measuring the permittivity and permeability also allows for the calculation of the electric and magnetic loss tangents; respectively, which are defined as the ratio of the imaginary and real component of the parameter and indicate the amount of energy that will be dissipated in the material [1].

For most materials the behavior is assumed to be constant as the angle of an impinging electromagnetic wave varies. These are known as isotropic materials. The characterization procedure for these materials is straight forward and there are a multitude of methods that can be used to extract the material parameters [11]. These

include the free-space transmission/reflection method [6, 12, 13] , guided wave transmission/reflection [14] [15], the inductance/capacitance method [16], and the resonant method [17]. The transmission line method is particularly commonly used due to its relative ease of implementation and the broad frequency band it can operate over [18].

However not all materials behave in this manner. Some materials have constitutive parameters that depend directly on the direction of the impinging field, and these are known as anisotropic materials [7]. Instead of being able to reduce the permittivity and permeability to a single number, each value instead reduces to a $3x3$ tensor that relates the x-y-z direction of the applied field to a parameter value. While examples of this behavior can be found in nature, such as in crystaline structures and ionized gases, the majority of materials with this property are engineered to behave in this way.

Materials can also be described as dispersive, which means that its constitutive parameters vary with respect to the frequency of the applied field [7] [19]. Any material that displays properties that are not normally found in nature can be referred to as "metamaterials," and the study of their potential applications in RF have been growing in popularity with examples such as [20], [21], and [22]. One of the first investigations into materials with such abnormal behavior was done by V.G Veselago, who explored the theoretical behavior of substances with a negative permittivity and permeability in [23].

For these materials, there exist multiple methods to evaluate their parameters; but they all have trade-offs to consider when choosing which method to use [24].

These considerations include the space required and the environment in which the measurements are being taken, whether or not the characterization process leaves the material intact, the number of samples and measurements required, and the thickness of the material [25] [26] [27]. Methods exist for extracting material parameters from EM simulations [28], analytically [29], and from physical measurements [30] [31].

While the potential uses of these materials are exciting, their complex behavior presents several challenges to fully characterize them. Because these materials are designed to exhibit different performance over frequency and angle, the chosen measurement system must also be able to operate over a broad band and reliably change the angle of incidence [32] [33] [34].

For all three automated systems the transmission/reflection method, either guided or free-space, was chosen. When using this method the VNA used for measurements must be calibrated to provide accurate results. The calibration methods used are the transmission-reflection(TR), described in [13], and transmission-reflection-line (TRL), described in [35]. The procedures for calibration of VNAs is well documented, as discussed in [36], [37], and [38].

After the VNA is calibrated, the material parameter extraction algorithm can be applied. For all of the systems, the chosen method of material extraction was the Nicolson-Ross-Weir, described in [39] and [40], and the Smith algorithm [41]. These methods are easy to implement and are less computationally intensive than iterative methods. However, these methods can produce multiple solutions, which leads to uncertainty in the extracted results. This is particularly important when evaluating samples of a material that are electrically large ($t > \lambda/2$) [42] [34]. In these cases,

other methods can be applied, including the Kramers-Kronig integral [43] [44] [45], phase unwrapping [46] [47], and other iterative methods as discussed in [48] and [49].

Extraction of material parameters does not depend on the chosen algorithm alone. The hardware chosen as well as the software controlling it have a large effect on the quality and quantity of measurements. There are multiple examples of such systems in the literature that perform in a variety of ways. Some previously designed systems utilize specially made transmission line structures to characterize materials, such as [50] and [51], coaxial lines [52], and waveguides as discussed in [53] and [54]. Additionally, some systems have automated control software to allow for multiple or complex measurements to be taken with greater accuracy and repeatability such as in [55], [56], and [57].

## 1.3 Problem Statement

The key objective of this work is to create control software for each of the three material characterization systems to allow for rapid, convenient, and accurate measurements of material parameters. By creating multiple systems the goal is to facilitate measurements of a great variety of different materials over many frequency bands. The previous design of the anisotropic scanner allowed for measurements to be taken but the user interface was obtuse and forced a linear operation of the measurement, steps that wasted time. The main problem addressed is the need for convenient systems that can easily characterize a material, frequency selective surface, or radome

over a varied set of performance goals while providing highly accurate and repeatable results.

## 1.4 Contribution

The contributions by the author are detailed in this section. The author made user interfaces to control three material characterization systems that included controls for the calibration, execution, and display of measurements taken. The author performed an error analysis on potential sources of error found in the measurement systems. A new algorithm was implemented for the three-probe anisotropic scanner. A prototype waveguide transition was fabricated to explore expanding the variety of materials usable by the waveguide material characterization system. Finally, measurements were taken with each of the systems to verify functionality and accuracy.

## 1.5 Organization of the Thesis

The organization of the thesis is as follows: Chapter 2 will cover the background of the project, starting with a discussion of material properties and the importance of permittivity and permeability, as well as a definition of isotropy and anisotropy. This is followed by an examination of the most common material characterization processes in use today, including the resonance, waveguide, and free-space methods. Chapter 3 will cover the implementation of the rectangular waveguide based scanner will be discussed. This will encompass the system description, the algorithms used to extract material parameters, system calibration, and user interface development.

This is followed by an analysis of potential error sources in this system. Additionally, theoretical work done for the use of square waveguides for the characterization of anisotropic materials will be discussed. Chapter 4 will focus on the implementation of the two free-space scanners. It will follow a similar format as the previous chapter, with a review of the hardware setup, calibration methods, software design, and an overview of measured results. Finally, Chapter 5 will present conclusions about the project as well as propose possible areas for future work or improvements.

# Chapter 2

# Background

## 2.1   Introduction

This thesis primarily concerns the automation of three systems to characterize the constitutive parameters of materials. For this reason it is important to then first address how we define the different parameters we will be measuring, such as permittivity, permeability, dispersion, and isotropy/anisotropy as they will be discussed extensively herein. The ways that these parameters impact the performance of a material when used in an RF device is also discussed. Additionally, the theory behind commonly used material characterization methods will be examined.

## 2.2   Material Properties

### 2.2.1   Electrical Properties

The performance of a material when exposed to an electromagnetic wave can be described by its permittivity (commonly symbolized with $\epsilon$) and permeability (written as $\mu$). Materials that are used as dielectrics are composed of atoms whose positive and negative charges are "bound," that is they do not move freely through the material like they would in a conductor [7]. However, these charges can still reorient themselves

to align with an applied field, a process that results in a vast amount of infinitesimal dipoles. These two parameters, permittivity and permeability, then reflect the ability of those charges to align in a material when an electric or magnetic field impinges on it, respectively. Throughout this thesis when referring to these two they will be described relatively. For permittivity, this means that a given epsilon value will be the relative permittivity with respect to a vacuum. This is the fundamental constant $\epsilon_0 = 8.854 \times 10^{-12}$ (Farads/meter). The permeability of a vacuum is $\mu_0 = 4\pi \times 10^{-7}$ (Henries/meter). These two values are used when denoting the relative permittivity and permeability of a material, and they are written as:

$$\epsilon_r = \frac{\epsilon}{\epsilon_0} \tag{2.1}$$

$$\mu_r = \frac{\mu}{\mu_0} \tag{2.2}$$

Often these relative values are written without the subscript r, and unless specified otherwise it can be assumed that $\epsilon$ and $\mu$ represent their relative values. Additionally, $\epsilon$ is often referred to as the dielectric constant of a material.

Both of these values are composed of a real and imaginary component and are traditionally written:

$$\epsilon = \epsilon' - j\epsilon'' \tag{2.3}$$

9

where $\epsilon'$ is the real part of the permittivity and $\epsilon''$ is the imaginary component of the permittivity, also known as the dielectric loss factor. As the name indicates, the imaginary component refers to the energy that is dissipated in the material. The permeability has a corresponding representation:

$$\mu = \mu' - j\mu'' \tag{2.4}$$

where $\mu''$ is the magnetic loss factor, corresponding to the energy that is dissipated in the material due to interactions with the magnetic field.

Another important material characteristic that will be discussed is the loss tangent. Simply, it is the tangent of the angle formed in the complex coordinate system from the real and imaginary components of $\epsilon$ and $\mu$ [58]. It is written:

$$tan(\delta) = \frac{\epsilon''}{\epsilon'} \tag{2.5}$$

$$tan(\delta_m) = \frac{\mu''}{\mu'} \tag{2.6}$$

Two other parameters that will be important in our discussion of material parameters are the wave impedance and refractive index. The wave impedance $\eta$ is used to express the ratio of electric to magnetic field components and is described in Pozar's Microwave Engineering [1] as:

$$H_y = \frac{1}{\eta}(E^+ e^{-\gamma z} - E^- e^{\gamma z}) \tag{2.7}$$

Where $\gamma$ is defined as:

10

$$\gamma = j\omega\sqrt{\mu\epsilon} = j\omega\sqrt{\mu\epsilon'(1 - jtan(\delta))} \qquad (2.8)$$

While the wave impedance is normally a complex value, often a lossless case is assumed which allows for its representation to reduce to:

$$\eta = \sqrt{\frac{\mu_r}{\epsilon_r}} \qquad (2.9)$$

The wave impedance of free space is a fundamental constant and is:

$$\eta_0 = \sqrt{\frac{\mu_0}{\epsilon_0}} = 377\Omega \qquad (2.10)$$

The refractive index is a measure of how much slower a wave propagates through a medium compared to a vacuum. It is defined as:

$$n = \sqrt{\mu_r\epsilon_r} \qquad (2.11)$$

These terms are used to describe the behavior of electromagnetic waves when between the interface of two different materials. This is important to discuss because the algorithms used to extract material parameters, which will be expanded on in later chapters, primarily rely on recording the transmitted and reflected components of a wave. The first case that will be discussed, derived from the work of [1] and [7], is a wave propagating through a vacuum and impinging upon a homogeneous medium with a dielectric constant that is not equal to 1, as shown in Fig. 2.1. After this,

the formulations will be expanded to form a general representation of a wave at the interface of two materials with unequal dielectric constants.
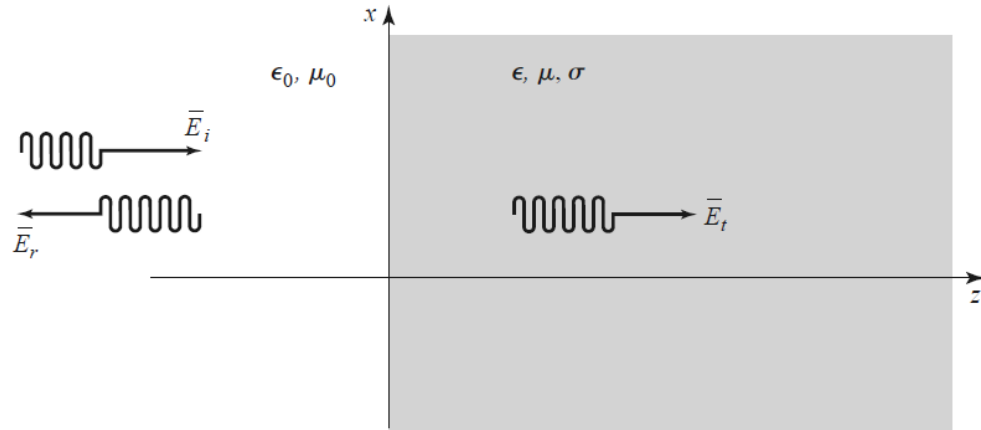


Figure 2.1: Reflected and transmitted components of wave at normal incidence between vacuum and material [1]

The reflected and transmitted components of a wave can be written in terms of the wave impedances of the two materials at an interface. The reflected component will be represented as $\Gamma$ and the transmitted component is written as T. For free space, this impedance is $\eta_0$. By solving the boundary conditions for the fields at the interface of two materials, as shown in [1] section 1.7, we are left with two equations relating T and $\Gamma$ to the wave impedance of the materials:

$$\Gamma = \frac{\eta - \eta_0}{\eta + \eta_0} \tag{2.12}$$

$$T = 1 + \Gamma = \frac{2\eta}{\eta + \eta_0} \tag{2.13}$$

12

Next, we will generalize these equations for any interface between two materials, as shown in 2.2.
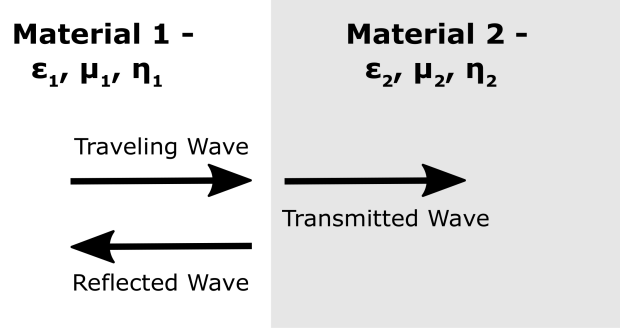


Figure 2.2: Reflected and transmitted components of wave at normal incidence [2]

The generalized equations are:

$$\Gamma = \frac{\eta_2 - \eta_1}{\eta_2 + \eta_1} \tag{2.14}$$

$$T = 1 + \Gamma = \frac{2\eta_2}{\eta_2 + \eta_1} \tag{2.15}$$

Using equation 2.9, we can then rewrite these two general equations in term of the constitutive parameters of both materials at the interface:

$$\Gamma = \frac{\sqrt{\mu_{r2}\epsilon_{r1}} - \sqrt{\mu_{r1}\epsilon_{r2}}}{\sqrt{\mu_{r2}\epsilon_{r1}} + \sqrt{\mu_{r1}\epsilon_{r2}}} \, , \tag{2.16}$$

$$T = \frac{2\sqrt{\mu_{r2}\epsilon_{r1}}}{\sqrt{\mu_{r2}\epsilon_{r1}} + \sqrt{\mu_{r1}\epsilon_{r2}}} \, . \tag{2.17}$$

Because we are able to represent the transmitted and reflected components of a wave solely in terms of the material parameters of the two substances at the interface,

13

it can be inferred that if one was able to collect information about how an applied field behaves, then the material parameters can be extracted.

### 2.2.2   Isotropy and Anisotropy

Another important parameter when discussing the behavior of a material is isotropy and anisotropy. Isotropic materials are those whose characteristics remain constant for any direction of an impinging field, whereas anisotropic materials are those whose characteristics rely directly on the direction of the applied field. Because of this anisotropic behavior, these materials must be represented with a $3 \times 3$ tensor corresponding to the material characteristics with respect to each of the principle planes [7]:

$$\left[ \bar{\epsilon} \right] = \begin{bmatrix} \epsilon_{xx} & \epsilon_{xy} & \epsilon_{xz} \\ \epsilon_{yx} & \epsilon_{yy} & \epsilon_{yz} \\ \epsilon_{zx} & \epsilon_{zy} & \epsilon_{zz} \end{bmatrix} \tag{2.18}$$

$$\left[ \bar{\mu} \right] = \begin{bmatrix} \mu_{xx} & \mu_{xy} & \mu_{xz} \\ \mu_{yx} & \mu_{yy} & \mu_{yz} \\ \mu_{zx} & \mu_{zy} & \mu_{zz} \end{bmatrix} \tag{2.19}$$

This behavior is not common to materials found in nature, occurring mainly in crystals, but is more often seen in engineered materials. This includes composites composed of fibers, particulates, or flakes that are aligned along an axis during manufacturing, as well as honeycomb or tube-filled materials [58]. These materials can

have dramatically different behavior than those composed of a homogeneous medium, and require careful characterization over a range of incident angles to be used effectively in RF devices.

## 2.3  Conventional Material Characterization Methods

All of the systems that will be described in this thesis utilize the transmission/reflection method of material characterization. This can be divided into two subsets: transmission line and free-space techniques. Both of these methods utilize the transmitted and reflected components of an applied wave to extract material parameters over a frequency range that is limited primarily by the hardware of the test set-up and the size and composition of the material-under-test. Two other primary methods for material characterization exist: the resonant, with examples of the method used practically in [59] and [60], as well as the inductance/capacitance method, with a good overview given in [61].

### 2.3.1  Transmission Line Transmission/Reflection

The transmission line method of material characterization is widely used for a variety of reasons: namely, that it is relatively simple [14], offers broad-band performance, utilizes a reasonably sized test set-up (especially in comparison to free space methods), and allows for the measurement of a variety of substances, such as heterogeneous or composite materials [54] [62], liquids [63] [64] and moist materials [65], powders [66] including nano-ferrite powders [67], and gasses [68], in addition to conventional

samples of solid dielectric material. This technique has also been in use for many decades, with Roberts and von Hippel utilizing it in 1941 to characterize materials for centimeter wavelengths [3] as shown in Fig. 2.3, and a vast quantity of discussions about and improvements to the method in the following years.
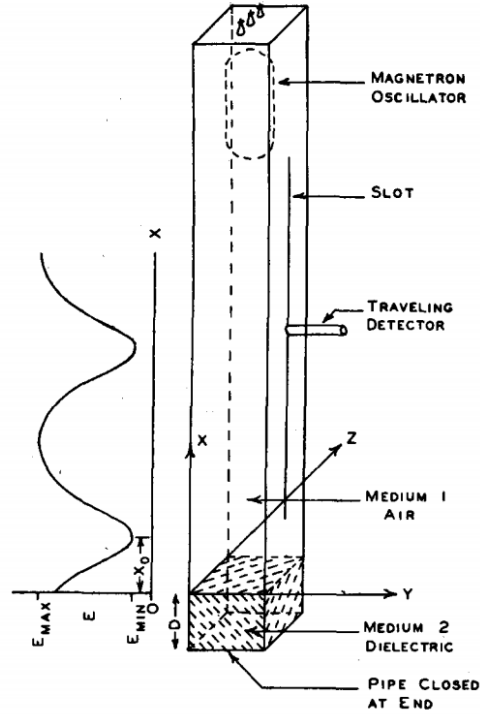


Figure 2.3: Early example of the "hollow pipe" method [3]

This method does have some drawbacks: namely, that unlike the free-space method materials can only be measured at broadside (although anisotropic materials can be evaluated along the "on-diagonal" components eg. $\epsilon_{xx}$ $\epsilon_{yy}$ [8]) and often creation of a sample can be destructive, such that the measured material under test will not be usable in the construction of an RF device. Additionally, the material samples are

sensitive to any gaps existing between the sample itself and the wall of the transmission line, although this can be corrected for [69].
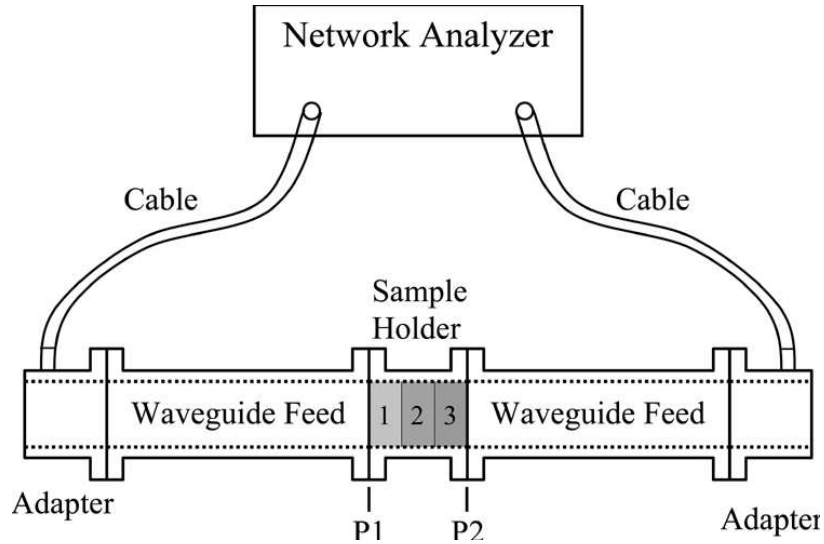


Figure 2.4: Example of simple test setup with 3-layer composite sample [4]

The systems that are used for this method are generally quite straightforward. A wave is injected in to a transmission line, normally a waveguide or coaxial cable, that has one or two ports. Within this line, there must be a component that is able to contain the sample, as well as ensure that there exist no gaps between the transmission line and the material under test. Each port is then connected to a network analyzer. From here, an electric field can be applied to one port and the resultant outputs measured, upon which a material parameter extraction algorithm can be applied. These algorithms use the magnitude and phase of the transmitted and reflected components of the applied field to extract the constitutive parameters of materials.

## 2.3.2 Free-Space Transmission/Reflection

Free-space measurement of materials has been extensively researched for the better part of the last century. This work started in earnest during the Second World War, during which RADAR played a critical role in the conflict and a race to develop and mature technologies intensified. One of the first examples of this technique in practice is found in [70], wherein several examples of different early measurement architectures as well as methods for material parameter extraction are explored. Other works in the following years such as [71] and [72] further expanded upon this. An early example of one such test setup is shown in 2.5. More recent work on the subject is shown in [73], [74], and [75].
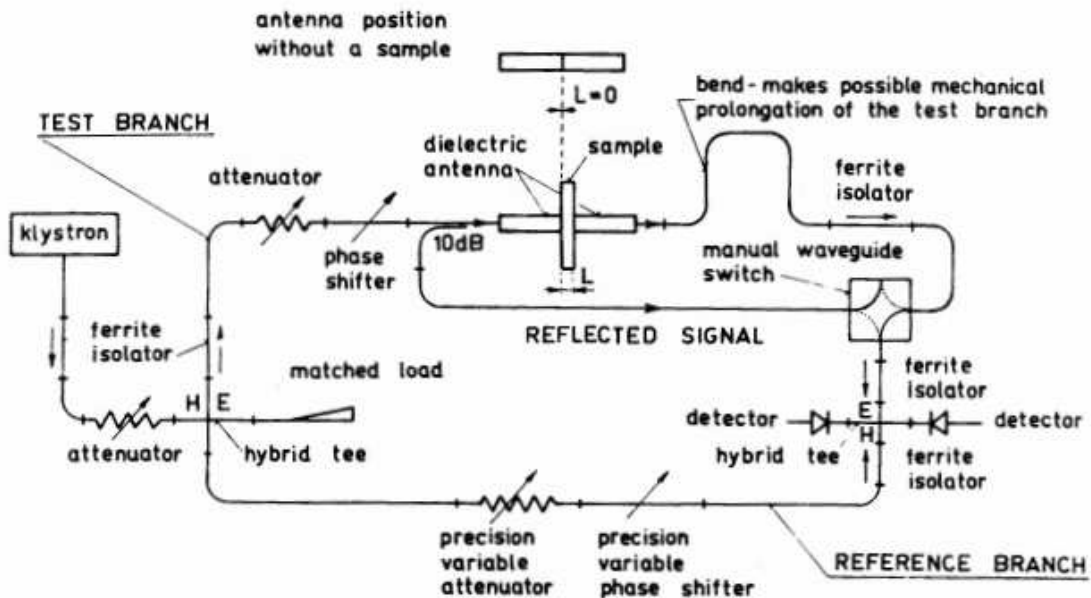


Figure 2.5: Early test apparatus for free-space method [5]

While this method is fairly simple to implement and offers broadband measurements, it still presents some drawbacks. The main difficulties in implementing this method come from the antennas that are used as measurement probes, and from the size of the setup itself. In terms of the antennas being used, it is important that two criteria must be met within the setup: the entirety of the antenna beam must be contained within the sample and the antenna must also be in the far-field region of transmission. When implementing the extraction algorithms, the assumption is made that all of the antennas energy is striking the material under test. If the antenna beamwidth is wider than the sample, then some of the energy transmitted may go directly to the receiving antenna, which skews the measured results. Additionally, if the beam strikes near the edges of the sample, diffraction may occur, which can result in unexpected and inaccurate measurements. For this reason, the rule of thumb for these measurements is that the sample should be at least 1.5 times bigger than the antenna beamwidth at the measurement distance [76] [77].

With respect to the far-field requirement, the extraction algorithms assume that a plane wave is impinging upon the material under test. The far-field distance of an antenna varies widely depending upon its type and the frequency of interest, with some useful guidelines shown in [78]; however, it is generally understood to be the distance from the antenna in the primary direction of propagation at which a constant phase wave is present. If the antenna is not at this distance, errors will occur in the measurement, particularly if the sample is measured at oblique incidence. This is the reason that a lens is often used in concert with the feed antenna, as it provides both a focusing effect and helps to ensure a planar phase front impinges upon the sample

19

[58]. An example of a simple oblique incidence system that utilizes spot-focused lens horn antennas is shown in Fig. 2.6.
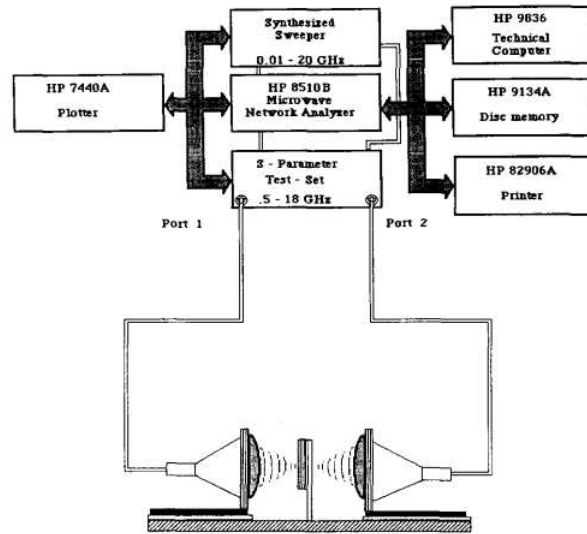


Figure 2.6: Free-space measurement method with lens antennas [6]

A final consideration for the sample is its thickness. While this is primarily related to the chosen extraction algorithm, it is still useful to explore while discussing the test set-up. The original Nicolson-Ross-Weir [39] [40] method has an issue in that it produces multiple solutions when the sample thickness approaches multiples of one-half of the test wavelength. If the sample is electrically thick (e.g. thickness $> \lambda/2$), this will have to be taken into account, although in recent years, this issue has been resolved through the use of a root search to find resonance points [34], the Kramers-Kronig integral [79], phase unwrapping [47], or iterative methods [80] [81].

Considering all of this, the other major difficulty in implementation of a free-space measurement system is its overall size. Factoring in the size of the sample and the size of the antennas can lead to very large test configurations, especially

for testing at relatively low frequencies. For example, in Focused Beam Methods, John Schultz gives an example of a system for material characterization at 500 MHz which incorporates dielectric lenses that are 6ft. in diameter [58]. While lenses and dielectric rod antennas are useful for reducing the required size of the system, the available space for a test system must be considered when deciding if the free-space material characterization method is the correct method for the application.

## 2.4   Summary

In this chapter, the characteristics of materials that will be measured are discussed, including permittivity and permeability, the behavior of waves at a material interface, and isotropy/anisotropy. These parameters and characteristics will be referenced throughout this thesis. Derivations for these parameters are presented along with their sources. The relationship between the physical composition of a material and its effects on an impinging electromagnetic wave is explored. Additionally, two of the major measurement methodologies for material characterization are discussed with an overview of their implementation and merits given. These are the transmission line and free-space methods, both of which are based on transmission and reflection of an applied field upon a material under test. These early examples are a good illustration of the advancement that has occurred in measurement technologies in the preceding decades.

# Chapter 3

# Waveguide Method for Material Characterization

## 3.1    Introduction

In this section, the actual implementation of the waveguide-based system here at the ARRC will be described. The physical setup will be shown and discussed, as well as descriptions of the calibration and material parameter extraction methods. Finally, development of the user interface and measured results will be discussed. An additional section discussing attempted implementation of a rectangular to square waveguide transition will follow. Although this was never successfully physically realized, extensive simulations were performed and they will be discussed.

## 3.2    Rectangular Waveguide for Characterization of Isotropic Materials

The implementation of a guided wave material characterization system for the Advanced Radar Research Center has proved to be a valuable resource both for the group the author is a part of (The Phased Array Antenna Research and Development group) but also to the lab as a whole. With the increasing use of 3D printed substrates

for use both in antennas and filters, a method to rapidly characterize the constitutive parameters of a printed structure has proven to be invaluable. In the following results, the testing of traditional commercially available substrates, homogeneous 3D printed materials, and non-homogeneous manufactured substrates will be discussed.

### 3.2.1 Rectangular Waveguide Functionality

The waveguide system that has been implemented utilizes a $72.136mm$ by $17mm$ (2.84" by 0.67") waveguide. The width (or the (a) dimension in Fig 3.1) of these waveguides is the same as the standard WR284 (or WG10) sized waveguide, although the height or (b) dimension is half the size of a normal WR284. This is useful in suppressing the existence of higher order modes. This is the same waveguide used by Yeary, et all, for the OU SPY-1 project, as detailed in [82].
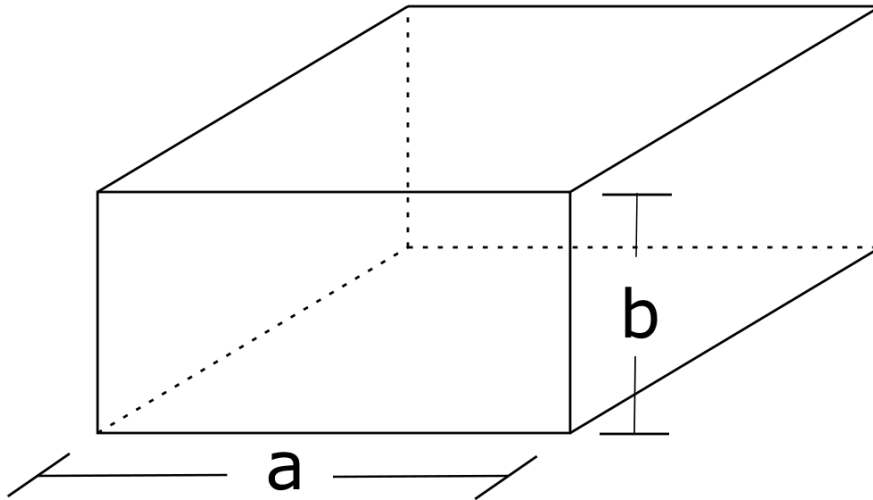


Figure 3.1: Rectangular waveguide dimensions

The effective frequency range for this system is $2.60 - 3.95$ GHz and is determined by the cutoff frequency of the dominant and secondary modes of the waveguide. These modes, which represent the field orientations within the waveguide, are visualized well in Fig 3.2.
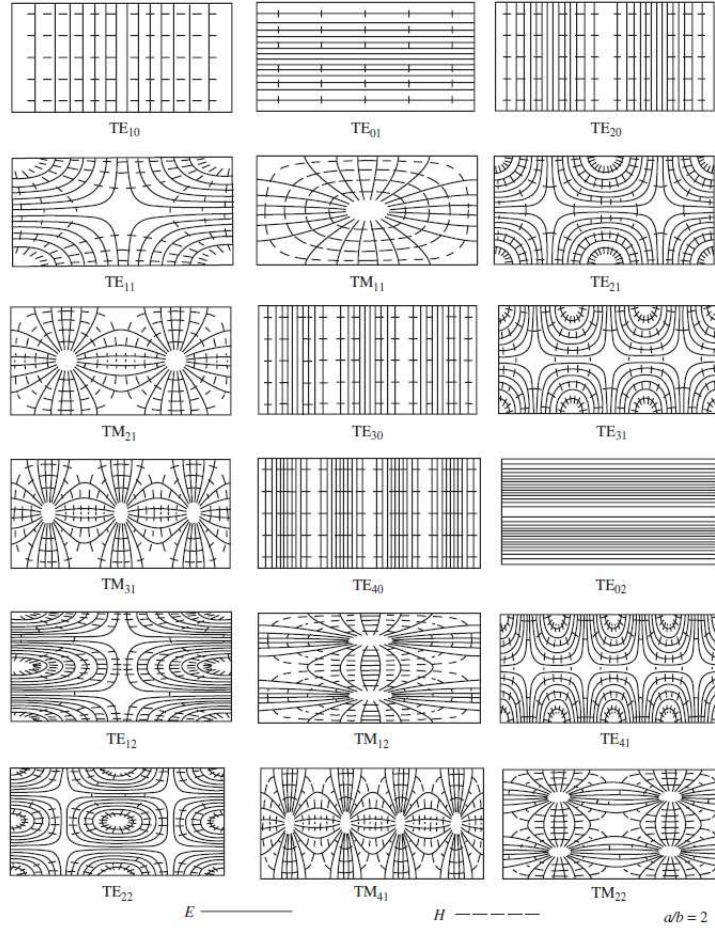


Figure 3.2: Rectangular waveguide modes for a/b = 2 [7]

The cutoff frequencies for each transverse electric (TE) or transverse magnetic (TM) mode are calculated with an equation given in [7], as shown below in equation 3.1, with m and n being eigenvalues that represent different modes that can be excited:

$$(f_c)_{mn} = \frac{1}{2\pi\sqrt{\mu\epsilon}}\sqrt{(\frac{m\pi}{a})^2 + (\frac{n\pi}{b})^2} \qquad (3.1)$$

Because operating near the cutoff frequency will lead to reduced performance, when determining the actual working frequency range, a common rule of thumb is that the lower limit of operation is $1.25 \times f_c$ and the upper limit is $1.90 \times f_c$ [83] where $f_c$ is the cutoff frequency of the $TE_{10}$ mode and is calculated as:

$$(f_c) = \frac{c}{2 \times a} \qquad (3.2)$$

where $c =$ the speed of light $= 2.99 \times 10^8$ m/s and a is equal to the width of the waveguide as shown in table 3.1. The modes that can be excited were then calculated and the first several are displayed in table 3.1.

Table 3.1: Cutoff frequency for rectangular waveguide (76.136 mm x 17 mm)

| m | n | $F_c$ |
|---|---|---|
| 1 | 0 | 2.08 GHz |
| 2 | 0 | 4.16 GHz |
| 3 | 0 | 6.24 GHz |
| 4 | 0 | 8.32 GHz |
| 0 | 1 | 8.82 GHz |
| 1 | 1 | 9.07 GHz |
| 2 | 1 | 9.75 GHz |
| 3 | 1 | 10.8 GHz |

These calculations were also verified with simulations performed in HFSS, by performing an eigenmode simulation of the waveguide structure we had:
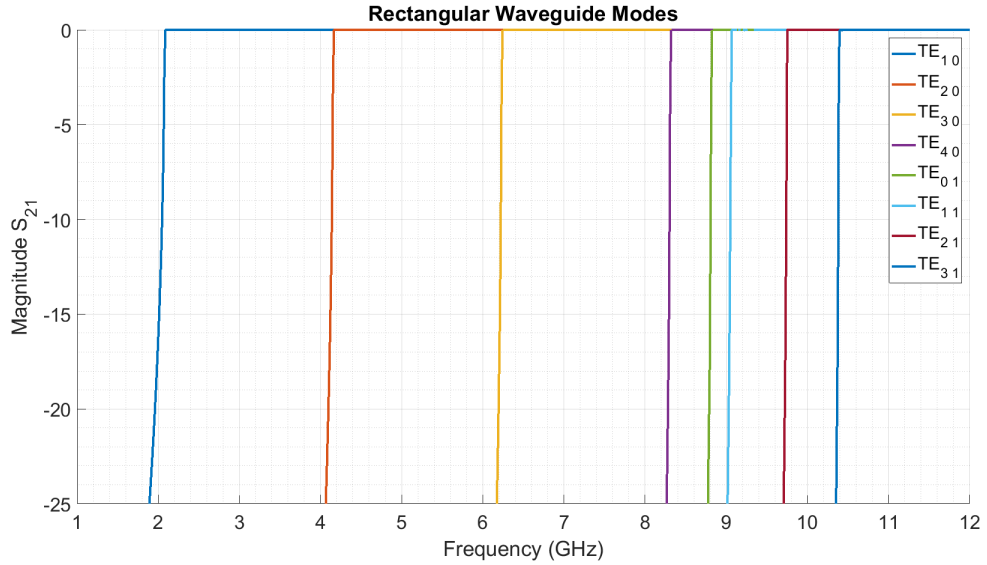
Figure 3.3: HFSS simulations of waveguide structure showing different excited modes

We can see here that the first mode excited is $TE_{10}$, thus it is the mode that is used for measurements. The operable frequency range is defined between the first and second excited modes. While the discussion of the excitation of different modes is important for understanding the hardware limitations of this system, it will become much more useful when considering the implementation of a square waveguide, as the higher order modes will be much closer to the frequency range we are operating over.

### 3.2.2 System Description

For the system that has been implemented in this thesis, the aforementioned waveguide is mounted on a metallic rail for easy manipulation. The base system is composed of two sets of two identical parts: an 11 cm long feed and a 17.5 cm section of waveguide. Each feed section is a probe-feed for the waveguide that connects to a coaxial cable which allows for excitation with a VNA. These straight waveguide

sections are necessary to attenuate any evanescent higher-order modes that may result from the waveguide to coaxial connection [40]. This hardware is displayed in Fig. 3.4:
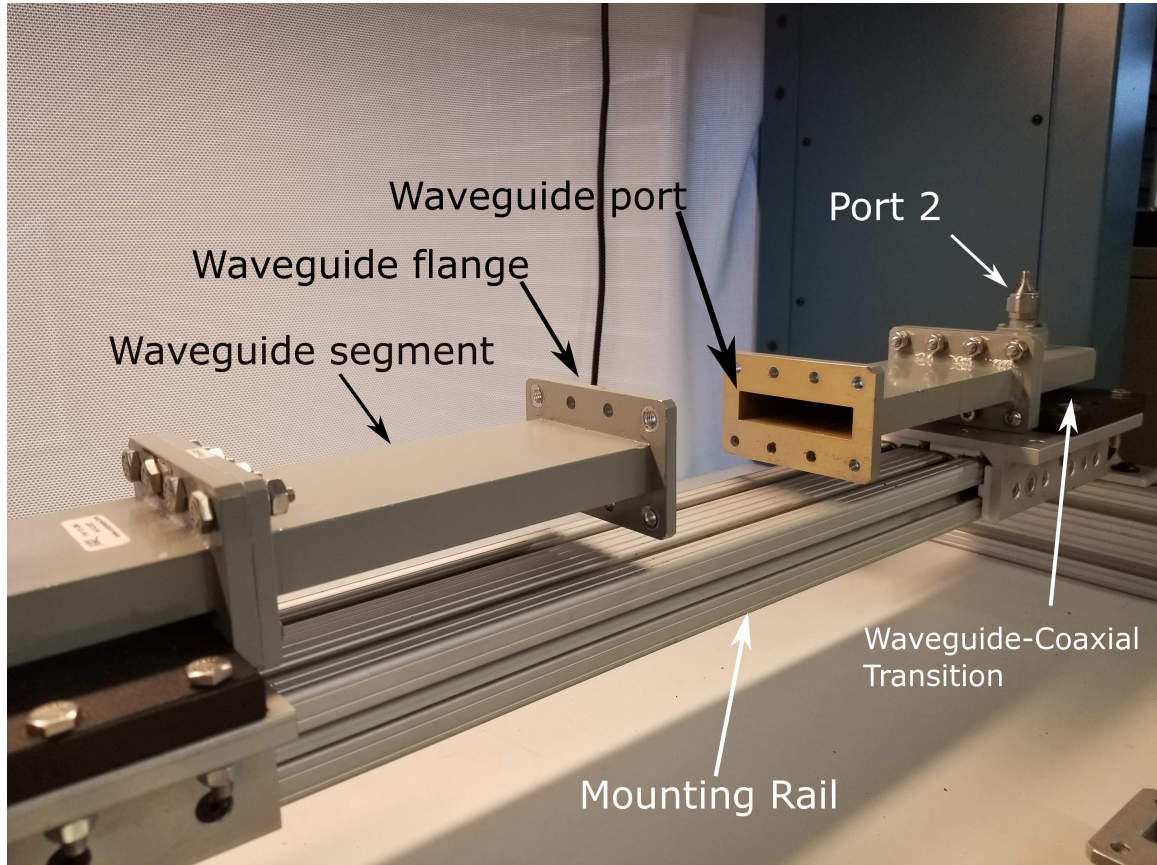


Figure 3.4: Physically realized waveguide system showing feed, line, and port

As shown, each section is attached to one another with the use of four bolts and nuts. Each feed is also attached to a metallic carriage, which allows for linear manipulation. Before this rail was implemented, the waveguides rested on the work bench and this in turn created variability in measurements, as the waveguide was free to rock back and forth. Additionally a mount was constructed that fits on the side of the rails, which allows for storage of extra hardware for added ease of use of the system, as shown in Fig. 3.5. Fig. 3.5 also shows the thin segments of waveguide

(which will be referred to as slides going forward) that are used as line delays for the calibration procedure, as well as to hold samples for measurement.
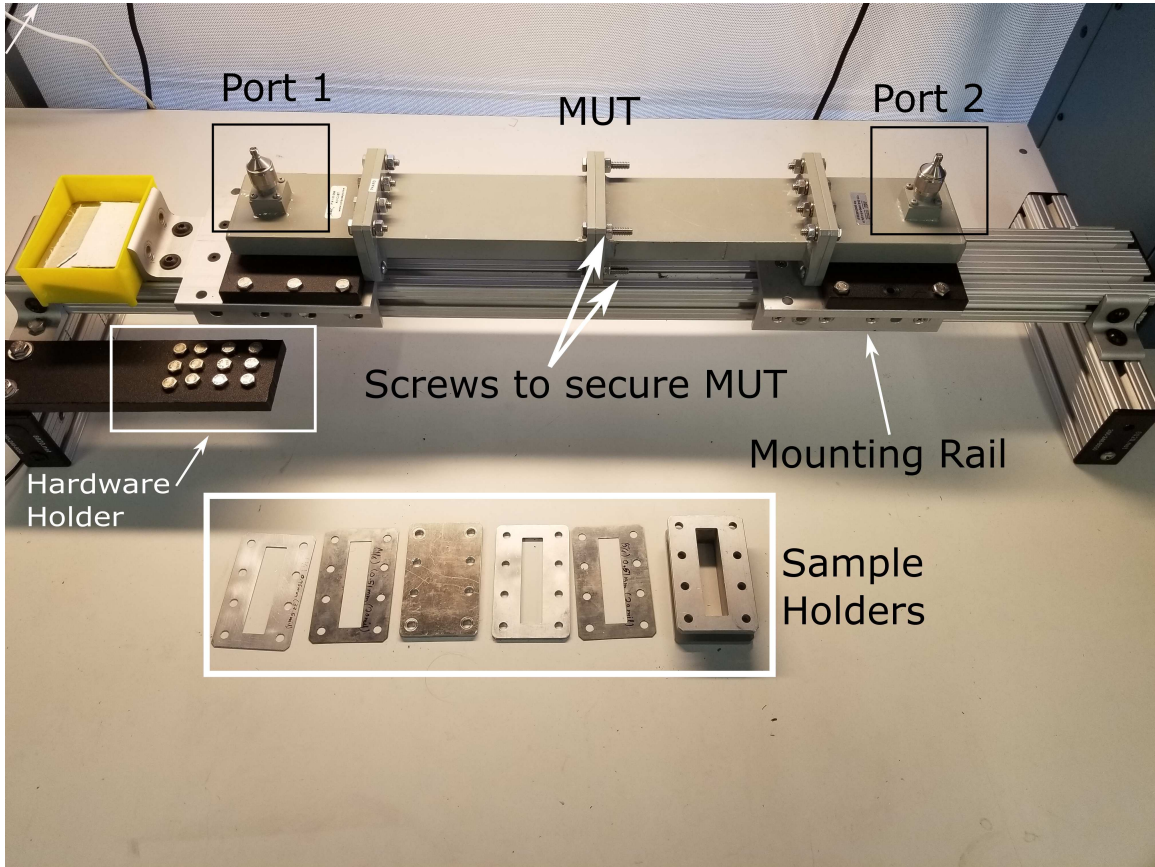


Figure 3.5: Waveguide system closed with hardware mount and sample holders, material under test mounted between both ports

As shown above, the two identical segments are attached to one another with the same set of four bolts and nuts. These are used for all measurements to ensure consistency, although it is important to ensure that they are not tightened excessively, as this can result in bending or damage to the waveguides.

### 3.2.3 VNA Description

Testing with this system was done with either a Copper Mountain Planar 804/1 or 814/1 VNA. They exhibit very similar performance. Both VNAs have a frequency range of 0.1 MHz to 8.0 GHz and have two ports. This is well within the frequency band of interest for our system. Another very useful aspect of the Copper Mountain VNAs is that they come with a built in LabView library. The software implementation will be discussed in detail in section 3.2.6, but it is worth mentioning that these libraries make integration significantly easier. The entire setup, including the VNA and attached coaxial cables, is shown in Fig. 3.6:
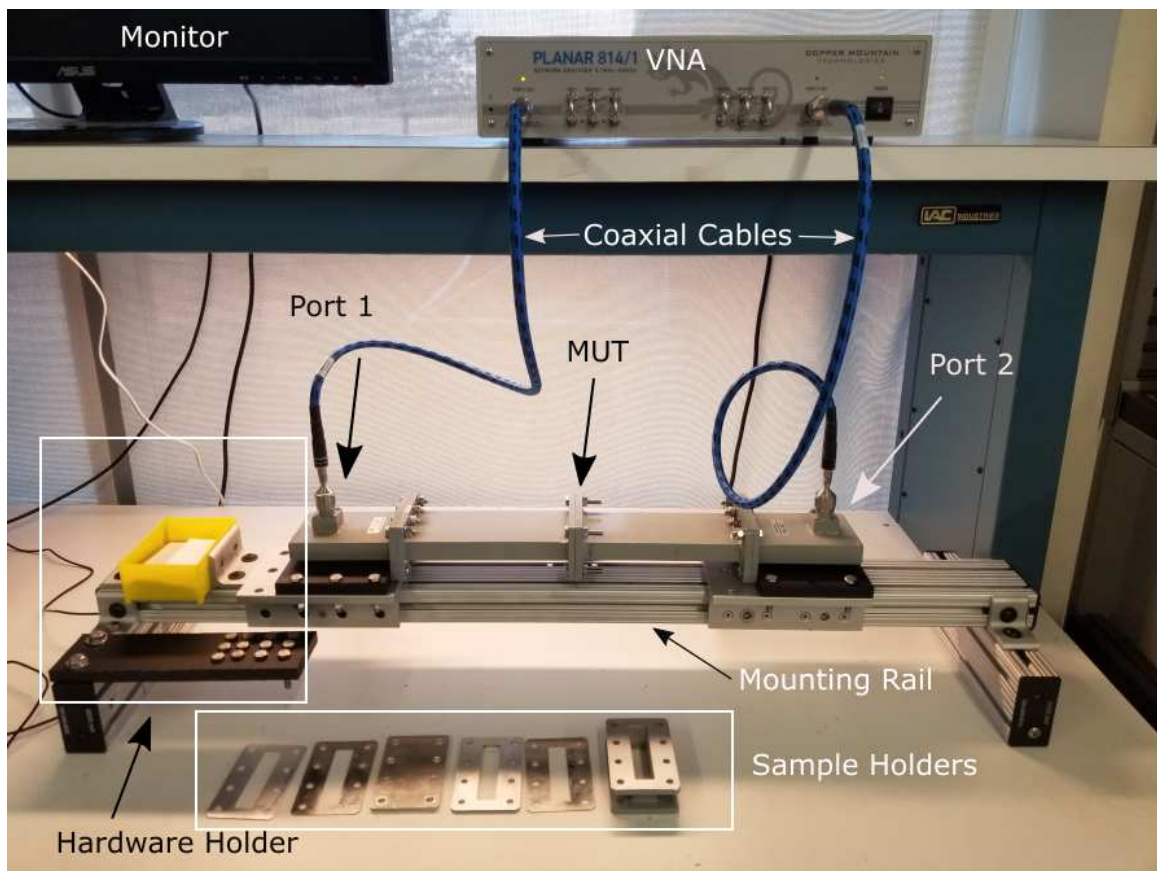


Figure 3.6: Full waveguide system with VNA

### 3.2.4 Calibration

A two port Thru-Reflect-Line (TRL) calibration is implemented in this system. When discussing the calibration of this system and VNAs in general, the work of Rytting in [84] is a wonderful reference on the internal methods a VNA is applying, while Pozar also gives a great general overview in [1]. In general, the calibration is performed to determine and eliminate the effects of connectors, cables, and everything that is leading up to the reference plane where the MUT (referred to as the DUT in Pozar) will be placed. By applying loads of known values to each port, the error can be quantified, which is often referred to as the "error box" of each port [1]. The author will not discuss all of the calculations required for this procedure, as they have been covered extensively, but generally, to perform a two-port calibration one must solve for five parameters: $S_{11}$, $S_{22}$, $S_{12}$, $\Gamma_L$, and $e^{\gamma l}$ and these parameters are related together by five equations listed below:

$$T_{11} = S_{11} + \frac{S_{22}S_{12}^2}{1 - S_{22}^2} \tag{3.3}$$

$$T_{12} = \frac{S_{12}^2}{1 - S_{22}^2} \tag{3.4}$$

$$R_{11} = S_{11} + \frac{S_{12}^2 \Gamma_L}{1 - S_{22}\Gamma_L} \tag{3.5}$$

$$L_{11} = S_{11} + \frac{S_{22}S_{12}^2 e^{-2\gamma l}}{1 - S_{22}^2 e^{-2\gamma l}} \tag{3.6}$$

$$L_{12} = \frac{S_{12}^2 e^{-2\gamma l}}{1 - S_{22}^2 e^{-2\gamma l}} \tag{3.7}$$

Where T refers to measurements taken with the Thru connection (pictured in Fig. 3.7 (a) ), R refers to measurements taken with the Reflect standard (pictured in Fig. 3.7 (b) ), and L refers to measurements taken with the Line standard (pictured in Fig. 3.7 (c) ). These five equations relate these error parameters to measured transmitted and reflected components, when each of the three loads (Thru, Reflect, and Line) are applied. The algebra to solve these five equations is quite involved, so if one is interested, solutions are available in [1] Section 4.5.



Figure 3.7 (a): Thru      Figure 3.7 (b): Reflect      Figure 3.7 (c) : Line

Figure 3.7: Waveguide calibration standards

As shown in Fig. 3.7, there are three unique calibration standards and all are required to apply a TRL calibration. The Thru standard is quite simple, one must only connect the two waveguide sections at the reference planes (where the MUT will be placed) and take a measurement. The Reflect standard can be any load where at the reference plane the VNA sees an approximately open or short. This results in all incident energy being reflected back, hence the name, with the only difference in an open or short being a 180° phase difference. The reflect standard used for this project is a precisely milled piece of aluminum designed to fit perfectly over the opening of

the waveguide with holes that match the flanges. The final standard required is the Line, which serves to produce a phase delay. In the above equations, the length of this line is represented by the symbol $l$. The length of line must be known and should not be a $\lambda/2$ multiple of the frequency of interest, as this can produce uncertainty in the phase measurements. By measuring the length of the line combined with the known guided-wave velocity, the time delay from the line can be input into the VNA, allowing for completion of the calibration.

### 3.2.5 Material Parameter Extraction Algorithm

To extract the constitutive properties of the MUT, the Nicolson-Ross-Weir (NRW) method is employed. This is a closed form method initially proposed in 1970 by [39] and modified in 1974 by [40] to become the method that is now commonly used today. An in-depth study of the method is presented by Rothwell in [85], wherein multiple cases of its application are studied. To employ this method, one must have calibrated their VNA to the plane of reference directly adjacent to the MUT, it is possible to compensate for a material sample that is not the same size as the sample holder as seen in [26], but this is more relevant to and thus will be discussed in section 3.3. Once the VNA is fully calibrated, the sample must be placed in a section of waveguide ensuring that there exist no gaps between the sample and the walls of the waveguide, as this will introduce significant error [69]. Once the sample is situated in the waveguide, a measurement can be taken. This will provide two data points of each frequency: the transmitted and reflected components of the wave through the material which are represented with $S_{11}$ and $S_{21}$. These two measurements are

then used through the following method (primarily sourced from [85] but also with reference from [39], [40], and [86]) to extract the material parameters:

First. the propagation factor $P$ for a wave propagating through the material under test is defined as:

$$P = e^{-jk_z d} \tag{3.8}$$

Where $k_z$ is the propagation vector in the direction of propagation through the waveguide, defined as the $\hat{z}$ direction, written as:

$$k_z^2 = k^2 - \kappa^2 \tag{3.9}$$

where $k$ is the wavenumber of the material, defined as:

$$k = \omega\sqrt{\mu\epsilon} \tag{3.10}$$

Depending on the application, the value of $\kappa$ will vary. For a $TE_{10}$ rectangular waveguide, such as presented in this section $\kappa = \pi/a$. For a guided-wave system that utilizes a TEM wave, $\kappa$ is assumed to be 0, and for a free-space system then $\kappa = \omega\sqrt{\mu_0\epsilon_0}(\theta_0)$. For the rest of this section, we will focus exclusively on $TE_{10}$ mode propagation.

Next, we can define the reflection coefficient for the wave impinging on the MUT as $\Gamma$ where:

$$\Gamma = \frac{Z - Z_0}{Z + Z_0} \tag{3.11}$$

Where $Z$ and $Z_0$ are defined as:

$$Z = \frac{\omega\mu}{k_z} \tag{3.12}$$

$$Z_0 = \frac{\omega\mu_0}{k_{z0}} \tag{3.13}$$

With $k_{z0}$ defined as:

$$k_{z0}^2 = k_0^2 - \kappa^2 \tag{3.14}$$

where $k_0 = \omega\sqrt{\mu_0\epsilon_0}$. We can then relate the two parameters $\Gamma$ and $P$ to the measured S-Parameters as:

$$S_{11} = \frac{(1 - P^2)\Gamma}{1 - P^2\Gamma^2} \tag{3.15}$$

$$S_{21} = \frac{(1 - \Gamma^2)P}{1 - P^2\Gamma^2} \tag{3.16}$$

Equations 3.15 and 3.16 and then be rewritten using two placeholder variables as:

$$S_{21} + S_{11} = \frac{P + \Gamma}{1 + \Gamma P} = V_1 \tag{3.17}$$

and

$$S_{21} - S_{11} = \frac{P - \Gamma}{1 - \Gamma P} = V_2 \tag{3.18}$$

Next, in every derivation seen thus far, the variable $\chi$ is calculated as:

$$\chi = \frac{S_{11}^2 - S_{21}^2 + 1}{2S_{11}} \tag{3.19}$$

Which then allows us to rearrange equations 3.17 and 3.18 to eliminate the variable $P$ so that:

$$\Gamma^2 - 2\Gamma\chi + 1 = 0 \tag{3.20}$$

This forms a quadratic equation to solve for $\Gamma$, with the caveat that by applying the quadratic formula we will create the potential for two solutions:

$$\Gamma = \chi \pm \sqrt{\chi^2 - 1} \tag{3.21}$$

However, the ambiguity of this answer does not present a major problem, as we can assume the material under test is passive (i.e. the material does not offer gain), in which case the condition $|\Gamma| \leq 1$ can be applied, as only one solution will satisfy it. Once equation 3.21 has been solved, one can then solve for $P$:

$$P = \frac{V_1 - \Gamma}{1 - V_1\Gamma} \tag{3.22}$$

Having solved for both $P$ and $\Gamma$, we can then begin to solve for the material parameters. This solution can be written multiple ways, depending on the source.

The author will start by showing the classical representation, followed by an alternate form that was found to be easier to follow. First, the classical form from [40]:

$$\frac{1}{\Lambda} = \left(\frac{\epsilon_r \mu_r}{\lambda_0^2} - \frac{1}{\lambda_c^2}\right) = -\left[\frac{1}{2\pi l} \ln \frac{1}{P}\right]^2 \tag{3.23}$$

where $\lambda_0$ is the free-space wavelength and $\lambda_c$ is the cutoff wavelength of the waveguide. $\Lambda$ can further be defined with:

$$Re\left(\frac{1}{\Lambda}\right) = \frac{1}{\lambda_g} \tag{3.24}$$

Unfortunately for those trying to implement this methodology, equation 3.23 presents a problem in the form of an ambiguity. Because $P$ is a complex value, and the natural logarithm of a complex number has infinite roots repeating every integer multiple of $2\pi$, there will be an infinite number of solutions to equation 3.23. This is more clearly illustrated in [85] with the following equation; note that the value of $\bar{k}_z = k_z / k_0$

$$\bar{k}_z = \frac{n - \frac{\phi}{2\pi}}{\frac{d}{\lambda_0}} + j\frac{\frac{\ln P}{2\pi}}{\frac{d}{\lambda_0}} \tag{3.25}$$

Where the variable n represents the infinite integer solutions available. This is also commonly referred to as the branching problem, and there exists extensive literature on how to work around this issue such as in [87], [8], and [42]. This is mainly a concern when the material is electrically large (i.e thickness $\geq \lambda/2$) or when measuring a substrate that does not behave in a manner consistent with naturally occurring

materials. Because the samples that were measured with this system do not approach that thickness, and the bandwidth the system is capable of measuring over is not exceptionally large, this is not an issue to discuss in this section.

To finish this derivation, and illustrate how the material parameters will be extracted, first we must define a placeholder variable $F$ as:

$$F = \frac{1 - \Gamma}{1 + \Gamma} \tag{3.26}$$

and calculate:

$$\bar{k}^2 = \bar{k}_z^2 + \bar{\kappa}^2 \tag{3.27}$$

letting $\bar{\kappa} = \kappa/k_0$. Using $F$ and $\bar{k}^2$, we can then solve for the relative permittivity and permeability of the material as follows:

$$\epsilon_r = \bar{k}^2 \frac{\bar{k}_{z0} F}{\bar{k}_z} \tag{3.28}$$

$$\mu_r = \frac{\bar{k}_z}{\bar{k}_{z0} F} \tag{3.29}$$

### 3.2.6   GUI Development

A primary concern for this project was the creation of a user interface to control the calibration, measurement, and post-processing for this system. Originally, each of these processes were conducted separately and required more time than was ideal,

with the user having to calibrate the system with software specifically for the VNA and then import the data manually into MATLAB to run the NRW script. This was a time consuming process that did not allow for quick visualization of measurements. To rectify these issues, a GUI was developed that allowed for all the requisite tasks required to acquire measurements into a single centralized place. The final GUI is pictured below in Fig. 3.8:
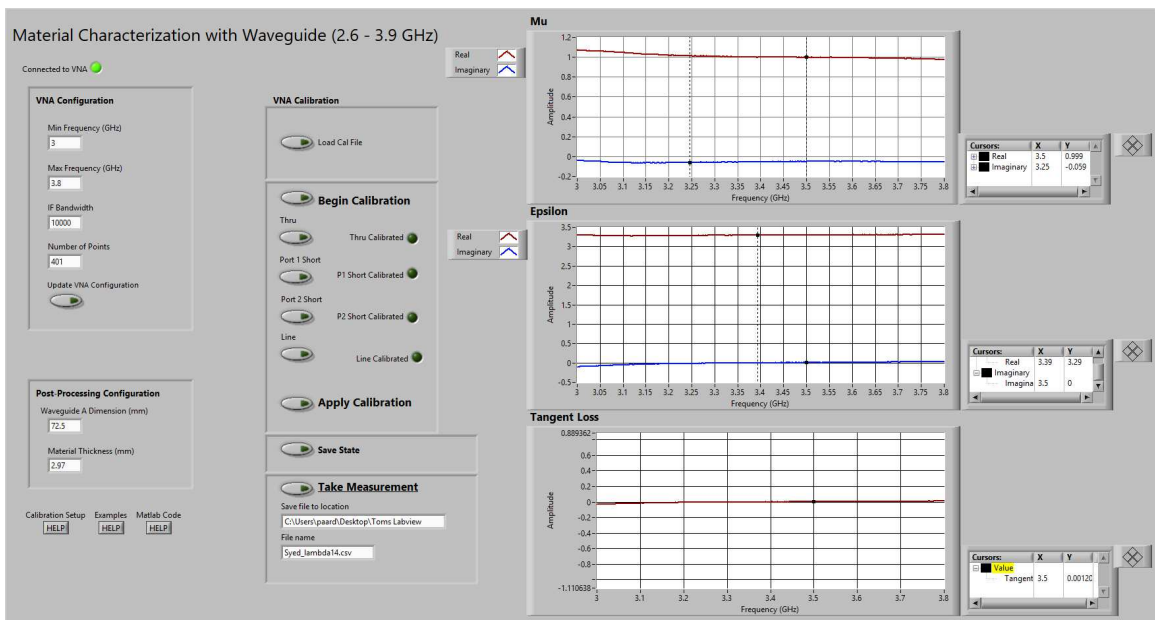


Figure 3.8: User interface for waveguide system

The measurements visible are of a 3D printed substrate modified with an array of cylindrical air gaps to form an artificial dielectric. More detail on the measured results will be discussed in the following section. However, first each of the features of the code will be illustrated. For reference, an overview of the code will be discussed first.

### 3.2.6.1    Overview

The overall control software architecture is shown below in Fig. 3.9.
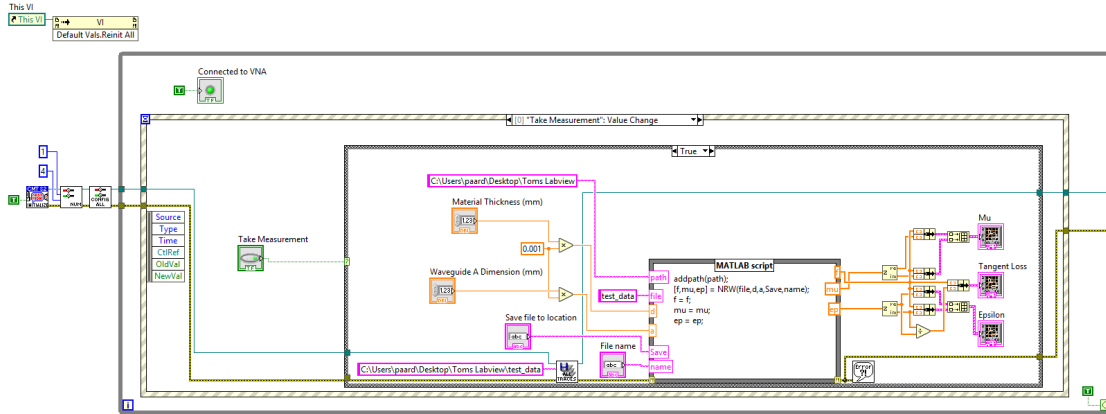


Figure 3.9: Control software overview

Here we can see the basic layout of the code, which is centered around an event structure that tracks user inputs and produces the corresponding desired result. The program initially resets all stored variables and connects to and configures the VNA to the basic/expected state with the correct number of traces that each contain the correct parameter. This is important, as the VNA exports data based on the order of traces and could corrupt the collected data if the user was allowed to configure it erroneously. After this, the code enters a While Loop where it remains indefinitely, waiting for a user input. Each of these possible inputs, and their implementation, will be discussed below.

### 3.2.6.2 Calibration

The first step in taking successful and accurate measurements is the application of a calibration state to the VNA. The user can accomplish this in one of two ways: by loading a saved calibration state or by calibrating the system manually. We will cover the manual calibration process first, as this is the most common activity undertaken.

To begin calibrating the system, the user selects the "Begin Calibration" button as shown in 3.8. As you can see in Fig. 3.10, there are no user inputs for this section.
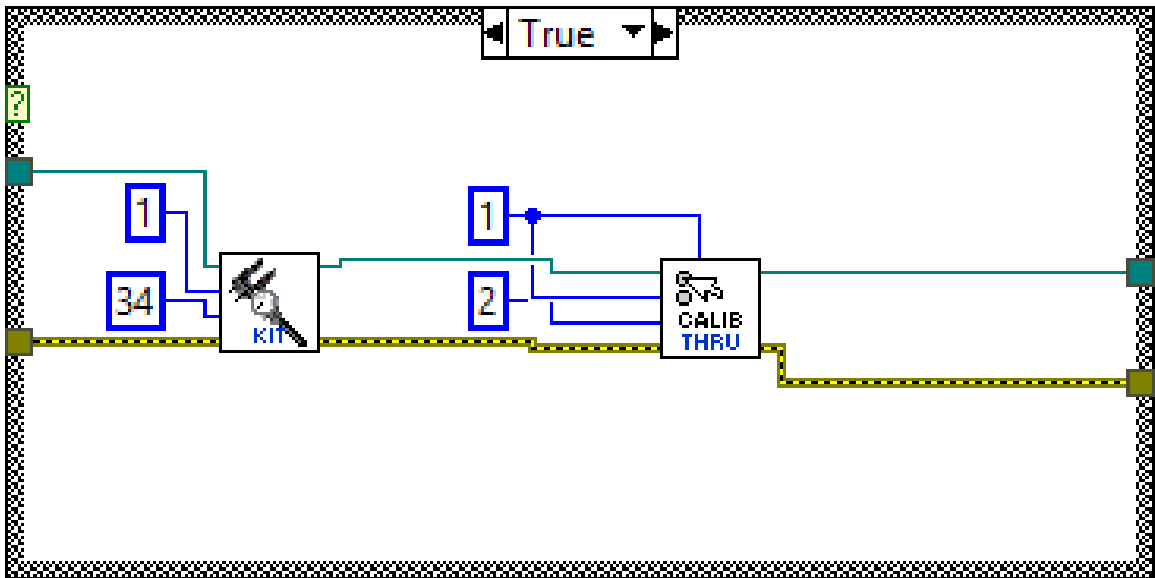


Figure 3.10: User begins calibration procedure

Instead, the code is simply instructing the VNA to load the requisite calibration kit. This is exceedingly important, as the computer used to control the waveguide system is also used to control other measurement devices. Thus, the VNA may be programmed to use a different calibration kit. These kits tell the VNA about the calibration standards that will be used, as well as the frequency range for calibration.

If the user does not specify the correct calibration kit and tries to run a calibration, the VNA will simply not comply and will return an error. This was a significant source of frustration when this project first began, as the author struggled to discover why his calibration code occasionally would not work after another user had worked with the VNA. Thankfully, the calibration kits are stored locally on the computer and have a constant index, so a known kit will be loaded into the system every time measurements are to be taken. This kit covers the full working frequency range of the system, therefore it will work for any logical frequency setting.

At this point, the user can configure the frequency range they would like the VNA to operate over, the number of points in the frequency sweep, and the IF bandwidth. This procedure makes use of a VI native to the Copper Mountain library and is shown below in Fig. 3.11:
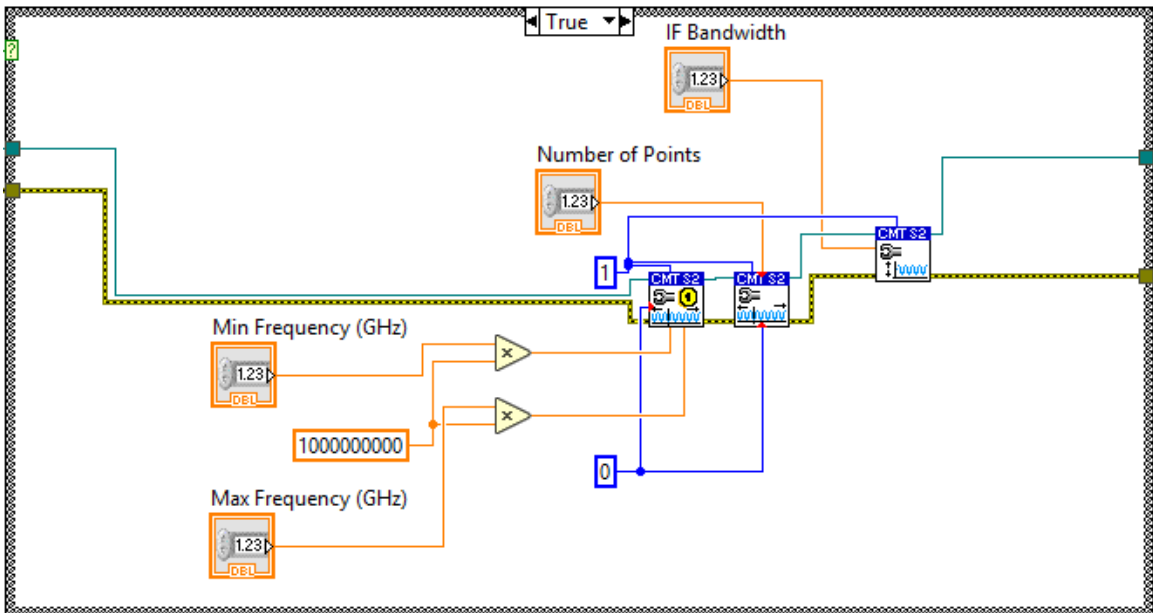


Figure 3.11: Update VNA settings

After preparing the VNA for calibration, the TRL calibration method as described in section 3.2.4 must be carried out. To accomplish this, the user is presented with four buttons that each trigger a specific calibration standard to be measured.

For a Thru measurement, the code to accomplish this is shown below in Fig. 3.12:
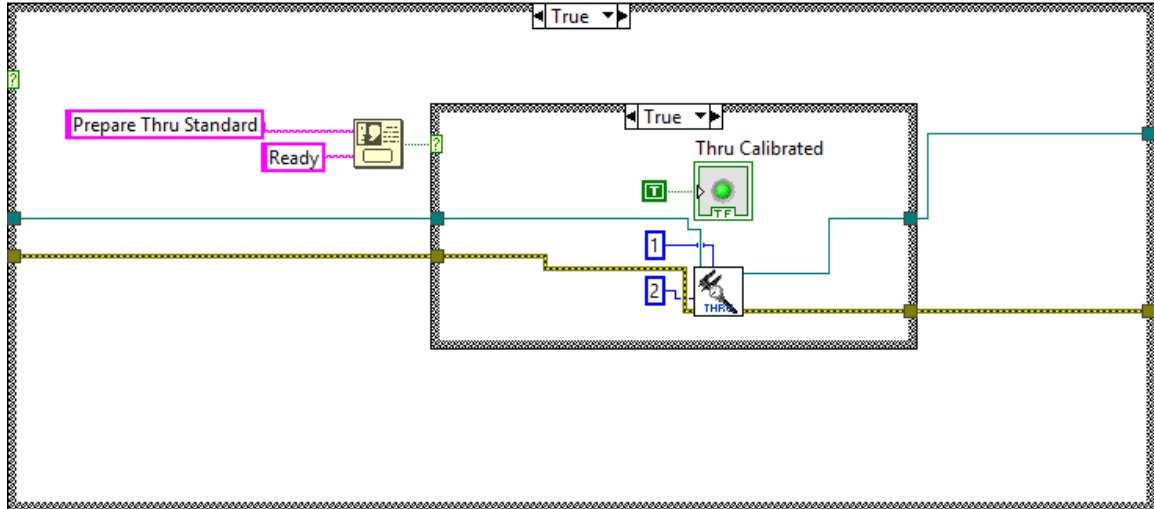


Figure 3.12: Thru calibration

The user is first prompted to input the standard, in this case connecting each waveguide section directly to one another. After the user confirms the standard is ready, the VNA is prompted to take the measurement. For each LabView Virtual Instrument (VI), the term used for a code block, that communicates with the VNA, SCPI commands are used. The potential commands that can be used are extremely extensive, as shown in their programming manual [88]. With these SCPI commands, basically every functionality present in their control software can be accomplished programmatically. Following this, the user will take two measurements with the Short/Reflect standard, one for each port, as shown below in Fig. 3.13:
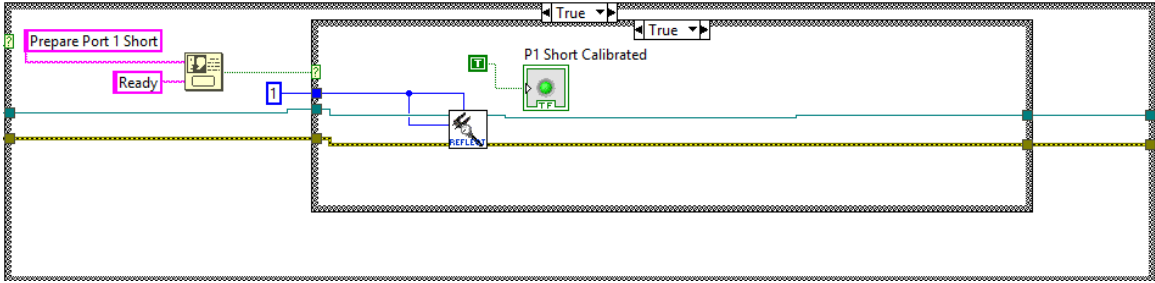
Figure 3.13: Reflect calibration

This will be followed, finally, by taking a single Line delay measurement. This is shown below in Fig. 3.14:
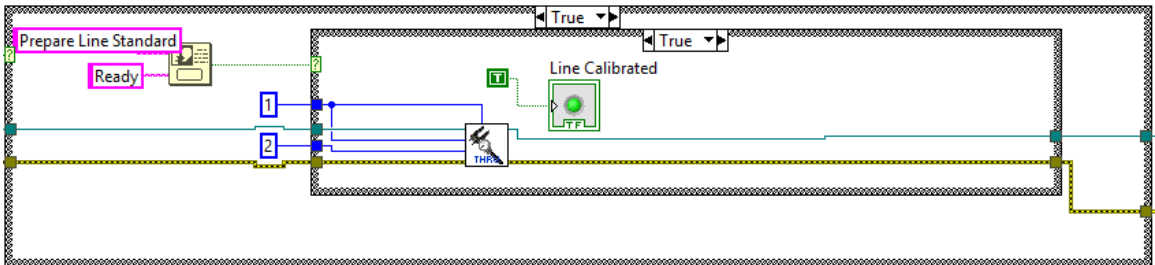


Figure 3.14: Line calibration

The user will then press the apply calibration button to perform the required calibration. If the user is happy with the calibration state, they can save it, as shown in Fig. 3.15. They will then be prompted by the software to choose a location to save the file with the name of their choosing.
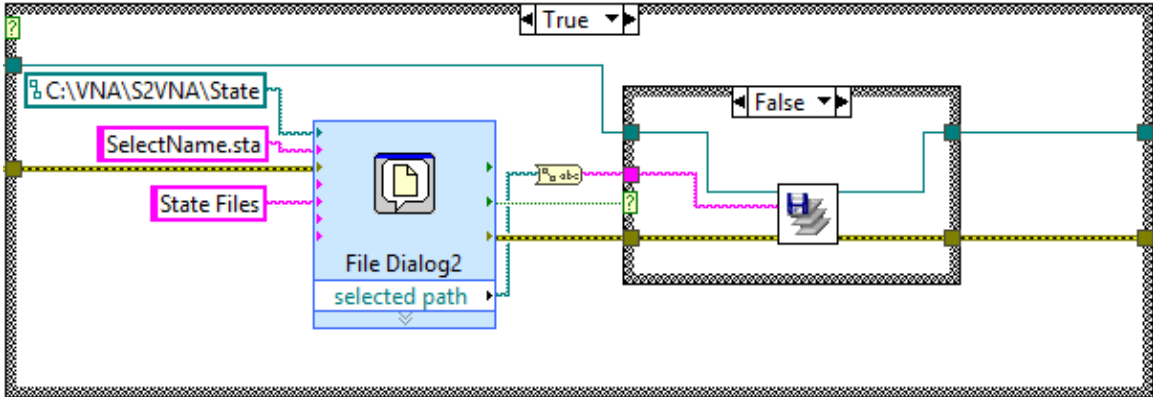
Figure 3.15: Save calibration state

The user also has the option to load a previously saved calibration state. This is particularly useful when the user wants to take multiple measurements over a period of time during which the system has not been tampered with in any way (i.e. the cables have not been moved or the connectors have not had their tightness adjusted). An example of the code that handles this procedure is shown in Fig. 3.16.
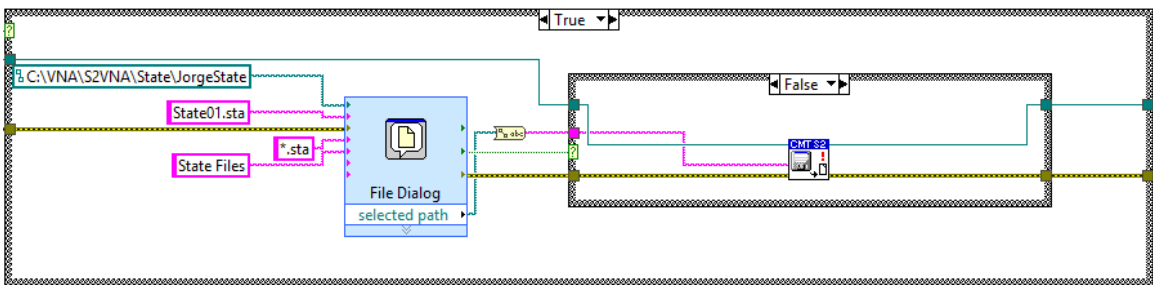


Figure 3.16: Load calibration state

Care should be taken to not rely on this procedure too heavily however, as there exists the possibility that the system was modified without the user's knowledge or that unintended contact with the system has led to slight shifts in cable positioning which can dramatically change the errors present on each port.

44

### 3.2.6.3    Measurements

Once the system is satisfactorily calibrated, taking measurements is the next step. To accomplish this, the user must verify that the settings for the post-processing are correct. These two variables are the width of the waveguide and the thickness of the material. As shown above in section 3.2.5, both of these variables are used in extracting the material parameters. It is important that the user verify these values are correct, as even slight deviations will produce dramatic changes in the results. The waveguide width will most likely not change, but the code was written with adaptability to other waveguide-based material measurement systems in mind so the option exists for use with different size waveguides. There is no button press required to update these values, as they are taken directly into the material extraction algorithm when a measurement is triggered. The code for triggering a measurement is shown below in Fig. 3.17.
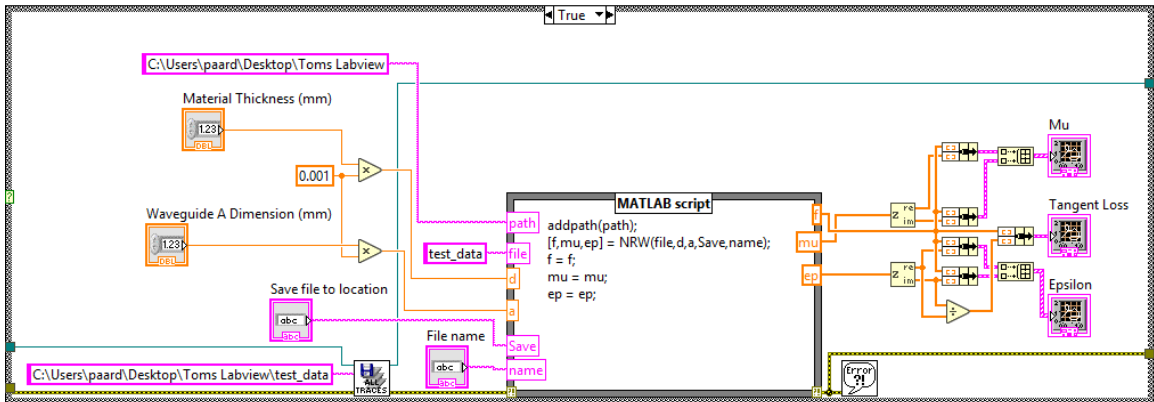


Figure 3.17: Take Measurement

As shown in the above figure, the extraction algorithm is not performed in Lab-View. Instead, the LabView control software runs a script node that calls a designated

MATLAB function. This requires both programs to be on the computer operating the system, as well as for a MATLAB bootstrapper to run constantly in the background. The benefit to this setup however, is that the computations required for the post processing are unnecessarily difficult to accomplish in LabView, and the data can be taken directly from the output of the control software and input into a MATLAB program that can run the post-processing again. This is particularly useful, since MATLAB is used so heavily at the Radar Innovations Lab, so plotting and processing data is user-friendly. Once the user chooses to take a measurement, they will then have the opportunity to specify the file name and location to which they would like to save the measured data.

### 3.2.6.4   Data Visualization

After the data is measured and the material parameters are extracted, it is instantly displayed to the user in the form of three plots. They display the permittivity, permeability, and the tangent loss calculated from the material measurements. Additional functionality was added to aid the user in the form of interactive cursors. These allow the user to scroll through the data or specify a particular frequency of interest to view the measured value at that point. The data is also exported, ready to be taken into MATLAB or the users program of choice to plot it as desired. Alternatively, the user can also right click on the graph to open a prompt to save the current measurements as a .eps file.

### 3.2.6.5 User Help

The final features that will be covered are those that are geared towards helping or instructing new users. There are three buttons in the lower left-hand corner of the program labeled "Calibration Setup," "Examples," and "Matlab Code." Each of these buttons will link the user directly to a PowerPoint presentation geared toward assisting them understand the functionality of the system, the algorithms that are used behind-the-scenes, as well as examples of different materials that have been measured. This code block is shown below in Fig. 3.18.
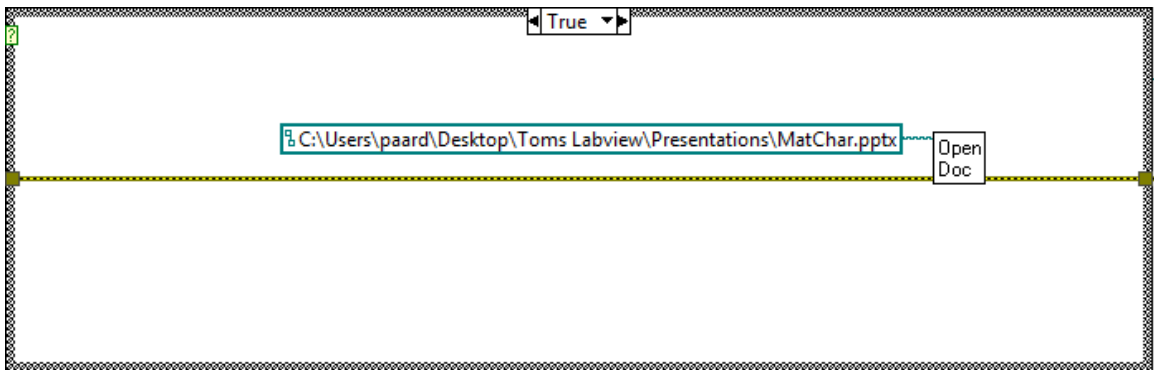


Figure 3.18: User help button

## 3.2.7 Results

To validate the system, a wide variety of materials have been tested and error analyses performed. These include "traditional" dielectric substrates, 3D printed plastics, and even concrete. In each of the figures below, the real and imaginary components of the measured permittivity will be shown on a single plot. Because of the speed at which these tests can be taken with different samples and sample orientations, each of the

plots include several tests taken together of the same material. The calculated mean is also shown in the figure, as well as the maximum difference in measured value seen from over any one sample over the frequency band of interest.
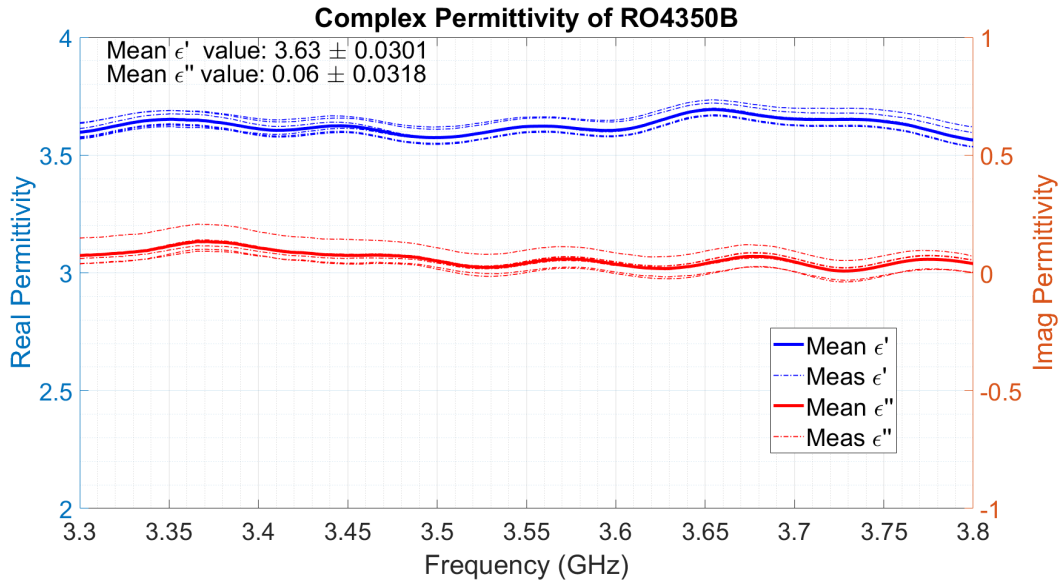


Figure 3.19: Permittivity measurements of RO4350B, taken with waveguide characterization system, expected $\epsilon_r = 3.66$

The first measurement to be discussed is of Rogers RO4350B, a well known dielectric with a design dielectric constant of $\epsilon_r = 3.66$ and a dissipation factor of $\tan\delta = .0031$. The measured results are shown in Fig. 3.19 and Fig. 3.20.
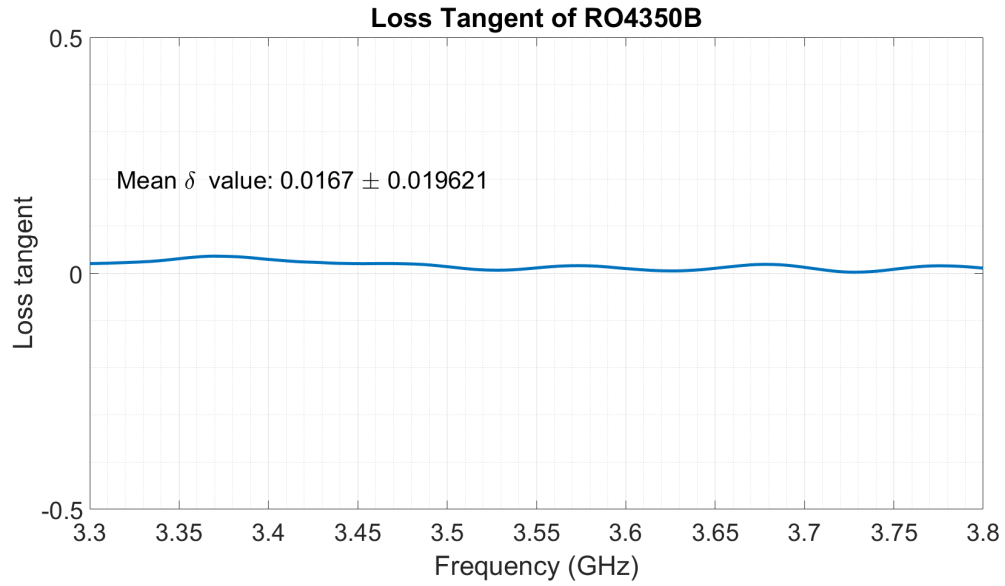
Figure 3.20: Tangent loss of RO4350B expected $\tan\delta = .0031$

In addition to measurements of traditional dielectrics, several more unique materials were tested for a variety of applications. This includes 3D printed dielectrics, milled artificial dielectric layers (although the results are not shown here), and construction materials. Several samples were taken with different consistencies of concrete and water, and the results are shown below for the first sample:
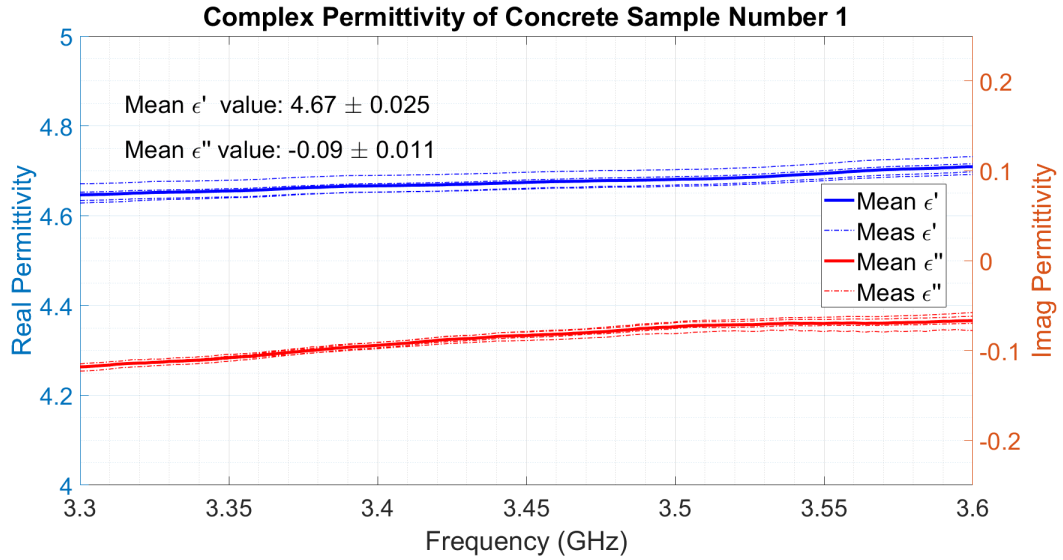
Figure 3.21: Concrete sample 1, permittivity measured with waveguide characterization system, approximate expected value $\epsilon'_r = 4.5 - 5$

The permittivity of concrete blocks is often considered to be around 4.5, though this can vary from 2.5 - 7 F/m depending on the constitution of the concrete [89].
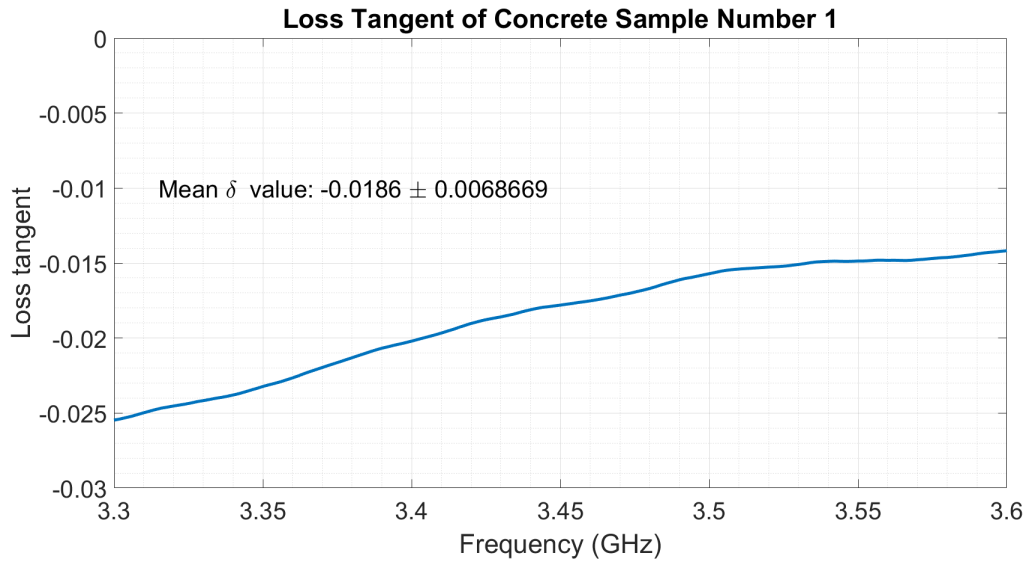


Figure 3.22: Concrete sample 1, tangent loss measured with waveguide characterization system
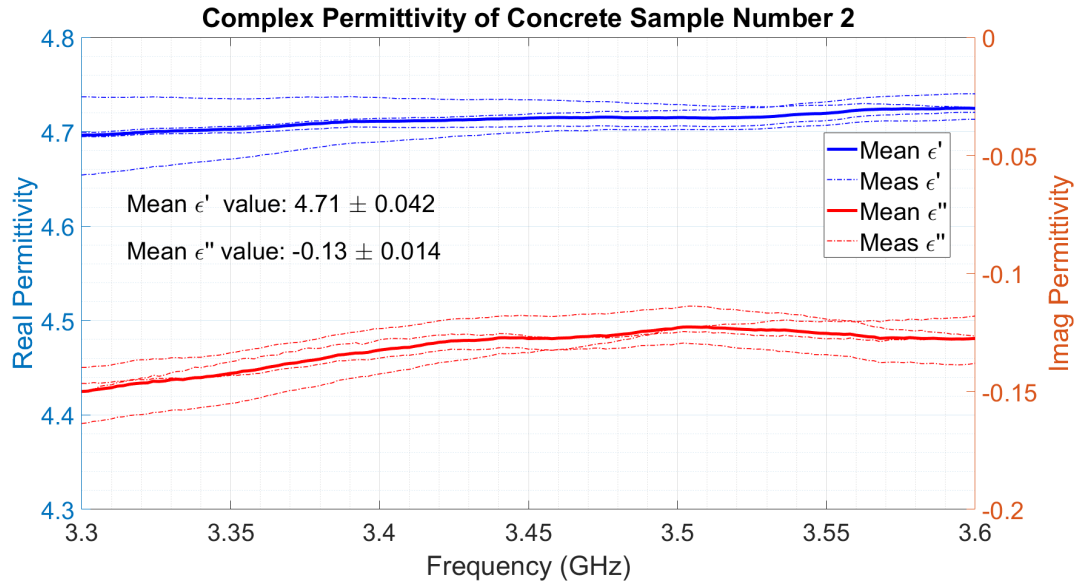
Figure 3.23: Concrete sample 2, permittivity measured with waveguide characterization system
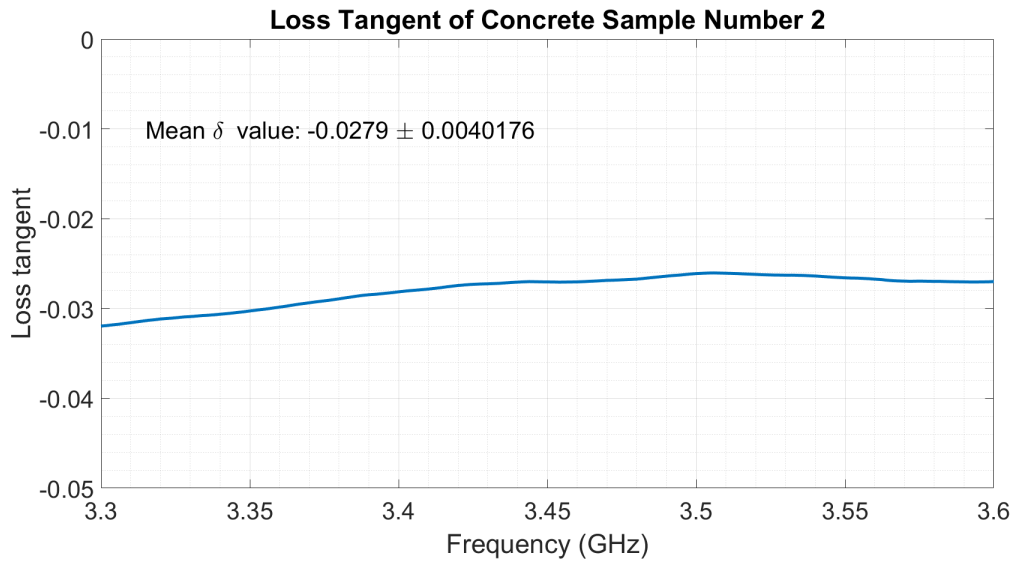


Figure 3.24: Concrete sample 2, tangent loss measured with waveguide characterization system

The third sample had a slightly different consistency, which forced the author to use adhesive to keep the sample from moving while measurements were taken. This did not appear to have a significant impact on the quality of the measurements taken:
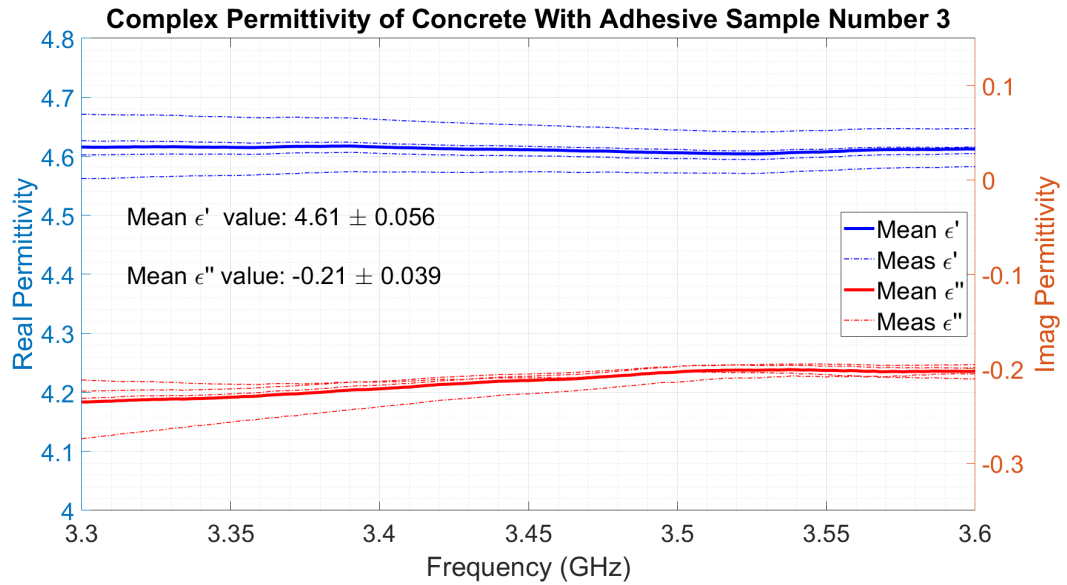


Figure 3.25: Concrete sample 3, permittivity measured with waveguide characterization system
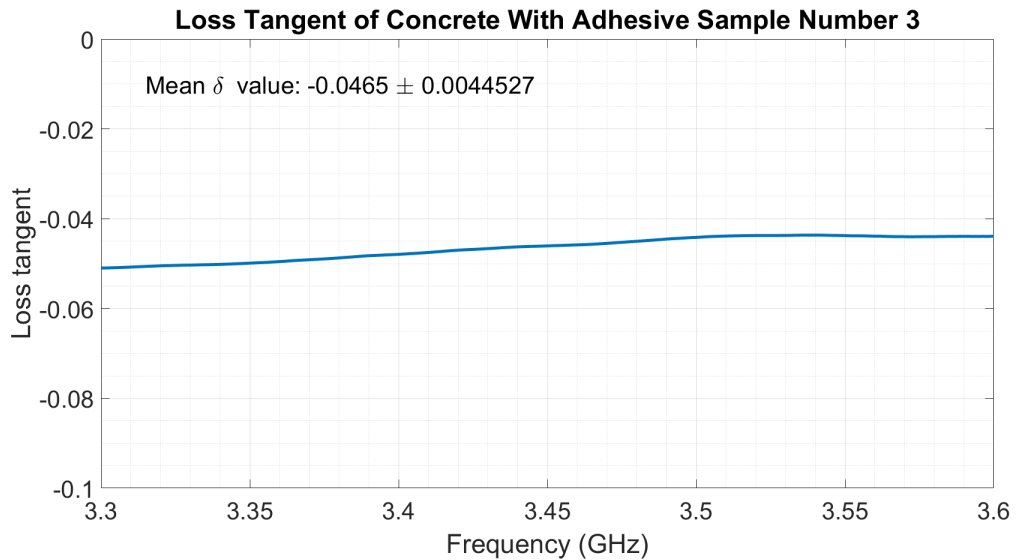


Figure 3.26: Concrete sample 3, tangent loss measured with waveguide characterization system

The fourth concrete sample had a much different composition than the other three presented in that it was also made with gravel and small stones. This resulted in an overall lower dielectric constant.
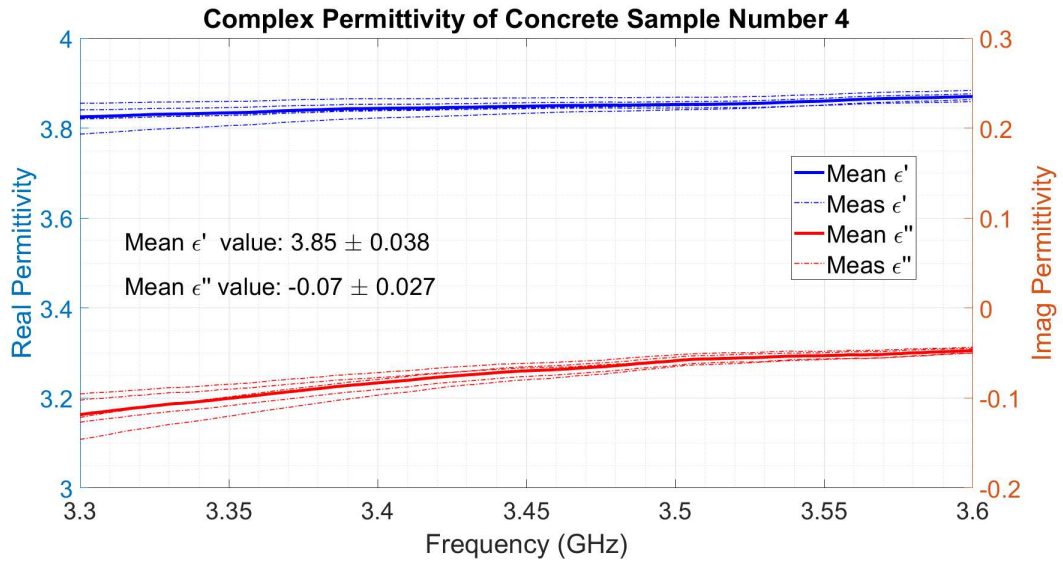


Figure 3.27: Concrete sample 4, permittivity measured with waveguide characterization system
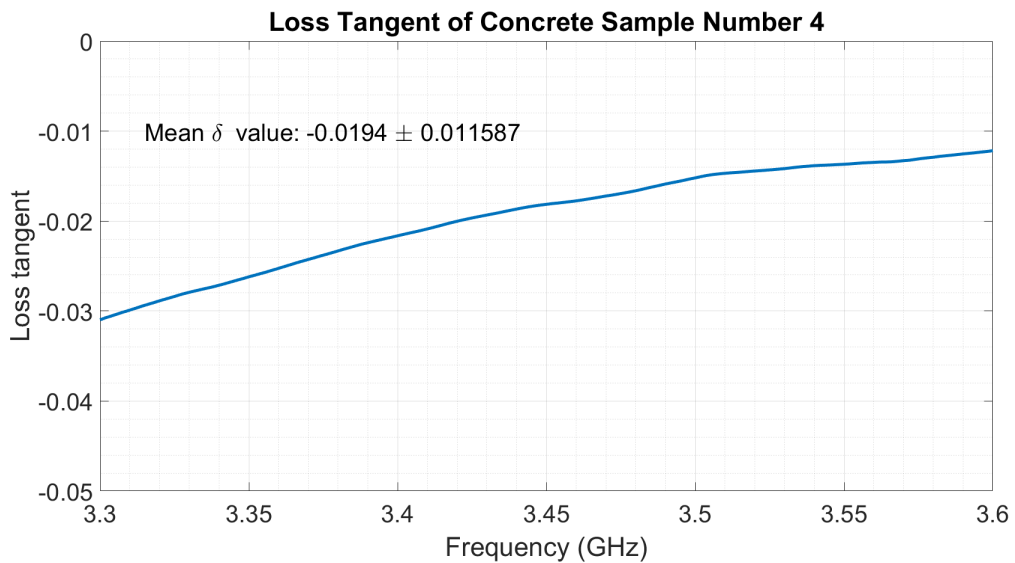


Figure 3.28: Concrete sample 4, tangent loss measured with waveguide characterization system

In these measurements, a slight upward trend of the measured values versus frequency is seen. While the causes have not been completely quantified, gaps between the sample and the sample holder, which induce a strong capacitive effect that increases with frequency, are believed to be the culprit.

The next measurements to be presented are of a 3D printed substrate that will eventually be used for an integrated filter. The material used was PLA with 100% printing. The complex permittivity of PLA is described in [90] and [91] to have a real component around 2.70 - 2.75 and an imaginary component from 0.017 - 0.041. These sample was measured with the waveguide material characterization setup, and the results are shown below.
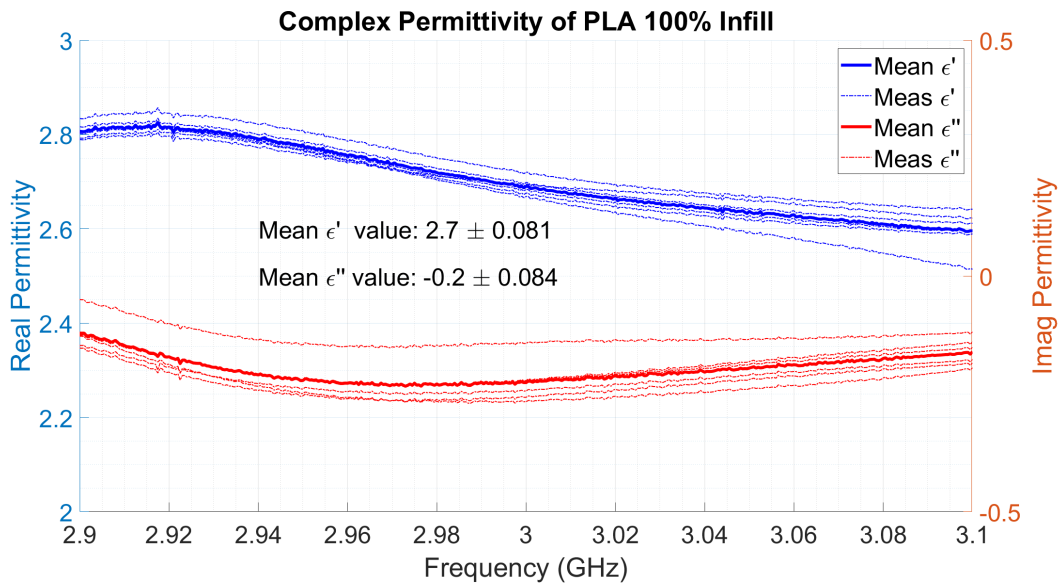


Figure 3.29: 3D printed PLA measured permittivity expected $\epsilon_r = 2.70$
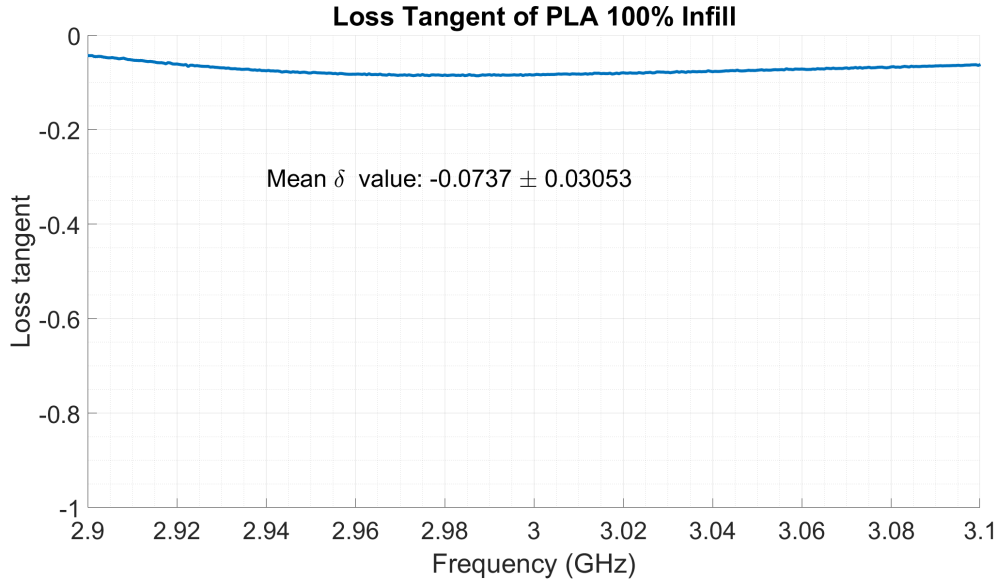
Figure 3.30: 3D printed PLA measured tangent loss

### 3.2.7.1 Error Analysis

While taking measurements with this system, it was noted that errors appeared in the calculated permeability and permittivity, particularly that the values were higher than expected. To attempt to determine the cause of these errors, HFSS simulations were performed of the WG system while introducing possible sources of error, two likely sources were identified.

The setup for the waveguide simulation is shown below in Fig. 3.31. The structure is made of perfect electrical conductor (PEC) and includes models of the flange of the waveguide and the sample holder. The length of the WG is much larger than the wavelength to ensure there are no effects from proximity to the excited ports. The simulated results are then input into the same NRW algorithm used to extract material parameters from measured results.
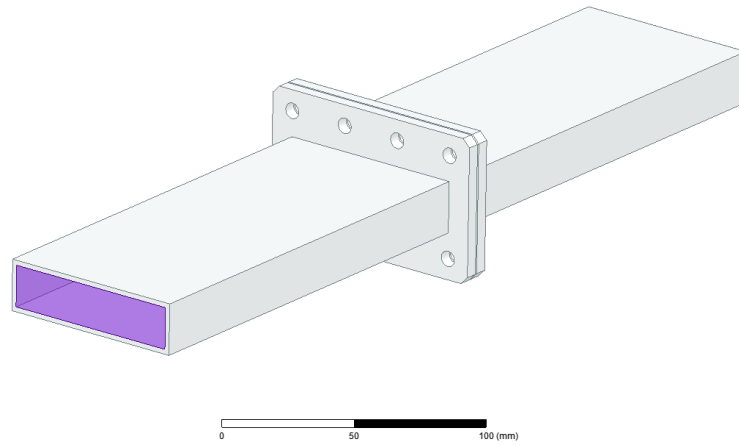
Figure 3.31: Waveguide error analysis simulation setup

The first error source that was identified were gaps between the ports of the waveguide and the sample holder itself. These could easily be introduced while taking measurements on the physical system by not aligning the mounting screws correctly or not tightening them sufficiently. An exaggerated depiction of this error setup is shown below in Fig. 3.33. The simulation was then run over multiple gap sizes for several sample thicknesses. These sample sizes correspond to the sample holders that are presently available for use with this system, as shown below in Fig. 3.32.
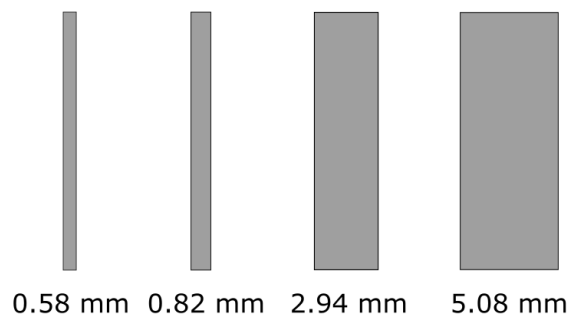


Figure 3.32: Waveguide sample slide sizes
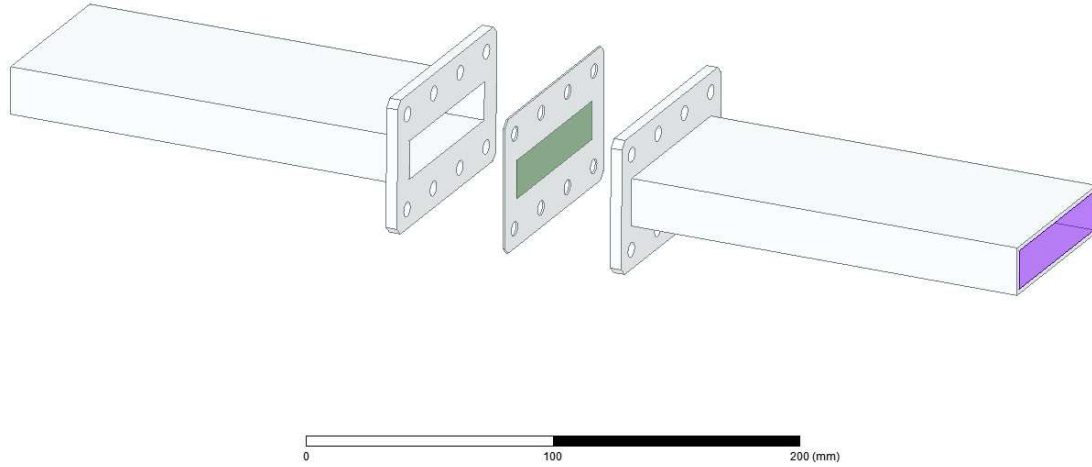
Figure 3.33: Waveguide simulation with gaps between sample holder

After sweeping through a variety of gap distances, a set of three realistically small gaps were selected. The results for the extracted material parameters for each thickness will be presented below, followed by a table outlining the maximum error seen for each parameter.
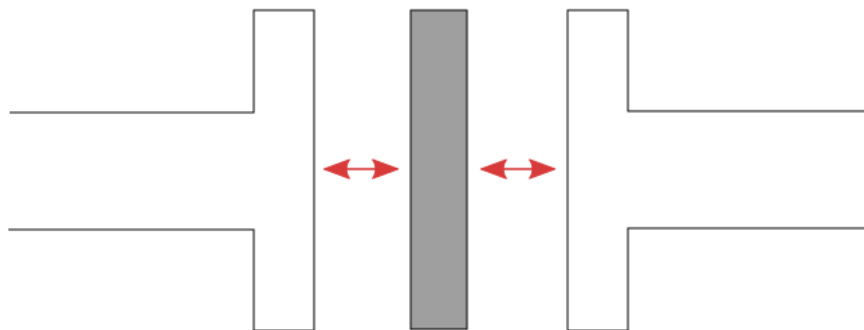


Figure 3.34: Illustration of gap location
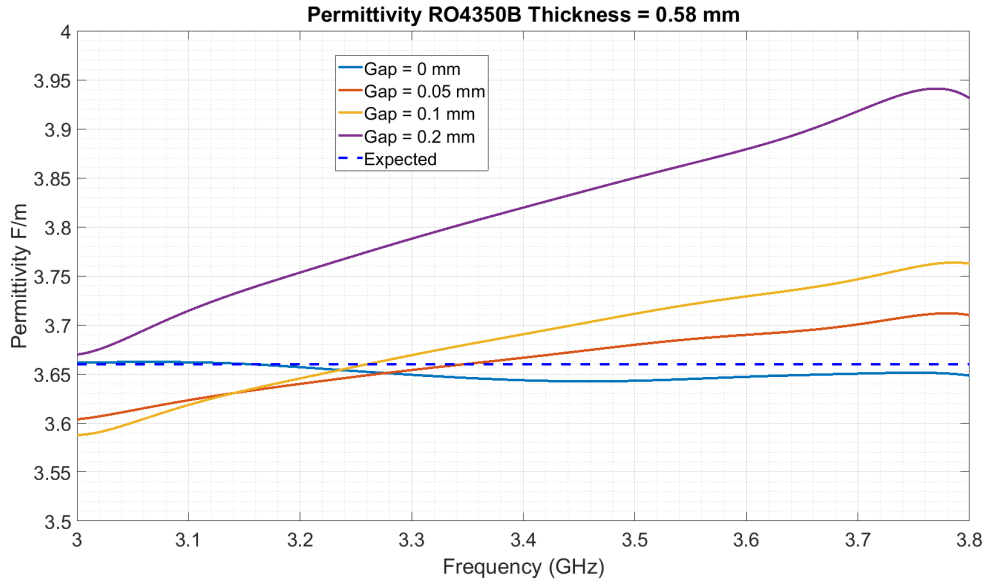
Figure 3.35: Extracted permittivity of 0.58 mm thick sample HFSS simulation

The upward shift in the extracted permittivity matches the effects seen in some measurements. While perfect matching is not seen, the results below show better matching as the sample thickness increases. A summary of the error values seen for this sample is shown below in Table 3.2

Figure 3.36: Extracted permeability of 0.58 mm thick sample HFSS simulation
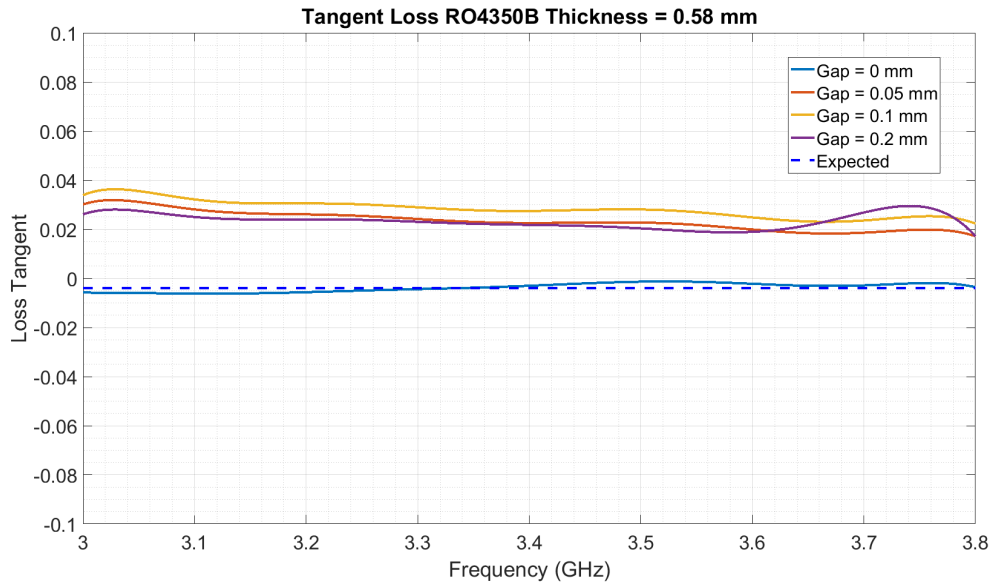


Figure 3.37: Extracted loss tangent of 0.58 mm thick sample HFSS simulation

It is notable that the percentage error seen in the loss tangent of the material is quite high. This is due, in part, to the extremely small expected value of $\tan\delta =$

$-4 \times 10^{-3}$, so that any small variations in value will result in large percent error. However, errors in permittivity, which is almost always the parameter of interest, perform much better, especially in the ideal case with no gap where less than 1% error is observed.

Table 3.2: Gap induced error for thickness = 0.58 mm

| Thickness = 0.58 mm | | | |
|---|---|---|---|
| **Expected** | $\epsilon = 3.66$ | $\mu = 1$ | $\tan\delta = -4 \times 10^{-3}$ |
| **Gap size** | **Max % error** $\epsilon$ | **Max % error** $\mu$ | **Max % error tan** $\delta$ |
| Gap = 0 mm | 0.34 % | 8.32 % | 68.71 % |
| Gap = 0.05 mm | 1.75 % | 26.10 % | 891.19 % |
| Gap = 0.1 mm | 3.19 % | 52.94 % | 1000.80 % |
| Gap = 0.2 mm | 8.07 % | 107.62 % | 833.29 % |

The results for the next thickness, 0.82 mm, is shown below. As discussed before, the error for all metrics is reduced as the thickness of the sample increases.
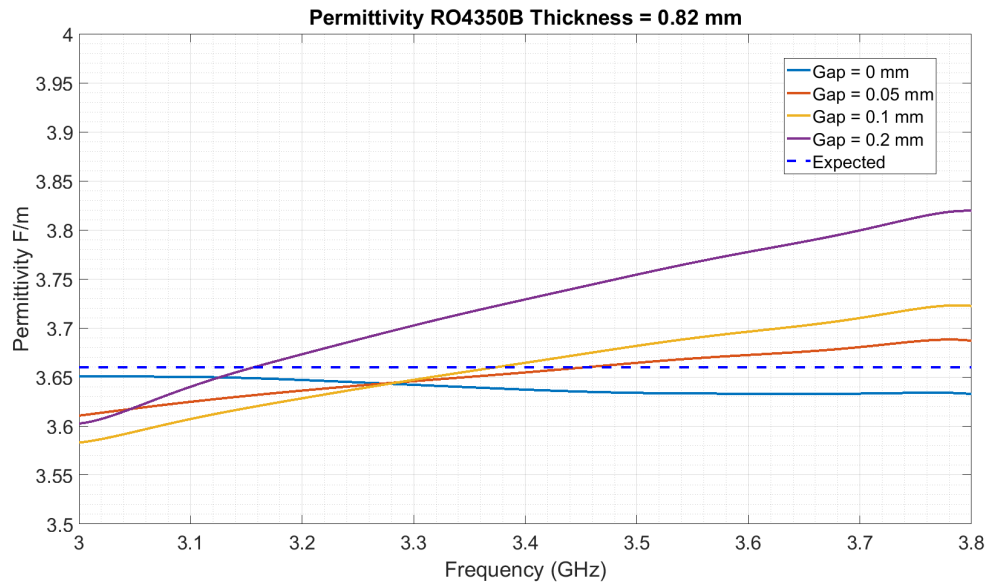


Figure 3.38: Extracted permittivity of 0.82 mm thick sample HFSS simulation

60
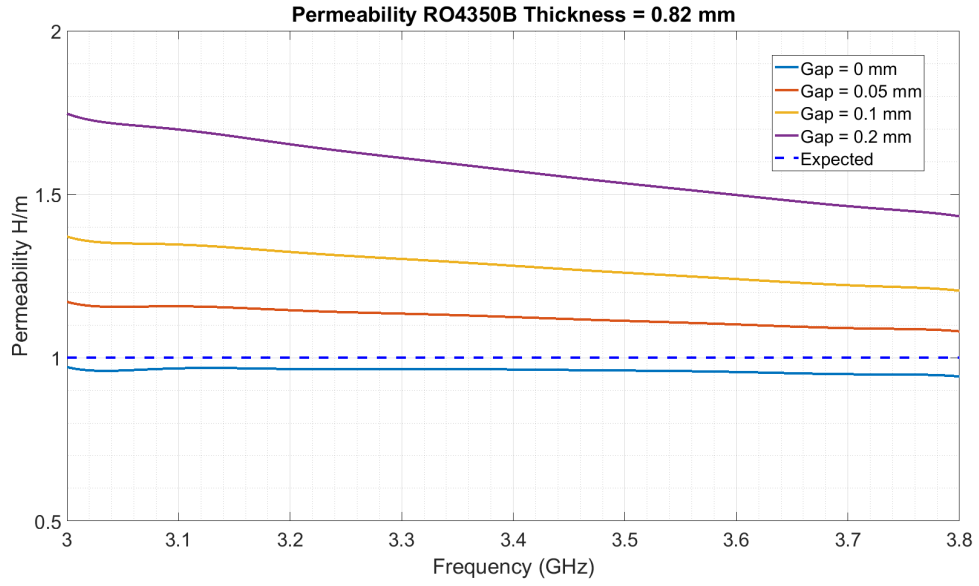
Figure 3.39: Extracted permeability of 0.82 mm thick sample HFSS simulation
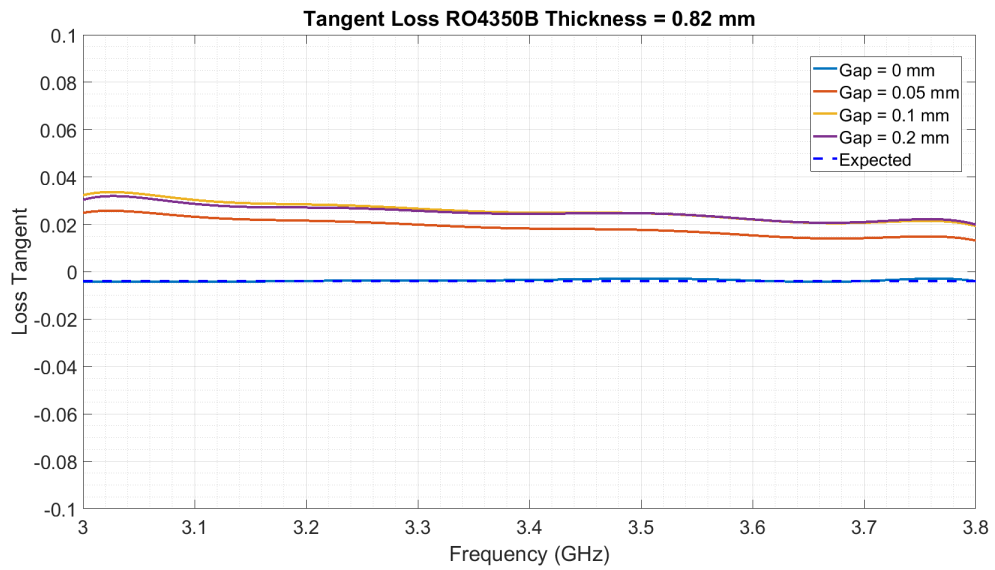


Figure 3.40: Extracted loss tangent of 0.82 mm thick sample HFSS simulation

It is worth noting that the presence of gaps adds considerable errors to the permittivity measurements, which was also observed when taking physical measurements.

Table 3.3: Gap induced error thickness = 0.82 mm

| Thickness = 0.82 mm | | | |
|---|---|---|---|
| **Expected** | $\epsilon = 3.66$ | $\mu = 1$ | $\tan\delta = -4 \times 10^{-3}$ |
| **Gap size** | **Max % error $\epsilon$** | **Max % error $\mu$** | **Max % error $\tan\delta$** |
| Gap = 0 mm | 0.29 % | 5.20 % | 28.44 % |
| Gap = 0.05 mm | 1.30 % | 17.78 % | 735.90 % |
| Gap = 0.1 mm | 2.28 % | 37.86 % | 930.75 % |
| Gap = 0.2 mm | 4.95 % | 75.71 % | 888.44 % |

Additionally, as the gaps increase in size, the effects on permeability and loss tangent grow rapidly beyond an acceptable error level.
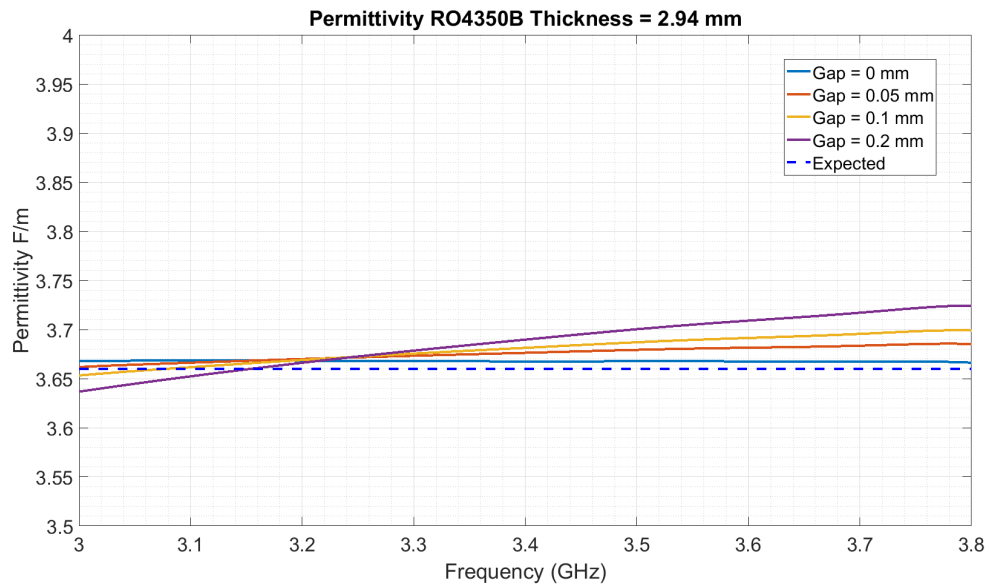


Figure 3.41: Extracted permittivity of 2.94 mm thick sample HFSS simulation
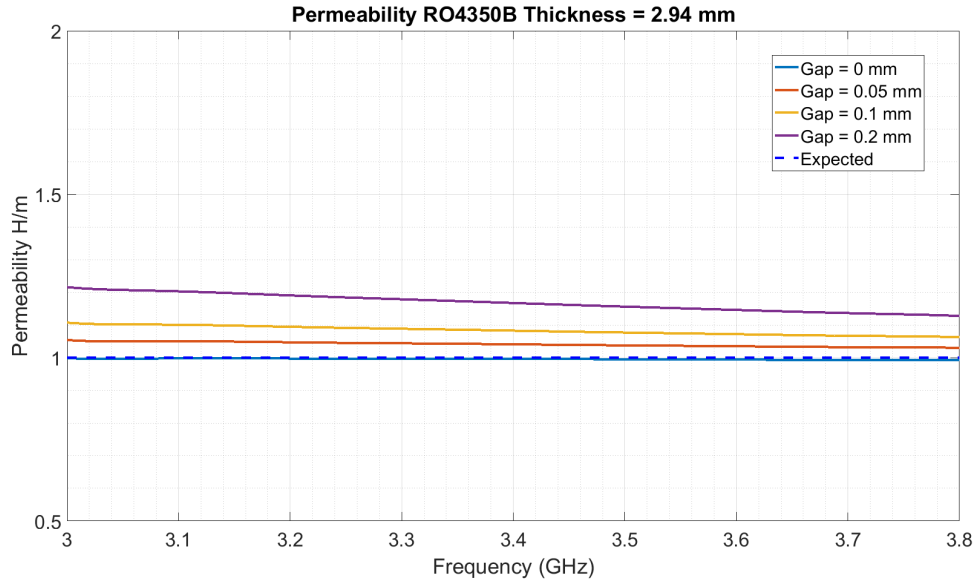
Figure 3.42: Extracted permeability of 2.94 mm thick sample HFSS simulation
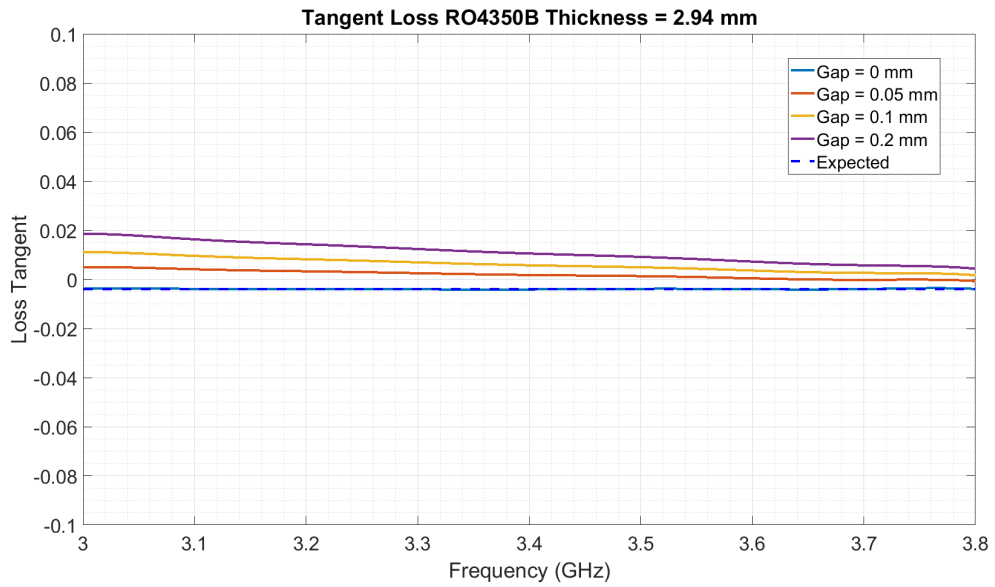


Figure 3.43: Extracted loss tangent of 2.94 mm thick sample HFSS simulation

Table 3.4: Gap induced error thickness = 2.94 mm

| Thickness = 2.94 mm | | | |
|---|---|---|---|
| **Expected** | $\epsilon = 3.66$ | $\mu = 1$ | $\tan\delta = -4 \times 10^{-3}$ |
| **Gap size** | **Max % error $\epsilon$** | **Max % error $\mu$** | **Max % error tan $\delta$** |
| Gap = 0 mm | 0.07 % | 1.03 % | 10.90 % |
| Gap = 0.05 mm | 0.53 % | 5.17 % | 226.74 % |
| Gap = 0.1 mm | 0.90 % | 10.49 % | 379.24 % |
| Gap = 0.2 mm | 1.58 % | 21.33 % | 564.91 % |
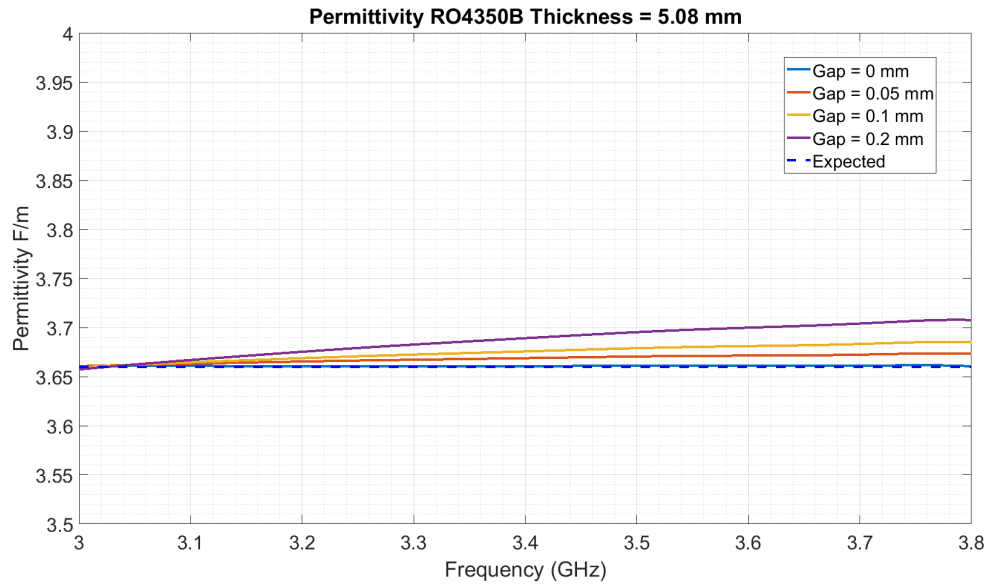


Figure 3.44: Extracted permittivity of 5.08 mm thick sample HFSS simulation
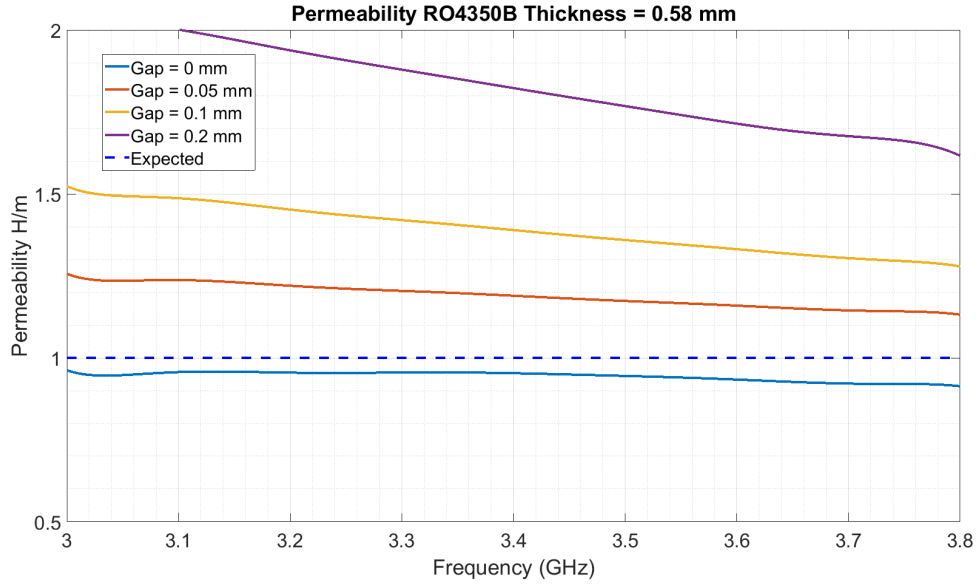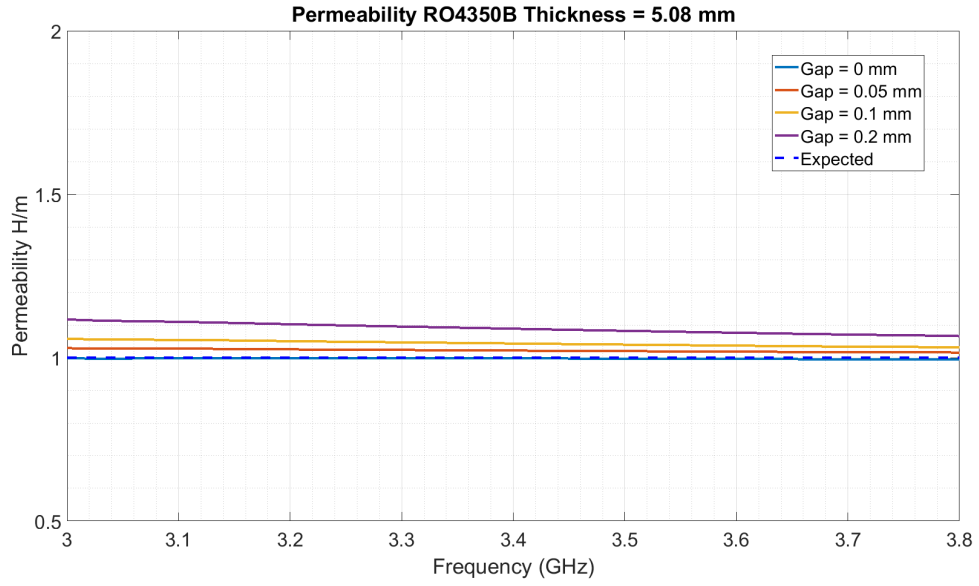
Figure 3.45: Extracted permeability of 5.08 mm thick sample HFSS simulation
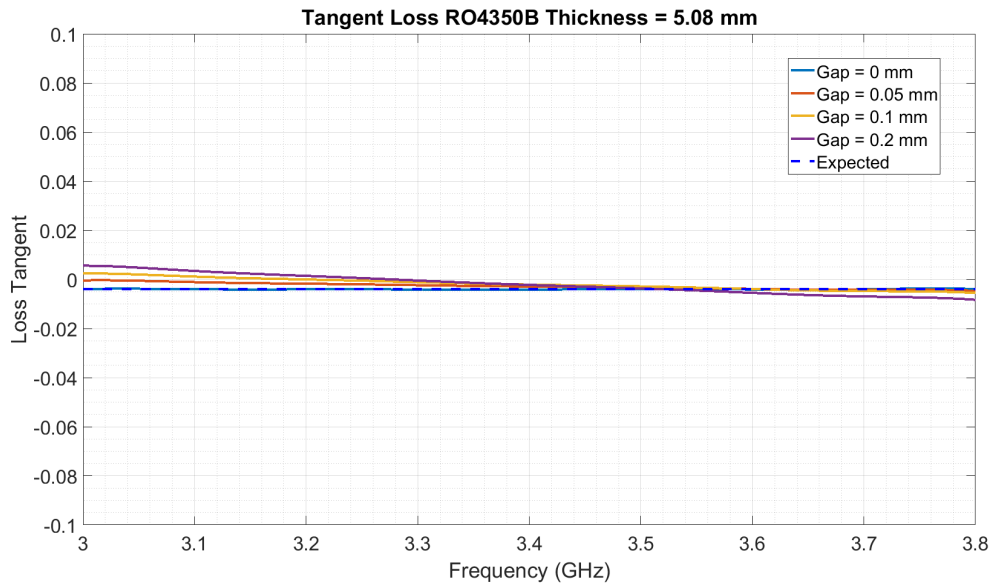


Figure 3.46: Extracted loss tangent of 5.08 mm thick sample HFSS simulation

It can be seen that increasing the thickness of the sample will reduce the effects

of small gaps on the measurements, although this is intuitive, as the gaps will make

Table 3.5: Gap induced error thickness = 5.08 mm

| Thickness = 5.08 mm | | | |
|---|---|---|---|
| **Expected** | $\epsilon = 3.66$ | $\mu = 1$ | $\tan\delta = -4 \times 10^{-3}$ |
| **Gap size** | **Max % error $\epsilon$** | **Max % error $\mu$** | **Max % error $\tan \delta$** |
| Gap = 0 mm | 0.04 % | 0.57 % | 7.75 % |
| Gap = 0.05 mm | 0.38 % | 2.93 % | 91.18 % |
| Gap = 0.1 mm | 0.70 % | 5.84 % | 160.19 % |
| Gap = 0.2 mm | 1.31 % | 11.72 % | 239.05 % |

up a smaller fraction of the volume of the sample as it increases in thickness. The effect of gaps is still significant. This leads us to conclude that proper alignment and tightening procedures must be followed thoroughly and ensuring that there are no gaps present when taking measurements is vital for maintaining accuracy.

The other probable cause of measurement error identified was gaps between the sample holder and the sample itself. This was seen commonly when performing tests, as it is difficult to manufacture a sample to the tolerance where it fits into the sample holder with minimal difficulty and has no gaps present. To evaluate the impact these gaps have on performance, HFSS simulations were run sweeping over different values of gaps. To illustrate these gaps, two figures below are presented. The first, Fig. 3.47 below, shows the normal configuration of the sample within the sample holder.
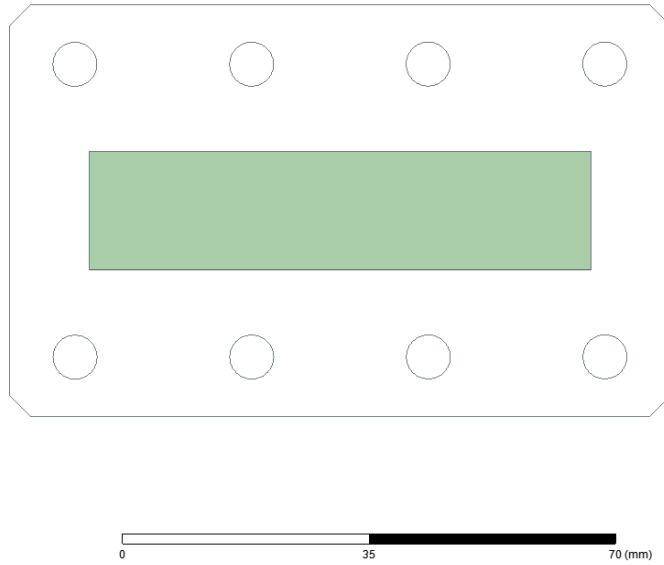
Figure 3.47: Normal sample configuration HFSS simulation

Note that the sample is coincident with the sample holder walls. The new setup, with an exaggerated gap for visualization, is shown in Fig. 3.48 below:
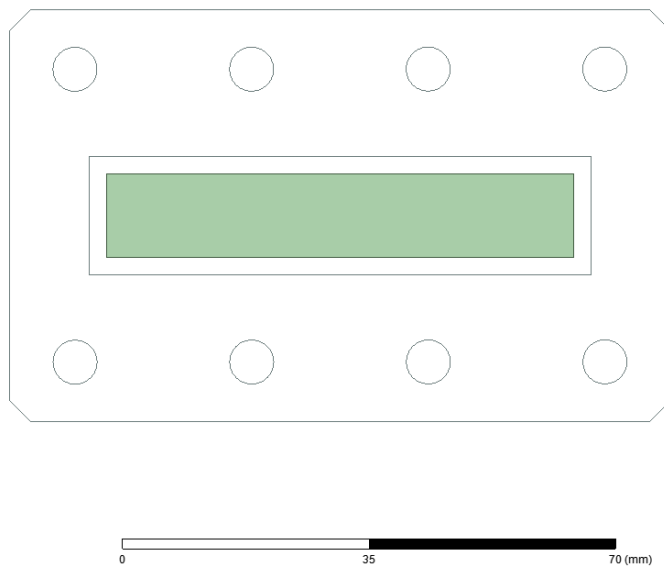


Figure 3.48: Sample holder with gap HFSS simulation

Testing of this setup was done for two thicknesses at the extremes of the chosen values, 0.58 mm and 5.08 mm, over a sweep of the same gap sizes explored before. The 0.58 mm case will be displayed first, with the three extracted parameters shown below in Figs. 3.49 - 3.51.
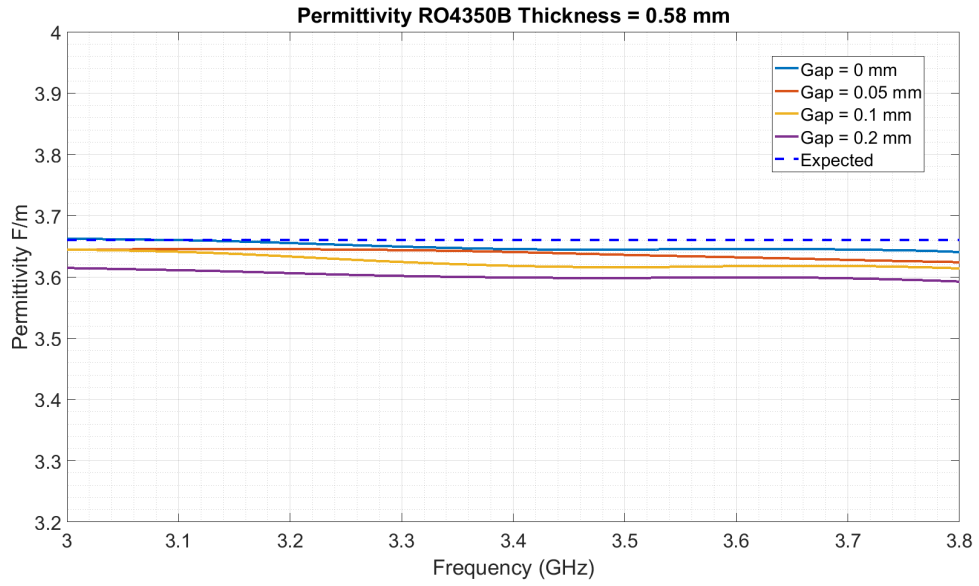


Figure 3.49: Extracted permittivity vs. sample holder gap 0.58 mm thick
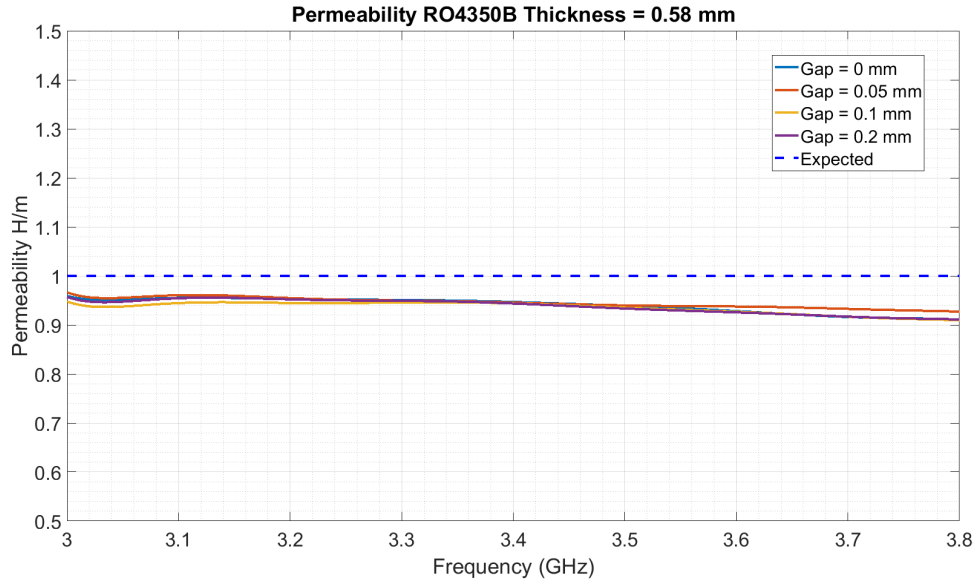
Figure 3.50: Extracted permeability vs. sample holder gap 0.58 mm thick
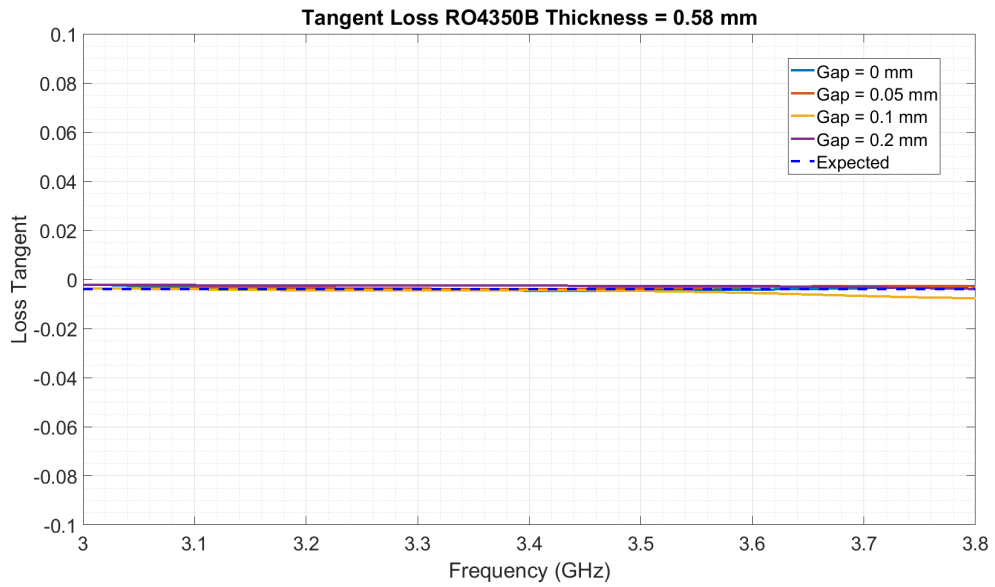


Figure 3.51: Extracted tangent loss vs. sample holder gap 0.58 mm thick

The results for this test show the most dramatic effects on the extracted permit-

tivity. While the other gap had an outsize effect on permeability and loss tangent,

Table 3.6: Sample gap induced error thickness = 0.58 mm

| Thickness = 0.58 mm | | | |
|---|---|---|---|
| **Expected** | $\epsilon = 3.66$ | $\mu = 1$ | $\tan\delta = -4 \times 10^{-3}$ |
| **Gap size** | **Max % error $\epsilon$** | **Max % error $\mu$** | **Max % error tan $\delta$** |
| Gap = 0 mm | 0.53 % | 8.93 % | 47.71 % |
| Gap = 0.05 mm | 0.99 % | 7.29 % | 32.33 % |
| Gap = 0.1 mm | 1.26 % | 9.04 % | 91.42 % |
| Gap = 0.2 mm | 1.85 % | 8.88 % | 42.61 % |

there appears to be little correlation between gaps in the sample holder and an effect

on either. In particular, the error in permeability does not change with gap size and

matches the error inherently seen when applying the extraction algorithm. However,

the effect on permittivity follows a clear pattern, wherein as the gap grows the error

in the permittivity increases, and the overall measured permittivity goes down.
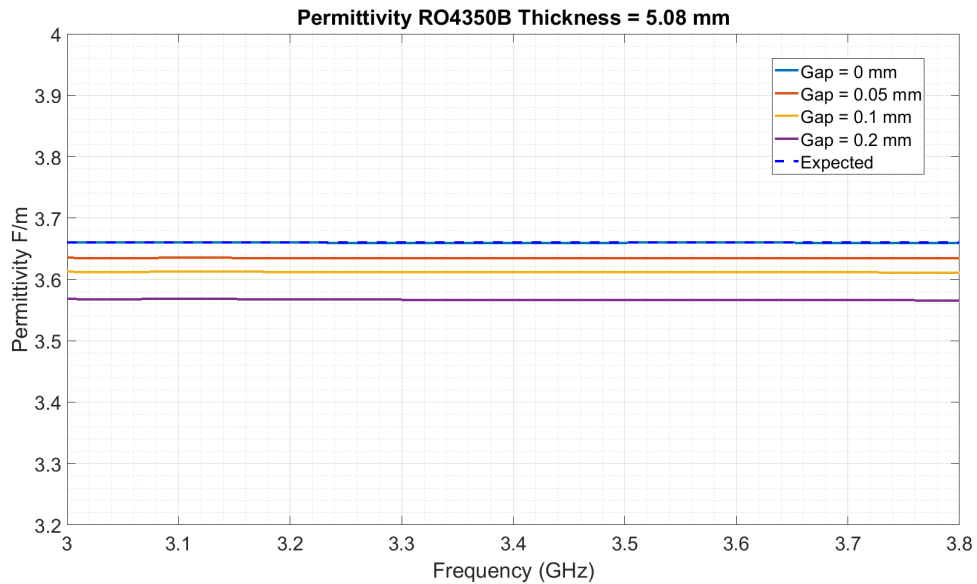


Figure 3.52: Extracted permittivity vs. sample holder gap 5.08 mm thick
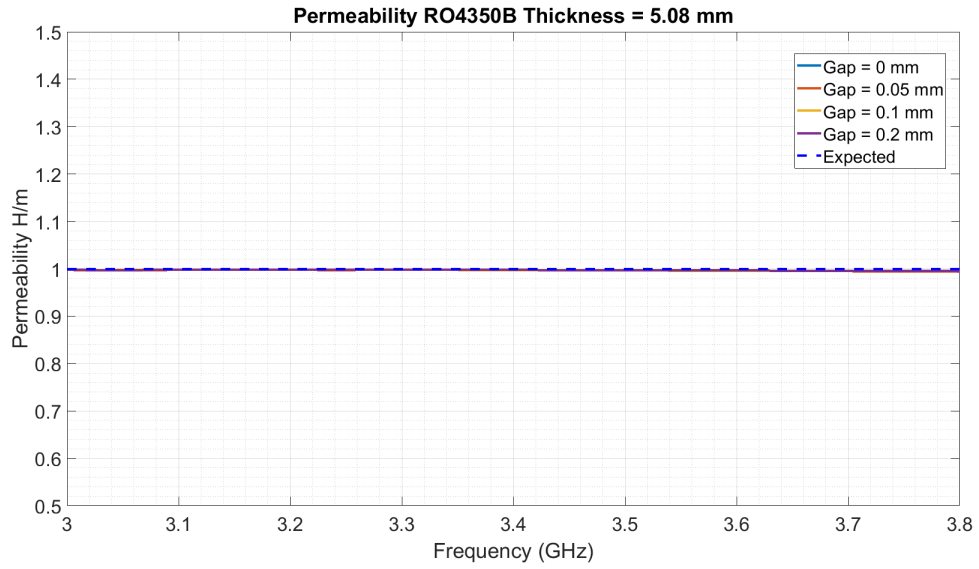
Figure 3.53: Extracted permeability vs. sample holder gap 5.08 mm thick
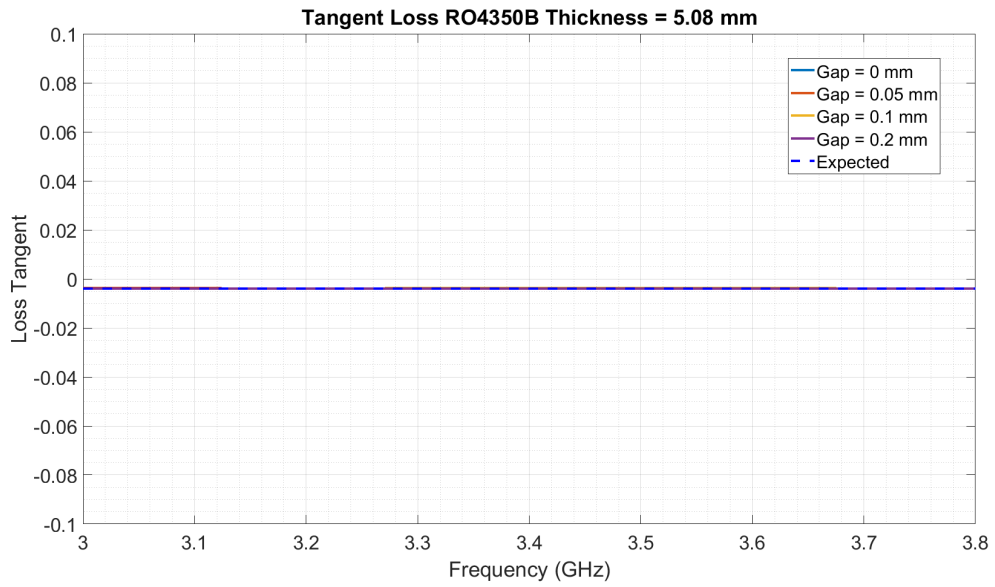


Figure 3.54: Extracted tangent loss vs. sample holder gap 5.08 mm thick

Table 3.7: Sample gap induced error thickness = 5.08 mm

| Thickness = 5.08 mm | | | |
|---|---|---|---|
| **Expected** | $\epsilon = 3.66$ | $\mu = 1$ | $\tan\delta = -4 \times 10^{-3}$ |
| **Gap size** | **Max % error $\epsilon$** | **Max % error $\mu$** | **Max % error tan $\delta$** |
| Gap = 0 mm | 0.03 % | 0.53 % | 2.10 % |
| Gap = 0.05 mm | 0.71 % | 0.57 % | 6.35 % |
| Gap = 0.1 mm | 1.34 % | 0.47 % | 7.31 % |
| Gap = 0.2 mm | 2.58 % | 0.51 % | 3.34 % |

The same pattern observed in the thin sample is seen here. An increase in gap size results in an increase in the error seen in permittivity measurements while loss tangent and permeability are unaffected.

We can conclude that results generally have less variability when a large sample is used. However, for all thicknesses the introduction of gaps between the waveguide ports and the sample will result in significant errors in all three extracted parameters. If a gap exists within the sample holder - sample interface, the most visible effect will be on the extracted permittivity.

## 3.3 Square Waveguide for Anisotropic Characterization

### 3.3.1 Introduction

While the use of rectangular waveguides for material characterization is well-documented and has been done for several decades, the method still has its drawbacks. Namely,

the measurement of anisotropic materials is difficult to perform. Because of the asymmetrical nature of a rectangular waveguide sample holder, if a sample is prepared for one orientation it cannot be rotated and measured at any other position. This is of particular importance, as the preparation of multiple samples introduces another source of error into the measurements [8]. This is illustrated below in Fig. 3.55:
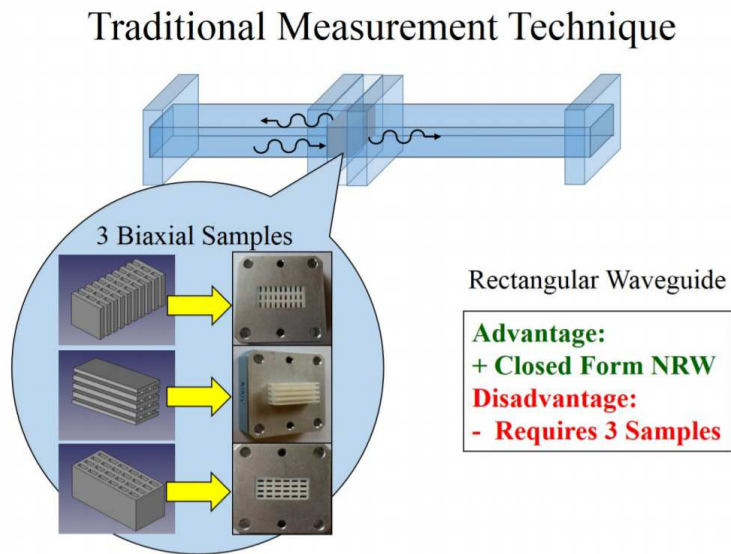


Figure 3.55: Traditional measurement procedure for anisotropic materials [8]

Because the ARRC is interested in the development and testing of artificial dielectrics and metamaterials, both of which can exhibit anisotropic behavior, simulations and testing were performed to develop a method to test these materials from a single sample.

Much of the work done was inspired by the work of Alexander Knisely in 2015, where he describes the construction of a Waveguide Rectangular to Waveguide Square (WRWS) system [34] [26]. This is illustrated below in Fig. 3.56. His work guided many of the decisions made and the algorithms used for material extraction.
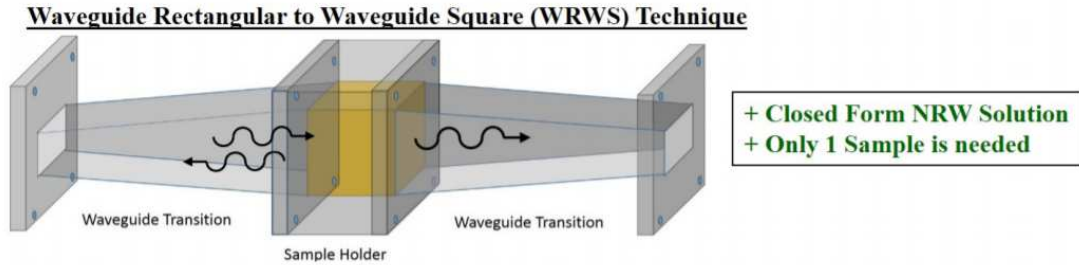
Figure 3.56: Rectangular to square waveguide transition [8]

The main motivation when performing these tests was to utilize the fabrication facilities at the ARRC to create a low-cost method for testing these anisotropic materials at S-band. To this end, the idea was to use the 3D printing capabilities of the ARRC to print two WRWS transitions and a square sample holder and then use electroplating tanks to coat them in copper. Ideally these transitions could then be integrated with the previously described rectangular waveguide-based system and control software to greatly expand the scope of what materials could be measured. Unfortunately, the limitations of our fabrication abilities, algorithm issues, and time did not allow us to completely achieve this.

### 3.3.2 System Description

When starting work to implement a WRWS transition, two main design goals were established: the transition must be fully compatible with the current rectangular waveguide system in use and it must be realizable with the fabrication systems at the ARRC. To meet this first objective, the transitions were all designed to have the exact flange configuration present in the current system. This model is shown below in Fig. 3.57:
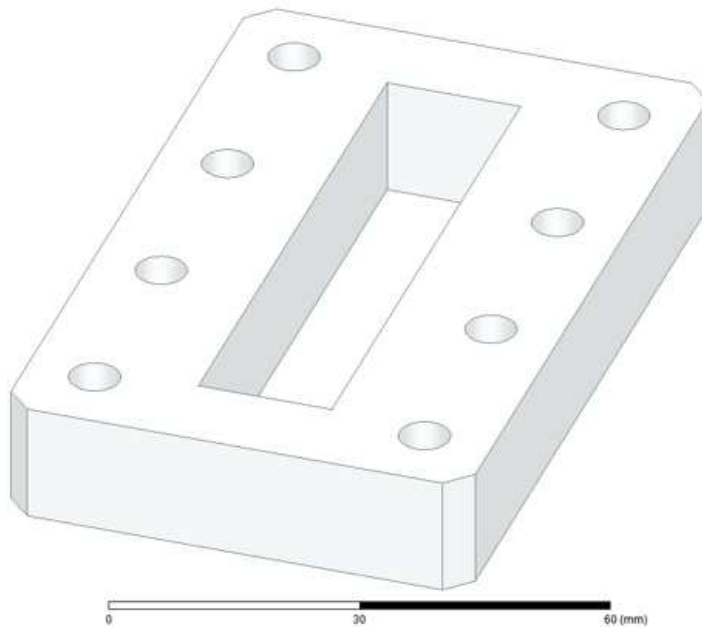
Figure 3.57: Model of flange present in rectangular waveguide

This small section was first 3D printed to show that the flange was compatible with the waveguide set up. This flange was then used as the basis for the connectors used for the WRWS transition that was designed for.

### 3.3.3  Simulations

To design these transitions, ANSYS HFSS was used to perform simulations over the frequency band of interest. The first simulations performed were a proof of concept, did not include thickness and were not physically realizable. This is shown below in Fig. 3.58:
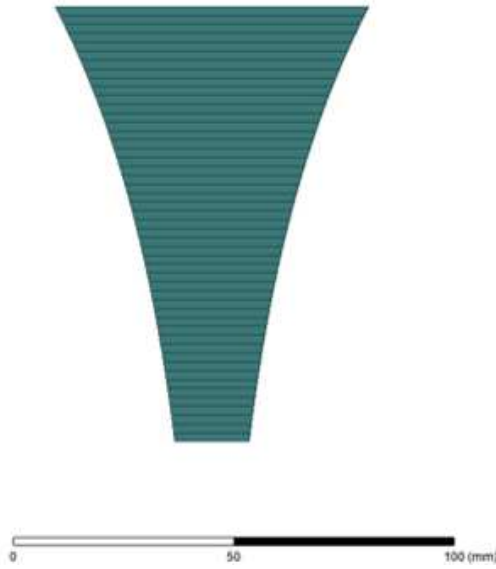
Figure 3.58: Model of WRWS transition geometry

The decision was made early on to use an exponential curve on the interior surface as opposed to the straight transition employed by Knisley. This was due to the reflections seen at the input of the transition, which were reduced over the band of interest by implementing a curved surface. The higher reflections were due, in large part, to the size constraints from the fabrication methods available. This will be discussed more extensively in section 3.3.5.

After verifying the performance of a single WRWS transition, the full system was also simulated with two transitions, a square sample of material, and the two feeding waveguides. This full setup is shown below in Fig. 3.59.
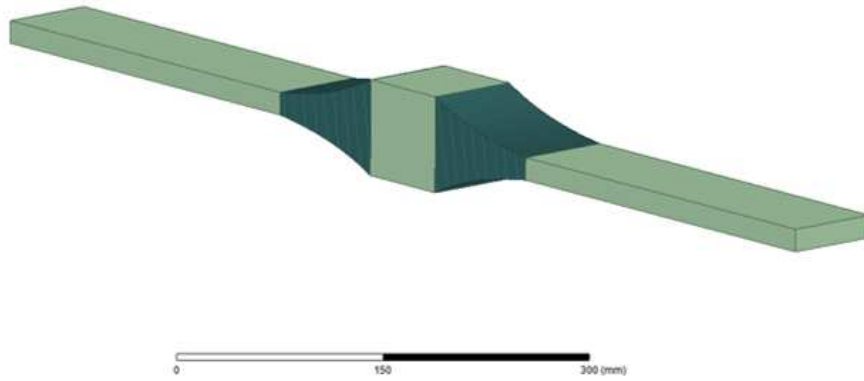
Figure 3.59: Model of WRWS system

After verifying the performance of this system, development of a physically realizable WRWS began. The first version of this transition is shown below in Fig. 3.60:
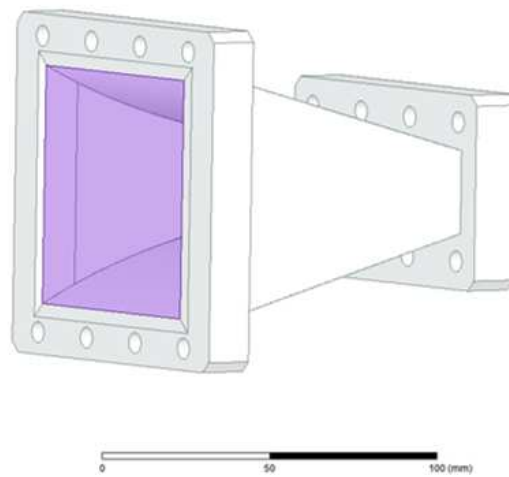


Figure 3.60: Model of WRWS version 1

The interior and exponentially curved surface is better illustrated in Fig 3.61 below:
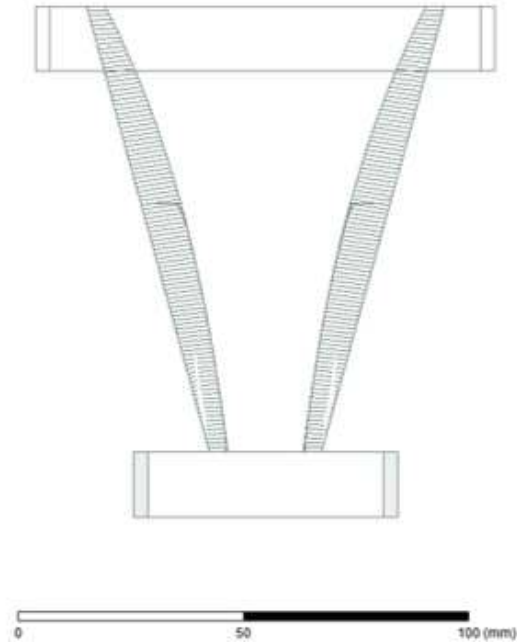
Figure 3.61: Model of WRWS system interior

Unfortunately, fabrication difficulties proved to be extensive, with the flange on both sides becoming deformed during the printing process. This prompted a thorough redesign of the system with an emphasis on being realizable with the resources available. A picture of the flange with damage to the square waveguide portion is shown below in Fig. 3.62
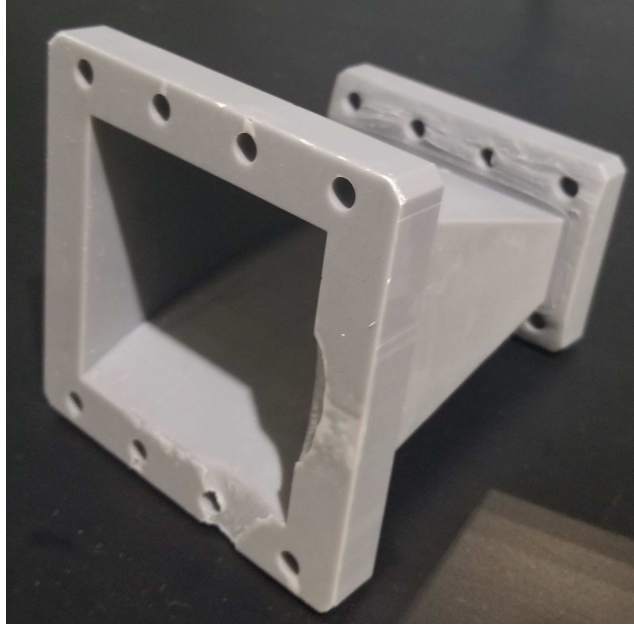
Figure 3.62: Damaged WRWS transition

This resulted in the creation of a second design, shown below in Fig. 3.63. A new curved flange was added to the smaller port, and the larger port was thickened significantly. Additionally, the larger port had two notches added to allow for the flange to be precisely trimmed after printing. This was a result of the first batch of this new design having significant damage to the flange caused by removal from the 3D printer base which then did not allow for a complete connection between the transition and the sample holder.
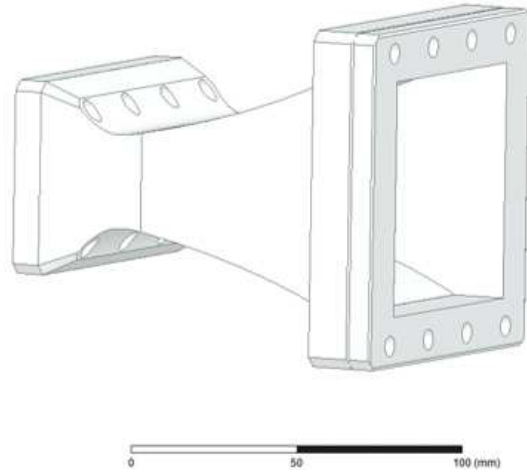
Figure 3.63: Redesigned WRWS transition

This sample holder, which is perfectly square to allow for a single sample to be inserted at all necessary orientations, is shown below in Fig. 3.64:
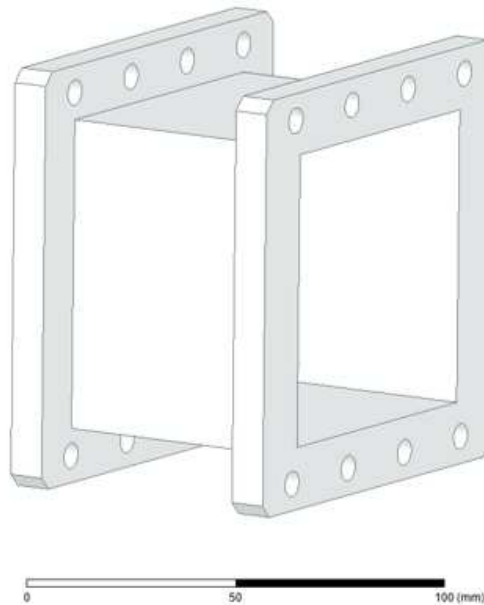


Figure 3.64: Square sample holder

These transitions were printed in the ARRC, but, as will be discussed in section 3.3.5, there were still significant challenges in the system implementation.

The printed transitions are shown below in Figs. 3.65 and 3.66:



Figure 3.65: Redesigned WRWS transition printed



Figure 3.66: Redesigned WRWS transition printed

### 3.3.4 Material Parameter Extraction Method

To extract material parameters from the WRWS system, a modified Nicolson-Ross-Weir technique was used. The main difficulty in implementing this algorithm is the

branching issue discussed earlier. Because the phase of a measurement will wrap around when measuring samples of thickness $> \lambda/2$, a branching algorithm must be developed as shown by Knisley [8]. By using that thesis as a starting point, the algorithm was developed in MATLAB to extract material parameters from simulated values. This proved to be difficult, as the short length of the WRWS transition (a result of the 3D printer used for fabrication) produced more reflections than was ideal. Additionally, a calibration had to be applied to the simulated system, which required measurements for a Thru-Reflect-Line calibration to be taken in HFSS and directly applied to the simulated results.

### 3.3.5 Fabrication Constraints

The biggest difficulties that were faced when fabricating these designs were the 3D printers used and the copper plating. The printer that was chosen for the design was the FormLabs Form2 3D printer. This printer has a maximum print area of $5.7 \times 5.7 \times 6.9$ in ($14.5 \times 14.5 \times 17.5$ cm) and a laser spot size of 140 microns [92]. This created the maximum size of any printed structure we could fabricate. There were significant difficulties in getting acceptable performance from this printer. The first being the finishing quality on the structure. The portion of the WRWS transition that was in contact with the printing plate often had serious bubbles or divots develop, which forced us to plan cutting at least some portion of the transition off after printing. This presented its own challenges, as even with a channel put into the design to guide the saw, achieving a perfectly flat transition was challenging. Any shift in the flatness of the transition would prove devastating, as air gaps existing between the waveguide

sections will introduce an unacceptable amount of errors. This could have been rectified with the use of support materials; however, the software from FormLabs that runs the printer does not support user customized support structures. Because of this, one must trust the software to decide where supports are necessary. For this specific part, the software felt that supports must be placed internally. This is also unacceptable, as it is impossible to completely remove the stubs of the support scaffolding except through extensive sanding, which then itself results in a non-uniform surface. As a result, support structures could not be used and the inner surface of the printed WRWS transition was uneven. The performance that resulted was less than ideal and generated issues with the copper plating.

Once the structure is printed, it must be plated in copper for it to be able to function as a waveguide. This proved to be problematic in our case. To achieve a uniform copper distribution, the part must be entirely submerged in the plating liquid and a uniform current distribution must be achieved. This requires the application of copper tape around the part in such a way as to force current to distribute evenly throughout the part. Unfortunately, this proved to be extremely difficult to achieve even in smaller and simpler parts. The weight of the printed transition, plus its complicated geometry, combined to be what proved to be an insurmountable challenge. When attempting to plate the part, the copper distribution was uneven and often the interior of the part was left completely unplated. Despite numerous attempts, the part was never successfully plated to a usable degree. Eventually, a combination of monetary and time constraints forced the author to move on from this work to continue automating other systems. Ideally, and as will be discussed in the future

work section, a waveguide transition could be purchased or milled directly from a piece of aluminum or copper as done by [8].

## 3.4 Summary

In this chapter, the automation of a waveguide-based material characterization system is described, as well as upgrades made to the hardware. The behavior of a waveguide is explored with focus on the excitation of higher-order modes. The operation and calibration procedures are detailed along with explanations of the software that is used. The user interface is shown with descriptions of the different modes of operation available to the user. The functionality of the LabView code that runs the user interface is explored, and sections of code are displayed to illustrate how different operational functions are accomplished. The exploration of the use of a WRWS set-up is described through details of the simulation and attempted fabrication of a WRWS transition and sample holder. While there were significant challenges faced in its implementation and it did not produce a working addition the the system, it did serve as a valuable learning experience and provides an opportunity for future work. The material extraction algorithm was developed to work with simulated results from the WRWS setup, and this should ideally transition smoothly to the extraction of measured results in the future. A derivation of the Nicolson-Ross-Weir algorithm, which is used to determine the electrical properties of materials, is also displayed. Material parameter extraction examples follow, including examples of traditional dielectric materials, building materials, artificial dielectric layers, and 3D printed dielectrics. The

potential sources of error in the waveguide setup are also explored. These are presented as two main components, gaps between the waveguide ports and gaps between the samples and the sample holder. Both of these error sources are investigated with the use of HFSS to determine the amount of error added to the measurements when these two effects are occurring. It is shown that gaps between the waveguide ports and the sample induce a significant percentage of error, even with relatively small gap sizes, and these errors align well with the effects seen on physical measurements.

# Chapter 4

# Free-Space Method for Material Characterization

## 4.1 Introduction

In this chapter the implementation of two more material characterization systems is discussed. These two systems will be called the mmWave scanner, a multi-purpose W-band setup that allows for antenna and material characterization, and the three-probe or anisotropic scanner, which, as the name suggests, has a third probe that can move independently of the other two to characterize materials at oblique angles of incidence at C and X-band. Both of these systems utilize the free-space transmission-reflection method for material characterization.

## 4.2   mmWave RF Scanner

### 4.2.1   Introduction
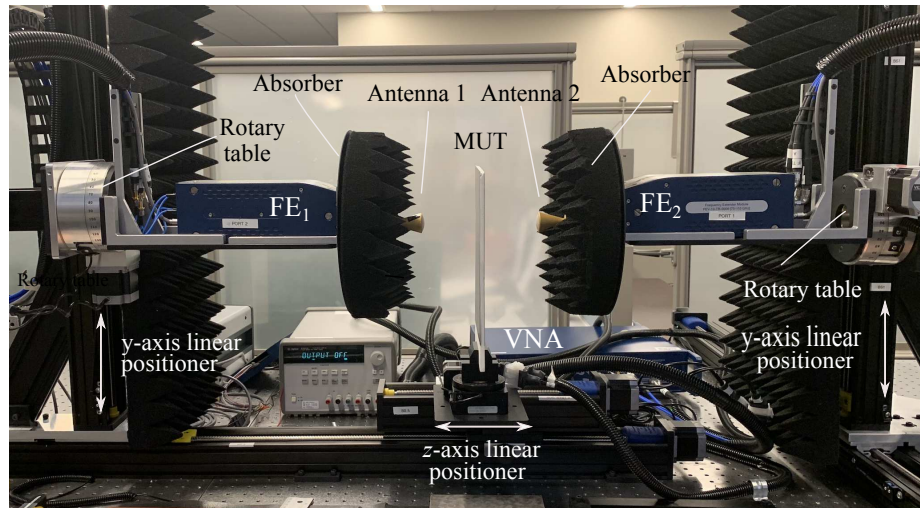


(a)
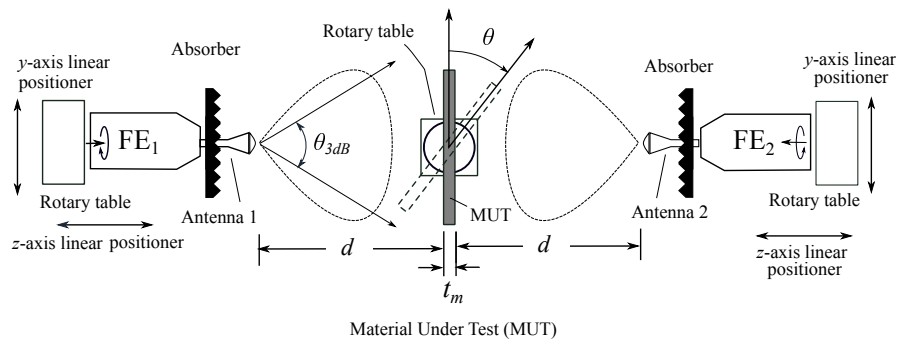


(b)

Figure 4.1: mmWave scanner full setup [9]

The mmWave scanner was designed by the PAARD to facilitate rapid testing for phased arrays at W-band (75-110 GHz). It is a multi-purpose tool that has several modes of operation depending on the required test. While these will be discussed further in a later section an, overview of the possible modes of operation are as follows: far field, planar near field, and material characterization. This is accomplished

by making the test setup reconfigurable and utilizing linear actuators. The control software and mechanical design for this device was a product of the collaboration between several very talented engineers and students, namely Chris Clark, Jonathan Christian, Dr. Rodrigo Lebron, Kevin Constien, Dr. Zeeshan Qamar, and Dr. Jorge Salazar. The author's contribution to this work was in handling the interface of the VNA and control software, as well as implementation of the material characterization mode. The use of the mmWave scanner for material characterization has also been described in [9] by members of the PAARD.

## 4.2.2 System Description

The mmWave system is composed of 5 linear actuators and 4 rotary tables which are used to position the probe, antenna under test, and/or material sample and take a variety of measurements. Two motors each run off of a Velmex motor controller, which is used to interface with, and receive commands from, the desktop that the control software is located on. The rotary tables allow for rotation of the AUT and probes, for both co-polar and cross-polar measurements, as well as rotation of a material under test for characterization off broadside. The entire system is mounted on an optical table that allows for reconfiguration of the system, as needed. This table also contains the VNA, power supplies, and motor controllers. The system utilizes a Copper Mountain C4209 VNA which can natively go to 9 GHz, as well as two FEV-10 frequency extenders which allows the VNA to operate from 75-110 GHz. This is ideal, as the system was originally designed for testing automotive radars at 77GHz.

### 4.2.3 Modes of Operation

The mmWave scanner has three main modes of operation: far-field antenna measurements, near-field antenna measurements, and material characterization. The first to be discussed is the far-field mode. While far-field testing of many radar systems at lower frequencies requires a large range or anechoic chamber, or is generally unfeasible; testing high frequency systems and arrays is quite possible in a confined space. A common rule of thumb for determining the far-field R is:

$$R > \frac{2D^2}{\lambda} \tag{4.1}$$

Where $\lambda$ is the wavelength and D is the largest dimension of the antenna. Also $R >> D$ and $R >> \lambda$. Because arrays at these frequencies are often quite small in size, and the wavelength is similarly small, it is possible to reach the far-field range of these antennas within the dimensions of the optical table.

To take a far-field measurement with the mmWave scanner, one must mount the AUT on the uppermost rotary table. The measurement probe is then positioned, using a laser level, to be in the same plane as the antenna. The antenna is powered on, and the rotary table is able to rotate the AUT for a complete 360° cut of a plane of the antenna. The probe can be rotated 90° to measure both the E and H planes of an antenna.

The final mode of operation is for material characterization. For this mode, two identical probes must be mounted on each frequency extender. Great care must be taken to ensure that both probes are equidistant from the material sample. While

the algorithm that is used for parameter extraction, the code for which was written by Dr. Zeeshan Qamar, uses all four S-parameters and averages between the "like" parameters, eg. $S_{11}$ and $S_{22}$ or $S_{21}$ and $S_{12}$, the algorithm is still extremely sensitive to anything more than very slight differences in distance. This is due to the extremely short wavelength of the frequency of operation, which results in phase wrapping issues when misaligned by even a fraction of a millimeter. Utilizing a laser level, precision calipers, and the machine's ability to store its position accurately resolves this issue.

Once correct alignment has been achieved, taking measurements in this mode of operation is very simple. One must only open up the material characterization user interface and trigger a measurement. Measurements can be taken at oblique incidences as well, although the lack of a third probe to capture the reflected component of the impinging wave (as discussed in the next section on the three-probe scanner) the measurements will have a degradation in accuracy. This system is suitable for measuring isotropic materials at high frequencies

## 4.2.4   GUI Additions

A key goal of the work done on the mmWave scanner was for the creation of a user interface that will expedite the measuring process and eliminate some of the wasted time inherent in manual measurement and post-processing. This GUI operates independently of the interface that controls the machine motion and antenna scans. The user interface is pictured below in Fig. 4.2:
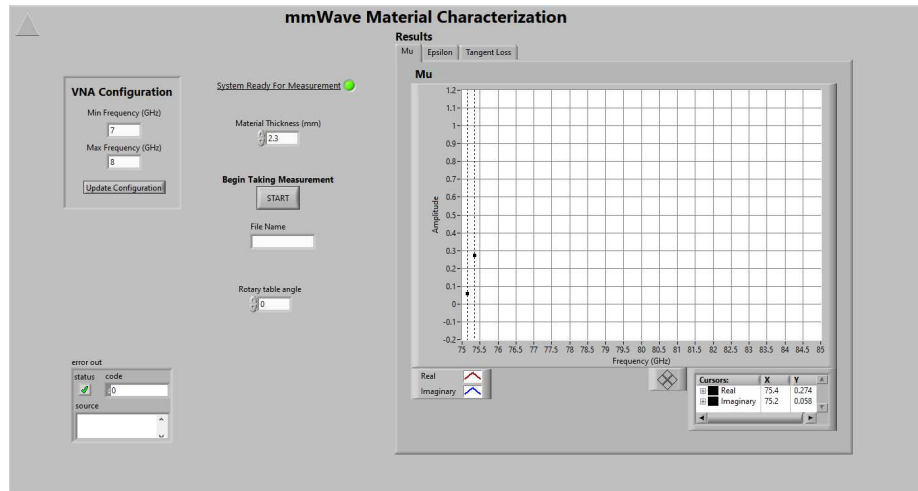
Figure 4.2: mmWave LabView GUI

This interface is user-friendly and serves a valuable role in facilitating fast and accurate measurements. The main features of the GUI are as follows: configuring VNA, triggering VNA to take and store data, processing data rapidly through integration with MATLAB, visualizing data, and control of rotary table motion.

Much of the architecture for this user interface is quite similar to the author's previous work on the guided-wave and free-space three probe scanners. However, changes had to be made to fit the mmWave scanner more effectively.

Configuring the VNA is fairly straightforward. Another Copper Mountain VNA is used for this system, which means that the included LabView library can still be used. Therefore, the user can easily specify the frequency range of interest and then quickly reconfigure the VNA. When the code initializes, the required traces for the implemented material extraction algorithm are automatically applied. For the mmWave scanner, this means that eight traces will be active: the real and imaginary components of each of the four S-parameters.

Triggering the VNA is similarly straightforward. Taking a measurement is as simple as sending a SCPI command via LabView that instructs the VNA to take a measurement as well as where the received data will be stored.

The data is then immediately processed with an instance of MATLAB that runs through LabView. The four-parameter algorithm is applied, using the frequency data from the measurements, as well as the user-specified material thickness, and the extracted material parameters versus frequency are then saved, and simultaneously sent back to LabView for display.

The same interactive graphs that are used for the guided wave system are used here, and allow for the user to trace over the output data to observe values at specific frequency points. The extracted permittivity, permeability, and tangent loss are displayed to the user. This allows the user to rapidly check that the measurements they have taken follow expected results, time is not wasted running post-processing scripts manually, wherein the discovery of a poor measurement may result in time lost.

The rotary table that the material sample is mounted in can also be controlled through the user interface.

## 4.2.5 Results

Because of the situation that, at the time of writing, is ongoing with respect to the Covid-19 outbreak, complete testing of this system was not possible. However, for illustrative purposes, results from several materials taken previously by Dr. Zeeshan Qamar with the mmWave scanner will be presented.

Three materials were measured and the results will be presented below. These materials are: Rogers 5880, Tachyon 100G laminate, and Taconic TLX laminate. A summary of the results is shown below in Table 4.1, where $\sigma$ represents the standard deviation, followed by plots of the measured results.

Table 4.1: Measured results mmWave scanner

| Material | Expected $\epsilon$ | Mean Measured $\epsilon$ | $\sigma$ Real | $\sigma$ Imag |
|----------|---------------------|--------------------------|---------------|---------------|
| RT5880 | 2.20 - 0.000198j | 2.2548 - 0.0177j | 0.012 | 0.0034 |
| Taconic TLX | 2.60 - 0.0049j | 2.6076 - 0.0050j | 0.0054 | 0.0035 |
| Tachyon 100G | 3.02 - 0.0063j | 3.0578 - 0.0416j | 0.0063 | 0.0045 |
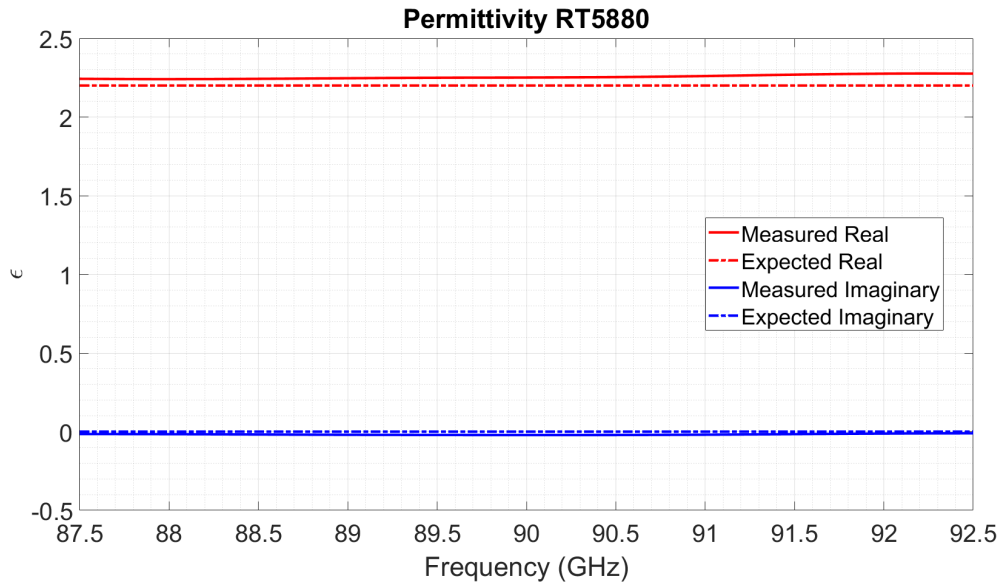


Figure 4.3: Rogers 5880 measured permittivity expected $\epsilon_r = 2.20$
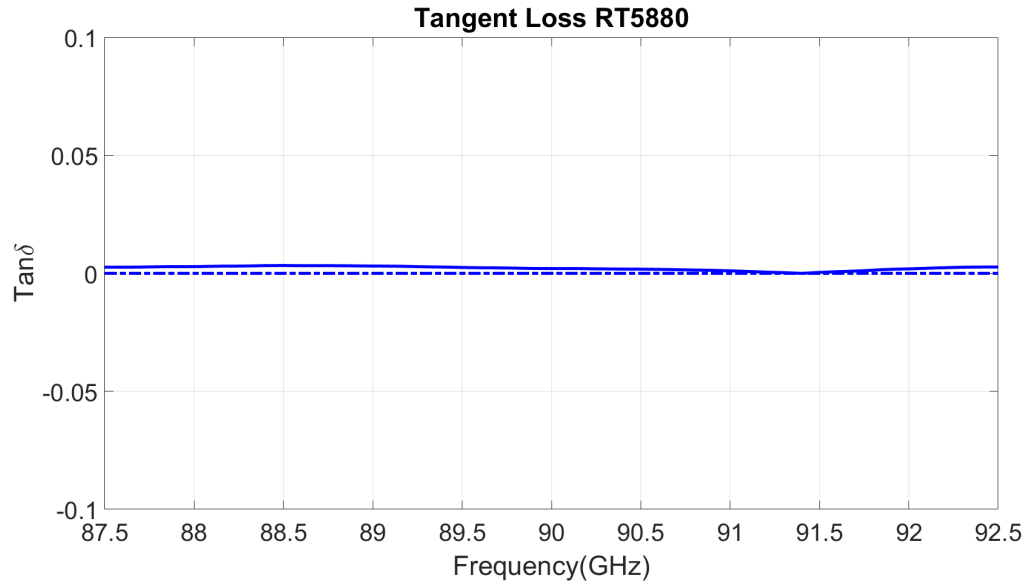
Figure 4.4: Rogers 5880 measured tangent loss expected $\tan\delta = 0.0009$
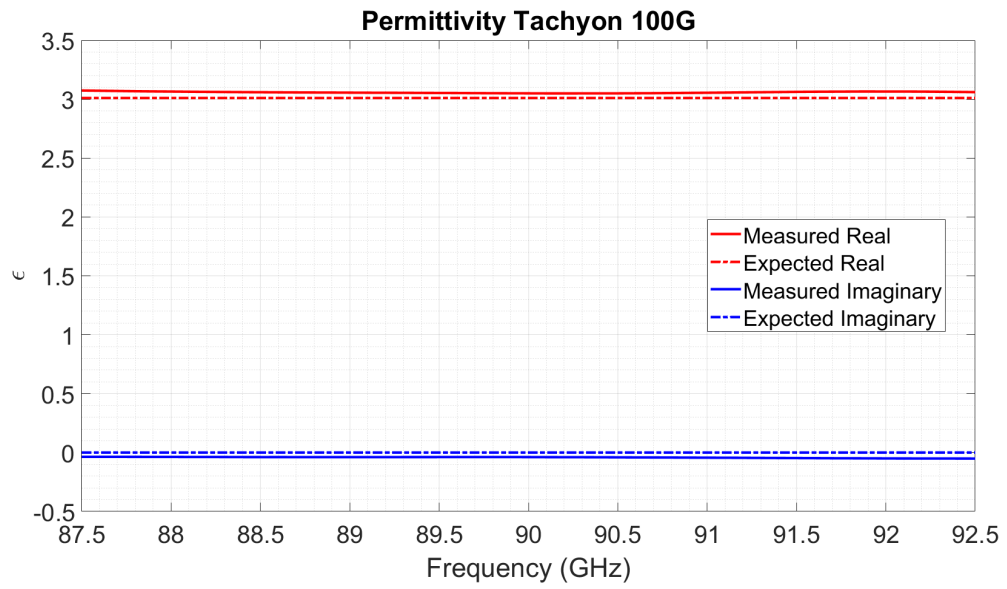


Figure 4.5: Tachyon 100G measured permittivity expected $\epsilon_r = 3.02$
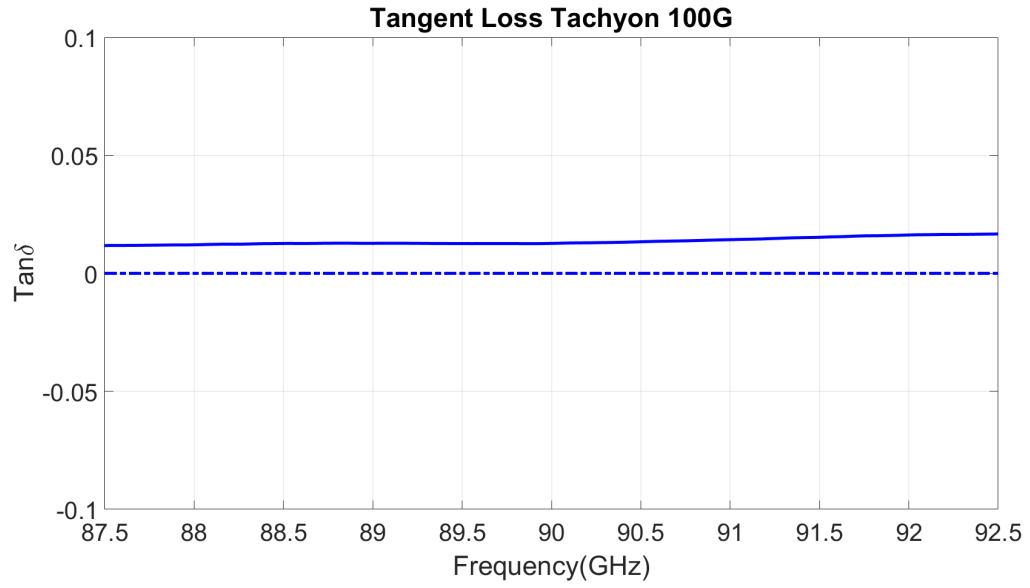
Figure 4.6: Tachyon 100G measured tangent loss $\tan\delta = 0.0021$
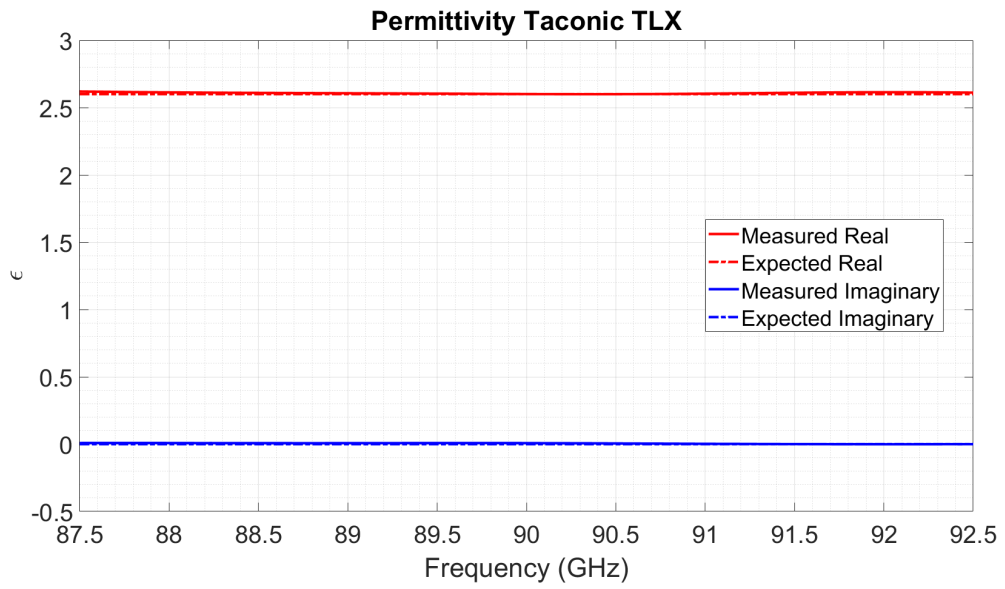


Figure 4.7: Taconic TLX measured permittivity expected $\epsilon_r = 2.60$
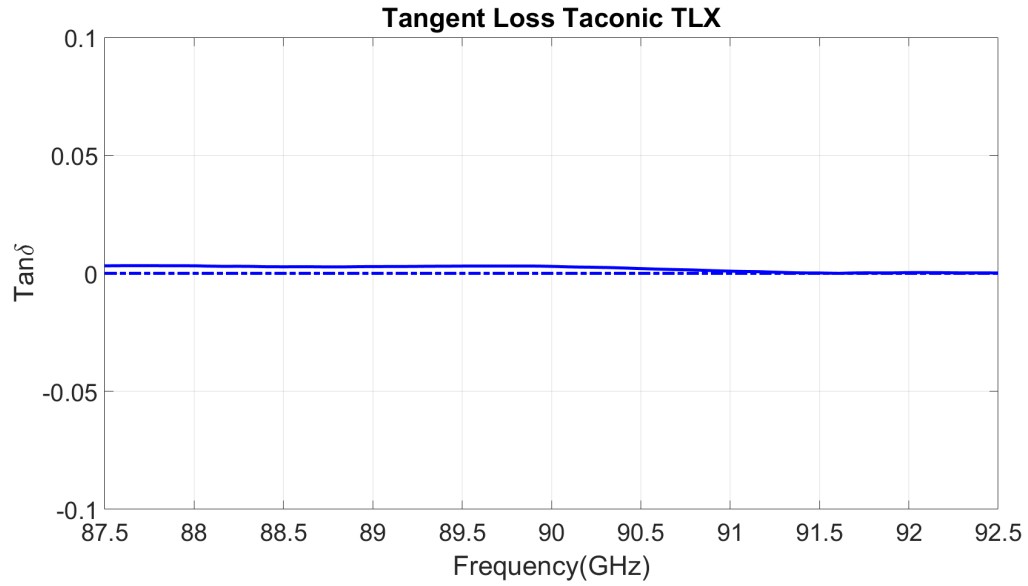
Figure 4.8: Taconic TLX measured tangent loss $\tan\delta = 0.0019$

Good matching to the expected values is observed in all three tests. There is a slight upward shift in all of the measured permittivity values, although this has been observed occurring when the sample is slightly misaligned rotationally. Because of the extremely small wavelength the scanner operates at, even infinitesimal changes to the position of the probes or the rotation of the sample holder has dramatic effects of the measured results.

## 4.3 Three-Probe Method for Anisotropic Material Characterization

### 4.3.1 Introduction

The three-probe anisotropic material characterization system is the last scanner that will be presented. This scanner is the result of hard work from two other students, Joel Love [10] and Alexander Stringer [2], without whom the author would not have been able to complete this project. The mechanical design and early testing was done by Mr. Stringer, and integration of the system with the control boards was done by Mr. Love. The authors primary goal on this aspect of his work was integrating the numerous small LabView scripts needed to run the system as a single unified GUI. Additionally, a new and more accurate material characterization algorithm was implemented to improve measurement quality.

### 4.3.2 System Description

The three-probe system, as the name implies, uses three WR-112 waveguides with 3D printed dielectric rod antennas to measure a material sample over a wide range of incident angles. Two of the probes, as shown in Fig. 4.9 and labeled $Tx$ and $Rx_1$, are locked in place.$Tx$ is the transmitting antenna. The $Rx_1$ antenna is used to measure the transmitted component of the applied wave. The $Rx_2$ antenna, however, is free to rotate. This antenna is mounted to a rotary table to enable automatic accurate movement. The $Rx_2$ antenna can then follow the rotation of the material sample

over incident angle, and it will receive the reflected component of the applied wave. This permits the user to apply a two-parameter Nicolson-Ross-Weir method to the measured data, and extract the material parameters more accurately.
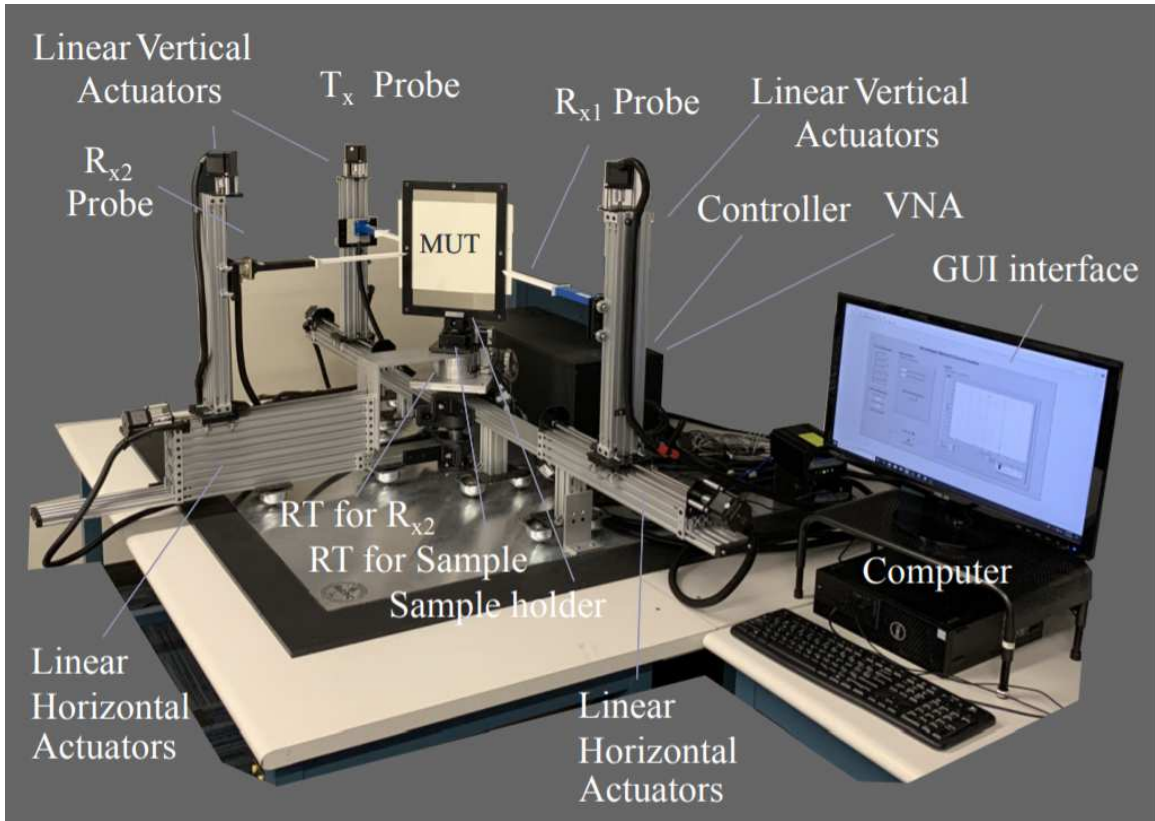


Figure 4.9: Anisotropic scanner full system setup

The RF scanner utilizes six aluminum rails acting as linear actuators that can be used to move the trolleys mounted on them. Each linear actuator has a stepper motor, which is used to position the trolleys and allows the entire measurement process to be automated. Three of the rails are mounted horizontally around a single axis where the material under test is also mounted on a rotary table. Each of the three horizontal rails has a trolley mounted on it upon which is mounted another linear actuator. These three rails can position their trolleys vertically and upon each trolley

a probe is secured. This allows each of the three probes to move both up/down and nearer/farther from the sample independently.

All of the stepper motors that drive the linear actuators are controlled by two TinyG CNC controller boards. They have an accuracy of 0.091mm [2]. These are controlled by sending commands to the TinyG USB port that interfaces with the controlling computer. Additionally, limit switches are mounted on all of the linear actuators at known positions to allow the system to automatically home itself and prevent damage to the system.

The VNA used for this system is a Copper Mountain Planar 804/1 with two ports. Because the VNA has only two ports, while there are three probes required to take the transmission and reflection measurements when not at broadside, an RF switch was used to switch the second port between the probes receiving the transmitted and reflected waves. To communicate with this switch an Arduino Uno was used to control a solid state relay that delivered the 24 V required to operate the switching action.

This setup allows a sample to be centered between all three probes. As the sample rotates off broadside from the transmitter, the reflected waveform will no longer reflect directly back. This is where the $S_{11}$ receiver becomes useful, it rotates in tandem with the sample to capture the reflected wave. Therefore, both the transmitted and reflected portions of the waveform are sampled, even at oblique incidence.

Each probe is a dielectric rod antenna designed for 7.5 GHz (WR112). These antennas were useful for this application due to their narrow beamwidth (10°) and small far-field range (2 inches), both of which contributed to a reduction in the size

of the entire testing apparatus. The antennas must be at least their far-field distance away from the sample to take an accurate measurement.

An important consideration in this system is the size of the sample under test. If the area illuminated by the test beam approaches or crosses the edge of the sample, then direct transmission and edge diffraction will occur, both of which will cause inaccurate measurements. Because of this, the sample's height and width should be at least 1.5 times larger than the antenna beamwidth [58]. The sample thickness must also be small with respect to the wavelength ($l << \lambda_r/2$).

### 4.3.3   Modes of Operation

The system has three primary modes of operation: broadside material characterization, oblique incident angle material characterization, and S-parameter measurements for when the extracted material parameters are unnecessary. For each mode an exact procedure must be followed before measurements can be taken. First, the system must be homed so that accidental moves out of the range of the linear actuators (which can severely damage the system) can be avoided. The homing procedure is fairly simple, as the TinyG control boards have a built-in functionality for the process. Limit switches are installed on all linear actuators, and their positions are defined programatically on the control boards. The homing procedure watches each of the probes that will be used in the measurement, $Tx_1$ and $Rx_1$ for broadside or all three for an oblique angle measurement, move until the trolley impacts the limit switch. This occurs for all horizontal and vertical actuators. After this is accomplished, the

system acknowledges that the probes are in a pre-defined position and ready to be moved.

Following this, the system must be calibrated. An automated calibration procedure was developed for the system. The calibration procedure changes slightly depending on if the scanner is taking broadside or angular sweep measurements, with Transmission-Reflection-Line (TRL) being used for broadside and Transmission-Reflection for the angular sweep.

For a broadside TRL calibration, three steps are required, although most of the positioning is handled by the control software. The first step is to take a Transmission or Thru measurement. When the calibration procedure is started, the probes will move automatically to the user-specified position for measurements. This is followed by taking a measurement with no reflect standard. Next, a line measurement is taken. To create the effect of a line delay in free-space, each of the probes retracts by one eighth of a wavelength, creating a separation of $\lambda/4$. This delay is used by the VNA to calibrate for phase errors. Finally, a reflection measurement is taken. This is accomplished by returning the probes to their original location, after which the user places a slab of copper-clad dielectric (which must be the same thickness as the MUT) into the sample holder. This will reflect the impinging wave, and will provide all of the requisite information to apply a TRL calibration.

To perform a calibration for an oblique incidence angle measurement, the procedure is somewhat more complicated, however it is no more difficult for the user. The basic idea of the calibration is to take a reflection measurement at every angle that will then be measured for the MUT. First, the sample holder must be empty

and a Thru measurement will be taken for the $Tx_1$ and $Rx_1$ probes. After this, the system will prompt the user to input a reflect standard. When the reflect standard is mounted in the sample holder, the system will automatically move to the first angle that will be measured. The sample will rotate, and the mobile probe $(Rx_2)$ will follow that rotation to be directed at the angle where the majority of the energy will be reflected. The system cycles through all of the positions to be measured, taking a reflect measurement and then saving a VNA state. Each of these states are assigned a number that is used by the system during the measurement process later.

Once this calibration is applied, the system allows the user to take a measurement. For a broadside measurement, this is extremely simple and fast. The user simply prompts the system for a measurement, and, in a similar process to that described in the discussion of the mmWave scanner, the S-parameters are saved and a modified NRW script is applied to them.

For the oblique incidence angle measurements, the process once again takes more time but is also quite user-friendly. The system prompts the user to input the material sample, and then moves to the starting angle. Following this, a process will ensue where the system recalls a saved calibration state from the VNA, then saves the calibrated S-parameters to a CSV file, passes those S-Parameters to a MATLAB script that applies the material characterization algorithm, then stores the material parameters. This is repeated for every angle of interest. Once this is completed, the angular data for a single frequency (7.5 GHz as that is the operating frequency for the rod antennas) is displayed for the user.

Finally, a simple measurement of the S-Parameters is also possible. For this, the user employs the manual positioning feature to position the probes as needed, and saves the S-Parameters directly from the VNA.

### 4.3.4   GUI Development

The creation of an easily accessible user interface was a key goal in the author's work on this scanner. This interface has several key features which will be discussed: VNA configuration, manual mechanical control, measurement configuration, system status visualization, calibration and homing, data visualization, and data saving utilities. This user interface is pictured below in Fig. 4.10
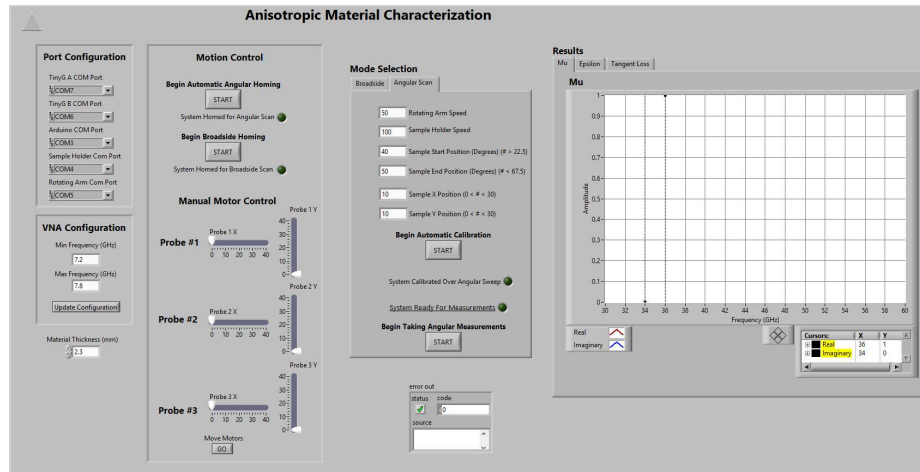


Figure 4.10: Anisotropic scanner LabView GUI

While much of this functionality had existed in the past, it was part of a massive number of Vi's and sub Vi's that had to be operated independently. Additionally, when running scans the only option for the user was to follow a strict path that included homing, calibration, and measurement. This forced the user to arduously

recalibrate for every measurement that needed to be taken, even if they were sequential and utilized the same measurement setup. This had to be rectified during the development of this GUI.

When the code is initialized, it first configures the VNA and the socket connections required for operation. These sockets can be customized within the user interface as seen in the upper left hand corner of the GUI in Fig. 4.10. The initialization code is shown below in Fig. 4.11:
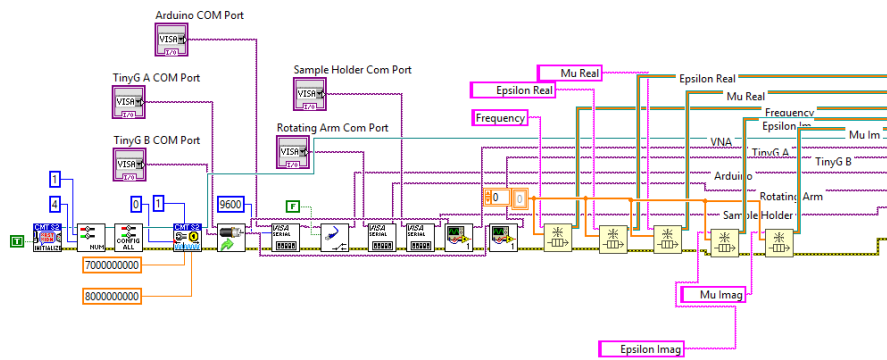


Figure 4.11: Anisotropic scanner initialization code

As with all of the other user interfaces, a way to control and reconfigure the VNA is included in this GUI. This allows the user to specify the frequency range of interest as well as the number of points to measure.

Before the hardware is allowed to operate, a homing procedure must be performed. This involves starting the homing procedure for whichever measurement mode is required: broadside or anisotropic. Once started, the system will move each linear

actuator towards its start point where a limit switch is mounted. Once the limit switch is activated the system will be "homed," and will know its reference location. After reaching the reference location, the system will move back to the specified measurement locations. Homing is required before calibration can be performed, to reduce the risk of a collision. This homing procedure is shown below in Fig. 4.12:
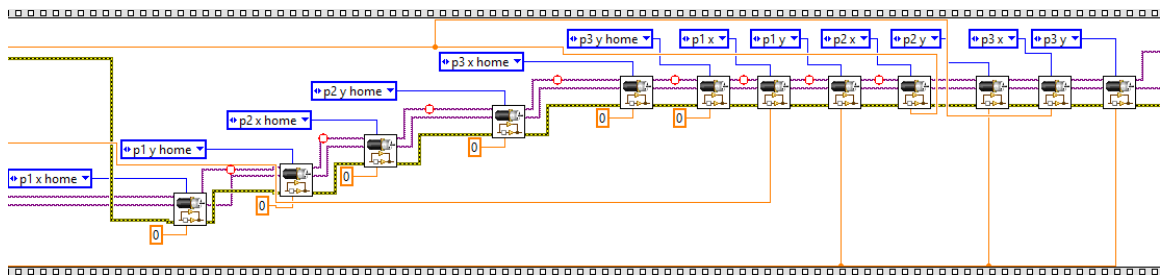


Figure 4.12: Anisotropic scanner homing procedure

The interface also allows for manual positioning of all of the linear actuators as shown in Fig. 4.13. This permits for manual testing to be done, as well as a quality of life improvement that removes the need to use a socket connection to communicate directly with the control board.
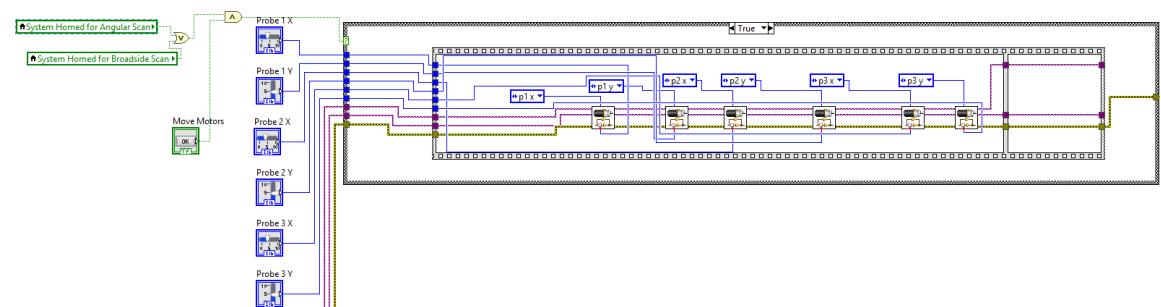


Figure 4.13: Anisotropic scanner reposition motors

Once a measurement is ready to be taken, the user must input the thickness of the measured material for the NRW script to use. As previously discussed, this is a vital parameter for accurate results to be obtained.

The interface also informs the user of the current status of the system. Lights will indicate when the system is connected to the VNA, when the system is homed, and when the system is calibrated and ready for a measurement to be taken.

The GUI allows for automatic calibration procedures to be performed and includes prompts to the user that guide them through the process. The first calibration procedure, for broadside measurements, is very simple and requires the user to merely input and remove a reflect standard from the sample holder. Other than this, the system handles all movements and measurements required to implement a TRL calibration.

For an angular calibration, the code is more interesting. The system first takes a through measurement between the two broadside ports, then moves to the starting position and prompts the user to input the reflect standard. It then moves to each position to take and store a calibration file. This is shown below in Fig. 4.14.
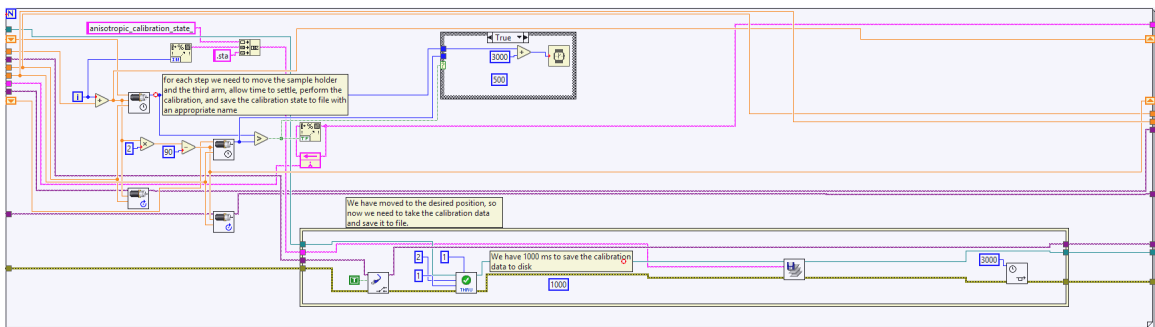


Figure 4.14: Anisotropic scanner angular scan calibration

Once the system is prepared, a measurement can be taken. The general procedure is similar to the angular calibration, in that the system is moving to the determined measurement locations, loading cal files, taking measurements, and saving them. This procedure is also shown below in Fig. 4.15:
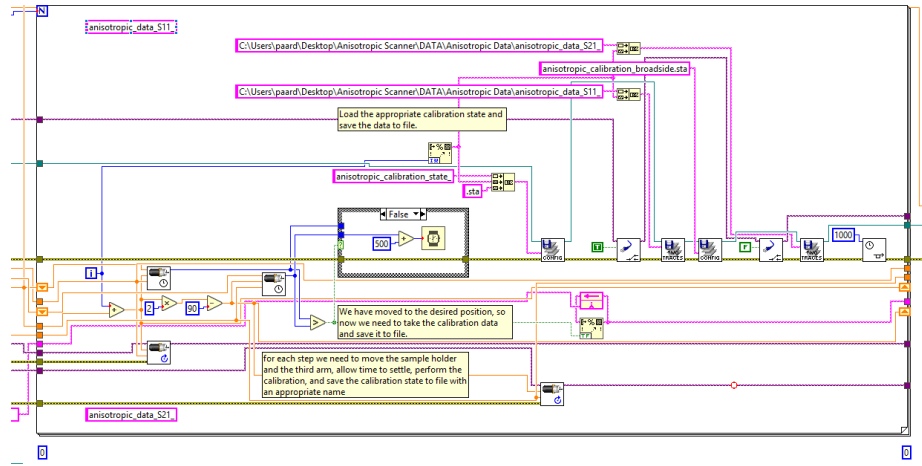


Figure 4.15: Anisotropic scanner angular measurements

Once a measurement is taken, plots of the values measured are shown to the user. They are interactive,adjustable, and have dynamic markers to show values at a point of interest. The user can the easily save the data as a CSV file with a user-defined name and location.

### 4.3.5  Results

The results shown below are measurements of two dielectric slabs over a range of incident angles from 30 - 50 degrees. A summary of the results are shown in Table 4.2, where $\sigma$ represents the standard deviation of the measurements, and plots of the measurements are shown below that. The mean is calculated over all incident angles

at a frequency of 7.5 GHz. All plots shown below are also at 7.5 GHz. We witnessed favorable matching for both permittivities, although the results veered away from the expected value at larger incident angles. This is to be expected, because as the sample rotates, the beam of the transmitting antenna approaches the edge of the sample, causing diffraction effects that can negatively impact the results.

Table 4.2: Measured results anisotropic scanner

| Material | Expected $\epsilon$ | Mean Measured $\epsilon$ | $\sigma$ Real | $\sigma$ Imag |
|----------|---------------------|--------------------------|---------------|---------------|
| RT5880   | 2.20 - 0.000198j    | 2.2749 - 0.1107j         | 0.1139        | 0.0447        |
| RO4350   | 3.66 - 0.0113j      | 3.6572 - 0.5014j         | 0.1655        | 0.4195        |
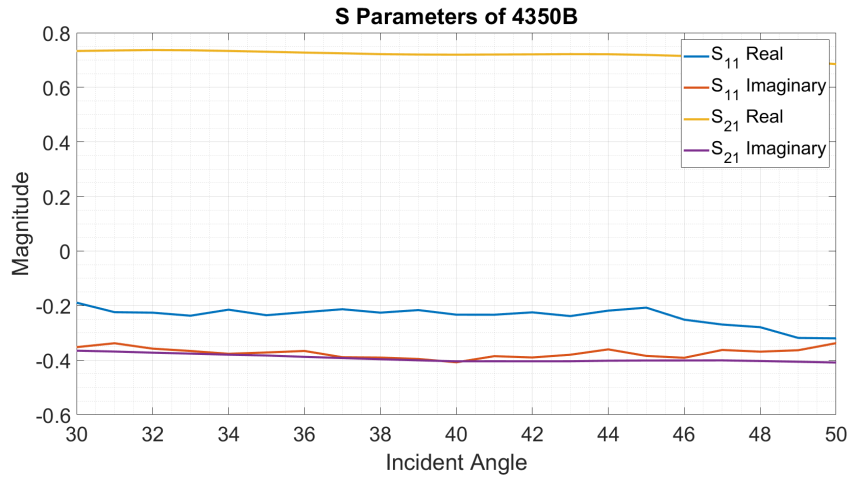


Figure 4.16: Measured RO4350 S-parameters
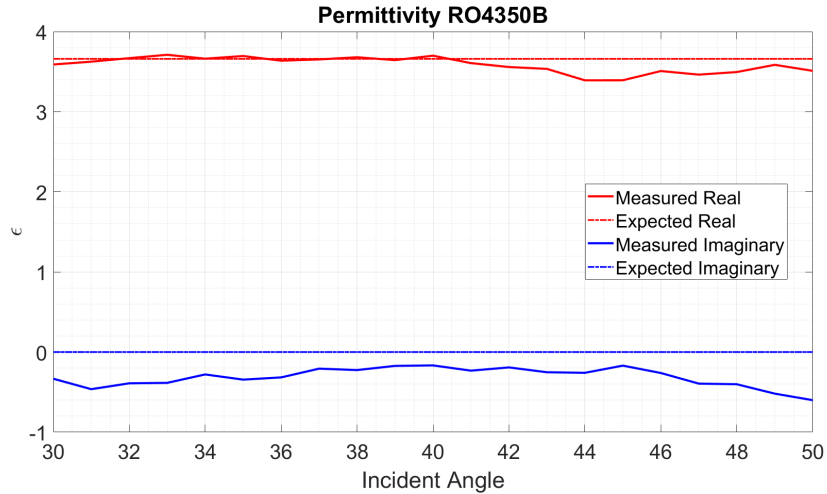
Figure 4.17: Measured RO4350 permittivity

The edge effects generate significant phase error, especially as the sample rotates to more severe angles of incidence. These phase errors are visible in the calculations of the permittivity in Fig. 4.17 above and are even more pronounced in the measurements of the imaginary component of the permeability below in Fig. 4.18.
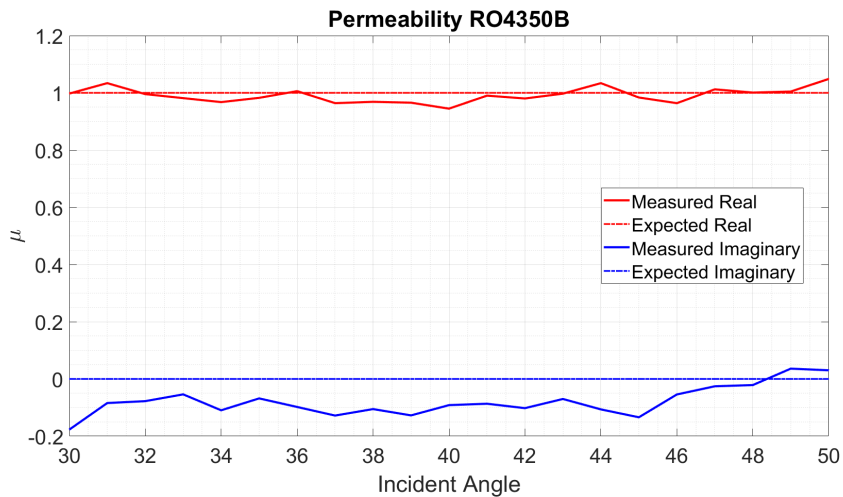


Figure 4.18: Measured RO4350 permeability

The reflected $S_{11}$ component is also normally much smaller in magnitude than the $S_{21}$ measurement, which leaves it even more susceptible to interference from diffracted fields. This is also reflected in Table 4.2 in the standard deviation $\sigma$ of the imaginary component, where great variance is seen over a measurement.
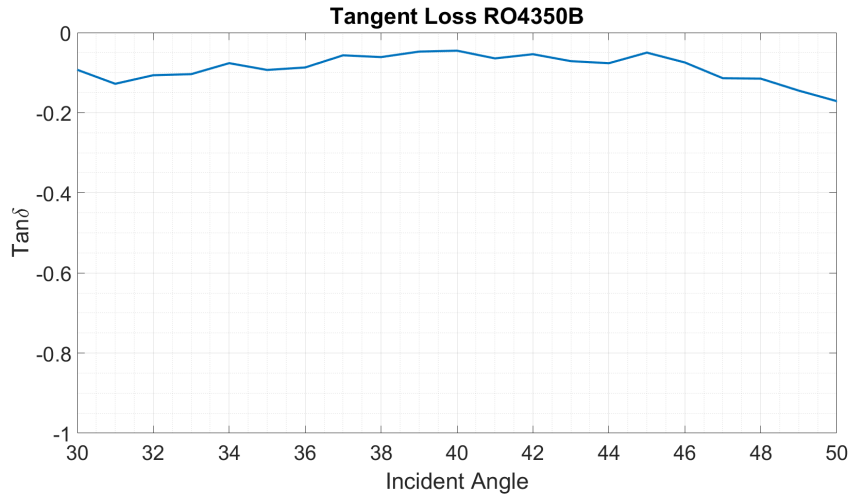


Figure 4.19: Measured RO4350 tangent loss
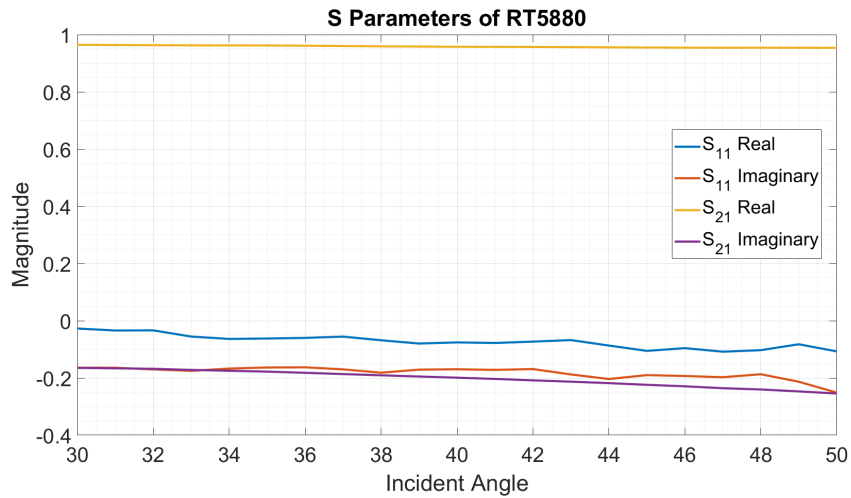


Figure 4.20: Measured RO5880 S-parameters
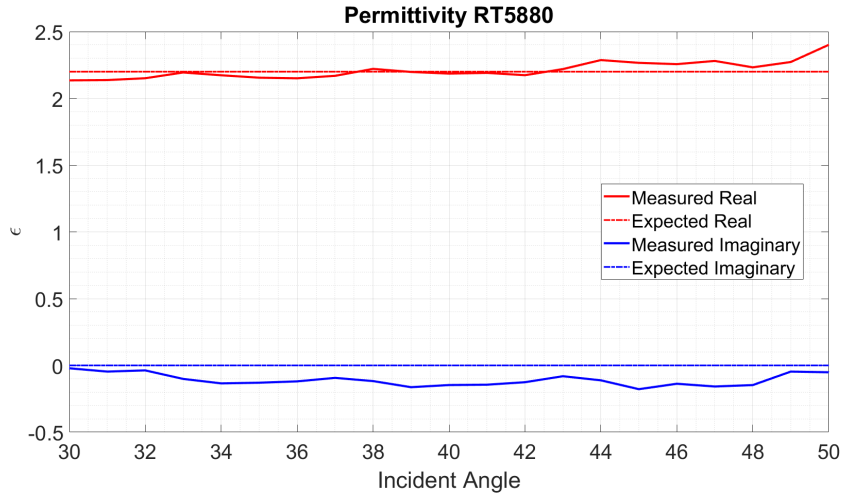
Figure 4.21: Measured RO5880 permittivity

The measured results of Rogers RT5880 match more closely with the expected values, although there is still variance seen in the imaginary components.
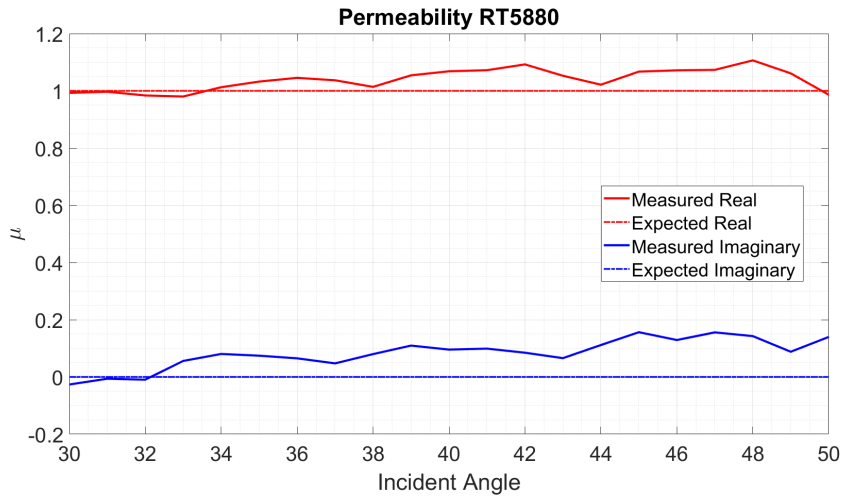


Figure 4.22: Measured RO5880 permeability
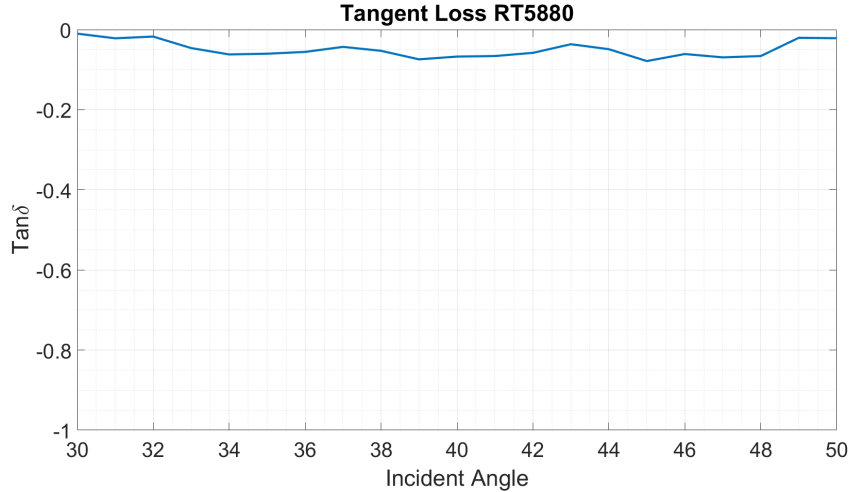
Figure 4.23: Measured RO5880 tangent loss

These results show improvement over the outcome previously measured with this machine. The main driver of this improvement is the implementation of a two-parameter algorithm, the reduction in phase errors, and experimentation with antenna positioning.

The two-parameter NRW algorithm that was implemented using the method found in [58] improves the results at more extreme angles of incidence, but is also very susceptible to phase errors. These errors were so unfavorable, that for the previous work on this system a single parameter (just using $S_{21}$) produced better results. However, through lots of experimentation and efforts to reduce the phase errors present, acceptable results were produced with the new algorithm.

To reduce these errors, several steps were taken, primarily removing the mounting frame used for samples and experimenting with time-gating settings. The removal of the mounting frame presented its own difficulties, however, as the sample was now increasingly prone to bending horizontally. Any sort of flex in the sample introduces

errors of its own, as this introduces variation into the distance of the probes to the sample and thus also produces phase error. This was mitigated by using thicker samples that were more structurally sound as well as setting the sample holder rotation rate to a minimum.

As discussed in [10], the antennas that are currently mounted on the system have disadvantages. This is mainly caused by two factors, the spherical nature of the wave produced by the antenna and the width of the beam. To get accurate results, the wave impinging on the sample must be close to planar and illuminating only the sample. However, for the dielectric rod antennas that are used presently, these two criteria present a dilemma wherein moving the antenna far enough away to have a planar phase front causes the beamwidth to become too large.

The best results were obtained by moving the antennas to their highest point possible at the range suggested by [10]. This, in combination with the removal of the metal frame, which appears to be a source of much of the diffracted fields at larger incident angles, and a narrow time gating band produce the best results. However, if a Gaussian focused beam antenna could be used for the system, the author believes even more accurate results are possible.

## 4.4 Summary

This chapter summarizes the work done by the author on the automation of two free-space material characterization systems. The first system discussed is the mmWave

RF scanner. The system operates at 75-110 GHz and provides multi-mode functionality that allows for antenna measurements in addition to material characterization. The system hardware and different modes of operation are presented first. This is followed by a description of the user interface. Finally, measured results from three dielectrics are presented. The other system that is detailed is the three-probe material characterization scanner. This system, initially designed by Alex Stringer and Joel Love, was upgraded to include a new user interface that should streamline operation. The hardware and operating modes are presented, followed by a discussion of the creation of a GUI to control the system. The operation of the control software is also detailed along with descriptions of the different features present. The calibration procedure for both the broadside and angular measurement tests is detailed and the software that drives this calibration is presented. This includes a discussion of the interaction between the software, the control boards, and the VNA. The section concludes with the presentation of material characterization tests for validation of system efficacy. No frequency selective surfaces or anisotropic materials could be fabricated by the PAARD to test with this scanner before operation of the lab ceased. However, two commonly known dielectrics were used and showed improved consistency over incident angle.

# Chapter 5

# Epilogue

Three material characterization systems were automated and tested, with improvements made to their parameter extraction algorithms and overall usability. For each system, control software was created to allow for rapid calibration, testing, and data visualization with a focus on accessibility. This control software is explored in detail for all systems and shows the general program flow as well as describing the different capabilities available to the user. The hardware design for each system is also outlined along with descriptions of the different modes of operation the machine can support. Each system was successfully automated, and this functionality was displayed with measurements of a variety of dielectric materials. Possible sources of error in measurements taken were determined, and their effects quantified through the use of the electromagnetic simulation software HFSS. This error analysis should prove useful for future measurements taken with these systems, as should the work done on potentially fabricating additional waveguide segments. Through the implementation of these user interfaces this work should present an ideal stepping stone for future studies in the characterization of RF materials.

## 5.1 Conclusion

The goal of this thesis was to automate three material characterization systems present in the Advanced Radar Research Center to allow for easier use and to reduce measurement time. For each system, a centralized user interface was developed that unified the procedures of calibration, measurement taking, and data post-processing into a single accessible form.

Each of the three systems present unique capabilities and operational frequency ranges that allow for a wide variety of dielectrics to be tested. The three-probe scanner offers a flexible setup that can measure smoothly over a wide range of incident angles which is invaluable for characterizing anisotropic materials. The mmWave scanner, which was already programmed to perform as an antenna measurement system, was augmented to provide broadside and angular material measurements at W-band frequencies. The guided-wave system presents rapid and accurate testing of isotropic materials, with work done to expand this functionality to anisotropic materials in the future.

For each system the creation of a user-friendly interface was the primary objective, and to accomplish this LabView was chosen for its ease of communication with the VNAs and control boards utilized in the scanners. These user interfaces allow for the user to open only a single window and do not require a high level of experience with the machine to operate. Each GUI integrates the common tasks performed during a measurement into a single place, which drastically cuts down on the time involved.

This includes prompting the user and guiding them through the calibration procedure for each system, taking measurements automatically, processing that data with MATLAB, and visualizing it for the user in a way that allows for easy exportation.

A variety of methods to improve the systems were explored. A rectangular to square waveguide transition was simulated and fabricated, in an attempt to add anisotropic material measurement capabilities to the guided-wave system. While this was not ultimately successful, the foundation for fabrication of these structures in the future is present. The material extraction algorithms were also improved upon, with a new two-parameter algorithm being implemented for the three-probe scanner and normalization of measured permeability explored to counteract measurement errors.

Measurements of a varied set of materials were taken for each system to verify their functionality as well as that of the user interfaces. This list includes traditional dielectrics such as Rogers 4350B and RT5880, 3D printed dielectrics, and non-traditional materials like concrete. Although not every measurement that was taken with these systems is presented in this document, it is encouraging that so many different applications for these systems have been found in the time they have been operational. Where the measured values did not align with expectations, simulations of possible error sources were performed. These simulated results helped to determine that, for example, using the guided wave system, gaps between the sample, sample holder, and waveguide ports were likely responsible for the shift seen in some measured results. The measurements taken verify the functionality of the user interfaces developed for this system as tools to expedite measurements.

## 5.2   Future Work

In the next stage of this work, the ideal steps would be to develop anisotropic materials for testing as well as some improvements to the current hardware and software. The systems are now ready for more thorough testing from a variety of users. In the future a primary goal should be the development of more materials to characterize.

In terms of changes to the hardware, the three-probe system presents some room for improvements to be made. The three-probe system uses dielectric rods that, as explored by Joel Love in [10], leave much to be desired. Those issues, including the beamwidth and production of a planar wavefront, limit the accuracy of the system. Introduction of new Gaussian focused beam antennas could greatly improve accuracy. Additionally, the introduction of more limit switches on some of the mounting rails would be useful. This would allow for completely safe operation, as currently not all directions of movement are terminated with a limit switch. Limit switches on the rotary table that controls the third moving arm would also allow for complete automation and would enhance positional accuracy.

The software can also be updated and improved in the future. There are some minor bugs related to timeouts and lag on button response that could be investigated and solved. More features could be added as needed for future users. Manual control of the sample holder for the three-probe system would be advantageous.

# Bibliography

[1] D. M. Pozar, *Microwave Engineering Fourth Edition*. 2005.

[2] A. Stringer, "A Novel Method for the Characterization of Anisotropic Materials," Master's thesis, University of Oklahoma, 2018.

[3] S. Roberts and A. Von Hippel, "A New Method for Measuring Dielectric Constant and Loss in the Range of Centimeter Waves," *Journal of Applied Physics*, vol. 17, pp. 610–616, Jul 1946.

[4] M. J. Havrilla and D. P. Nyquist, "Electromagnetic characterization of layered materials via direct and de-embed methods," *IEEE Transactions on Instrumentation and Measurement*, vol. 55, pp. 158–163, Feb 2006.

[5] J. Musil, F. Zacek, A. Burger, and J. K. lovsky, "New microwave system to determine the complex permittivity of small dielectric and semiconducting samples," in *1974 4th European Microwave Conference*, pp. 66–70, Sep. 1974.

[6] D. K. Ghodgaonkar, V. V. Varadan, and V. K. Varadan, "A free-space method for measurement of dielectric constants and loss tangents at microwave frequencies," *IEEE Transactions on Instrumentation and Measurement*, vol. 38, pp. 789–793, Jun 1989.

[7] C. A. Balanis, *Advanced engineering electromagnetics*. John Wiley & Sons, second ed., 2012.

[8] A. G. Knisely, M. W. Hyde, M. J. Havrilla, and P. J. Collins, "Uniaxial anisotropic material measurement using a single port waveguide probe," in *AMTA 2016 Proceedings*, (Austin, TX, USA), pp. 1–6, IEEE, Oct 2016.

[9] Z. Qamar, N. Aboserwal, and J. L. Salazar-Cerreno, "An accurate method for designing, characterizing, and testing a multi-layer radome for mm-wave applications," *IEEE Access*, vol. 8, pp. 23041–23053, 2020.

[10] J. Love, "Automated Calibration of an Anisotropic Materials Characterization Instrument," Master's thesis, University of Oklahoma, 2019.

[11] T. Zwick, A. Chandrasekhar, C. W. Baks, U. R. Pfeiffer, S. Brebels, and B. P. Gaucher, "Determination of the complex permittivity of packaging materials at millimeter-wave frequencies," *IEEE Transactions on Microwave Theory and Techniques*, vol. 54, pp. 1001–1010, March 2006.

[12] R. A. Fenner, E. J. Rothwell, and L. L. Frasch, "A comprehensive analysis of free-space and guided-wave techniques for extracting the permeability and permittivity of materials using reflection-only measurements," *Radio Science*, vol. 47, Feb 2012.

[13] M. Kaniecki, E. Saenz, L. Rolo, R. Appleby, and O. Breinbjerg, "Scattering-parameter extraction and calibration techniques for RF free-space material characterization," in *8th European Conference on Antennas and Propagation, EuCAP 2014*, pp. 1093–1097, IEEE, Apr 2014.

[14] Baker-Jarvis and James, "Transmission/reflection and short-circuit line permittivity measurements," tech. rep., NIST, Washington, DC, 1990.

[15] D. G. Watters and M. E. Brodwin, "Automatic material characterization at microwave frequencies," *IEEE Transactions on Instrumentation and Measurement*, vol. 37, pp. 280–284, June 1988.

[16] J.-Y. Chung, *Broadband Characterization Techniques for RF Materials and Engineered Composites.* PhD thesis, Ohio State University, 2010.

[17] K. Saeed, R. D. Pollard, and I. C. Hunter, "Substrate integrated waveguide cavity resonators for complex permittivity characterization of materials," *IEEE Transactions on Microwave Theory and Techniques*, vol. 56, pp. 2340–2347, Oct 2008.

[18] F. Costa, M. Borgese, M. Degiorgi, and A. Monorchio, "Electromagnetic Characterisation of Materials by Using Transmission/Reflection (T/R) Devices," *Electronics*, vol. 6, p. 95, Nov 2017.

[19] V. V. Varadan and R. Ro, "Unique retrieval of complex permittivity and permeability of dispersive materials from reflection and transmitted fields by enforcing causality," *IEEE Transactions on Microwave Theory and Techniques*, vol. 55, pp. 2224–2230, Oct 2007.

[20] J. L. Vedral, *Analysis, Characterization and Application of Microwave Metamaterials.* PhD thesis, University of Colorado at Colorado Springs, 2016.

[21] R. W. Ziolkowski, "Design, fabrication, and testing of double negative metamaterials," *IEEE Transactions on Antennas and Propagation*, vol. 51, pp. 1516–1529, Jul 2003.

[22] S. K. Ghosh, S. K. Parui, and A. Chatterjee, "Development of novel engineered metamaterial: Structure, extraction of various parameters and applications," in *2017 1st International Conference on Electronics, Materials Engineering and Nano-Technology, IEMENTech 2017*, pp. 1–6, IEEE, Apr 2017.

[23] V. G. Veselago, "THE ELECTRODYNAMICS OF SUBSTANCES WITH SIMULTANEOUSLY NEGATIVE VALUES OF $\epsilon$ AND ," *Soviet Physics Uspekhi*, vol. 10, pp. 509–514, Apr 1968.

[24] C. E. Kintner, *Free-Space Measurements of Dielectrics and Three-Dimensional Periodic Metamaterials.* PhD thesis, University of Arkansas, 2017.

[25] A. Solovey, M. Wasson, and R. Mittra, "Free space transmission loss measurement of magneto-dielectric materials: Solution uniqueness and measurement tolerance tradeoffs," in *The 40th European Microwave Conference*, (Paris, France), IEEE, 2010.

[26] A. G. Knisely and M. J. Havrilla, "Material characterization de-embedding for rectangular to square waveguide," in *Antennas and Propagation (EuCAP), 2015 9th European Conference on.*, (Lisbon, Portugal), pp. 1–5, IEEE, 2015.

[27] D. R. Smith, S. Schultz, P. Markoš, and C. M. Soukoulis, "Determination of effective permittivity and permeability of metamaterials from reflection and transmission coefficients," *Physical Review B*, vol. 65, no. 19, p. 5, 2002.

[28] A. N. Plastikov, "About two approaches to automation of a process of calculating metamaterial parameters according to the scattering-parameter extraction method using modern full-wave simulators," in *2017 Progress In Electromagnetics Research Symposium - Spring (PIERS)*, pp. 3763–3767, IEEE, May 2017.

[29] X. Chen, B.-I. Wu, J. A. Kong, and T. M. Grzegorczyk, "Retrieval of the effective constitutive parameters of bianisotropic metamaterials," *Physical Review E*, vol. 71, p. 46610, Apr 2005.

[30] B. Crowgey, J. Tang, O. Tuncer, L. Kempel, E. Rothwell, and B. Shanker, "Measurement of anisotropic material properties for antenna applications," in *2012 Loughborough Antennas & Propagation Conference (LAPC)*, pp. 1–4, IEEE, Nov 2012.

[31] M. Y. Koledintseva, J. L. Drewniak, and S. Hinaga, "Effect of anisotropy on extracted dielectric properties of pcb laminate dielectrics," in *2011 IEEE International Symposium on Electromagnetic Compatibility*, pp. 514–517, Aug 2011.

[32] D. Cohen and R. Shavit, "Bi-anisotropic Metamaterials Effective Constitutive Parameters Extraction Using Oblique Incidence S-Parameters Method," *IEEE Transactions on Antennas and Propagation*, vol. 63, pp. 2071–2078, May 2015.

[33] H.-C. Yin, Z.-M. Chao, and Y.-P. Xu, "A new free-space method for measurement of electromagnetic parameters of biaxial materials at microwave frequencies," *Microwave and Optical Technology Letters*, vol. 46, pp. 72–78, Jul 2005.

[34] A. G. Knisely, *Biaxial Anisotropic Material Development and Characterization using Rectangular to Square Waveguide*. PhD thesis, AIR FORCE INSTITUTE OF TECHNOLOGY, 2015.

[35] G. F. Engen and C. A. Hoer, "Thru-Reflect-Line: An Improved Technique for Calibrating the Dual Six-Port Automatic Network Analyzer," *IEEE Transactions on Microwave Theory and Techniques*, vol. 27, pp. 987–993, Dec 1979.

[36] H. J. Eul and B. Schiek, "A Generalized Theory and New Calibration Procedures for Network Analyzer Self-Calibration," *IEEE Transactions on Microwave Theory and Techniques*, vol. 39, pp. 724–731, Apr 1991.

[37] U. Stumper, "Uncertainties of VNA S-Parameter Measurements Applying the TAN Self-Calibration Method," *IEEE Transactions on Instrumentation and Measurement*, vol. 56, pp. 597–600, Apr 2007.

[38] U. Stumper and T. Schrader, "Calibration method for vector network analyzers using one or two known reflection standards," *IEEE Transactions on Instrumentation and Measurement*, vol. 63, pp. 1648–1655, Jun 2014.

[39] A. M. Nicolson and G. F. Ross, "Measurement of the Intrinsic Properties Of Materials by Time-Domain Techniques," *IEEE Transactions on Instrumentation and Measurement*, vol. 19, pp. 377–382, Nov 1970.

[40] W. B. Weir, "Automatic Measurement of Complex Dielectric Constant and Permeability at Microwave Frequencies," *Proceedings of the IEEE*, vol. 62, no. 1, pp. 33–36, 1974.

[41] D. R. Smith, D. C. Vier, T. Koschny, and C. M. Soukoulis, "Electromagnetic parameter retrieval from inhomogeneous metamaterials," *Physical Review E - Statistical, Nonlinear, and Soft Matter Physics*, vol. 71, p. 11, Mar 2005.

[42] O. Luukkonen, S. I. Maslovski, and S. A. Tretyakov, "A stepwise Nicolson–Ross–Weir-based material parameter extraction method," *IEEE Antennas and Wireless Propagation Letters*, vol. 10, pp. 1295–1298, 2011.

[43] S. Kim, D. Novotny, J. Gordon, and J. Guerrieri, "A differential form of the Kramers-Kronig relation for determining a Lorentz-type of refractive index," in *IEEE Antennas and Propagation Society, AP-S International Symposium (Digest)*, vol. 2015-Octob, pp. 1174–1175, IEEE, Jul 2015.

[44] I. B. Brezeanu, P. A. Paraschivoiu, R. Negroiu, and L. A. Chiva, "Applications of Kramers-Kronig Relations," in *2017 IEEE 23rd International Symposium for Design and Technology in Electronic Packaging (SIITME)*, pp. 82–85, IEEE, Oct 2017.

[45] J. J. Barroso and U. C. Hasar, "Comments on "A Unique Extraction of Metamaterial Parameters Based on Kramers-Kronig Relationship"," *IEEE Transactions on Microwave Theory and Techniques*, vol. 60, pp. 1743–1744, Jun 2012.

[46] J. J. Barroso and U. C. Hasar, "Constitutive Parameters of a Metamaterial Slab Retrieved by the Phase Unwrapping Method," *Journal of Infrared, Millimeter, and Terahertz Waves*, vol. 33, pp. 237–244, Feb 2012.

[47] A. Elhawil, G. Koers, L. Zhang, J. Stiens, and R. Vounckx, "Reliable method for material characterisation using quasi-optical free-space measurement in W-band," *IET Science, Measurement & Technology*, vol. 3, pp. 39–50, Jan 2009.

[48] H. Esteban, J. M. Catala, S. Cogollos, and V. E. Boria, "Characterization of complex dielectric properties of materials using a hybrid iterative method," in *IEEE Antennas and Propagation Society International Symposium: Wireless*

*Technologies and Information Networks, APS 1999 - Held in conjunction with USNC/URSI National Radio Science Meeting*, vol. 10, pp. 186–188, May 2000.

[49] R. A. Fenner and S. Keilson, "Free space material characterization using genetic algorithms," in *2014 16th International Symposium on Antenna Technology and Applied Electromagnetics (ANTEM)*, pp. 1–2, IEEE, Jul 2014.

[50] A. Deutsch, T. . Winkel, G. V. Kopcsay, C. W. Surovic, B. J. Rubin, G. A. Katopis, B. J. Chamberlin, and R. S. Krabbenhoft, "Extraction of /spl epsiv//sub r/(f) and tan/spl delta/(f) for printed circuit board insulators up to 30 ghz using the short-pulse propagation technique," *IEEE Transactions on Advanced Packaging*, vol. 28, pp. 4–12, Feb 2005.

[51] J. M. Grimm, D. P. Nyquist, M. Thorland, and D. Infante, "Broadband material characterization using microstrip/stripline field applicator," in *IEEE Antennas and Propagation Society International Symposium 1992 Digest*, pp. 1202–1205 vol.2, June 1992.

[52] N. Mahjabeen, H. McIntyre, Y. Goel, S. P. Gowri, and R. Henderson, "Dielectric characterization of stacked packaging substrates using a coaxial transmission line technique," in *2019 IEEE Texas Symposium on Wireless and Microwave Circuits and Systems (WMCS)*, pp. 1–5, March 2019.

[53] Z. Abdurrasyid and A. Munir, "Characterization of thin slab artificial dielectric material using rectangular waveguide," in *2014 International Conference on Computer, Control, Informatics and Its Applications (IC3INA)*, pp. 141–144, Oct 2014.

[54] O. V. Tereshchenko, F. J. K. Buesink, and F. B. J. Leferink, "Measurement of complex permittivity of composite materials using waveguide method," in *10th International Symposium on Electromagnetic Compatibility*, pp. 52–56, Sep. 2011.

[55] A. B. Bhattacharyya, S. Tuli, and S. Kataria, "An automated nondestructive characterization system for pyroelectric materials," *IEEE Transactions on Instrumentation and Measurement*, vol. 43, pp. 30–33, Feb 1994.

[56] S. Wu, S. Guan, C. Li, L. Tsai, C. Kuo, M. Hsieh, and C. Su, "Dielectric constant and loss-tangent extraction using near-field technology and phase delay method," in *2018 IEEE International Symposium on Electromagnetic Compatibility and 2018 IEEE Asia-Pacific Symposium on Electromagnetic Compatibility (EMC/APEMC)*, pp. 683–686, May 2018.

[57] A. Rakov, M. Sobchenko, K. Dumchikov, V. Zhukov, and V. Ukhandeev, "Automatic system for characterization of high-frequency printed circuit board materials," in *2018 IEEE Conference of Russian Young Researchers in Electrical and Electronic Engineering (EIConRus)*, pp. 1692–1696, Jan 2018.

[58] J. W. Schultz, *Focused Beam Methods Measuring Microwave Materials in Free Space.* 2012.

[59] K. K. Joshi and R. D. Pollard, "Microstrip resonator technique for non-destructive moisture/permittivity measurement," in *1999 IEEE MTT-S International Microwave Symposium Digest (Cat. No.99CH36282)*, vol. 4, pp. 1863–1866 vol.4, June 1999.

[60] M. A. H. Ansari, A. K. Jha, and M. J. Akhtar, "Dual band microwave sensor for dielectric characterization of dispersive materials," in *2015 Asia-Pacific Microwave Conference (APMC)*, vol. 1, pp. 1–3, Dec 2015.

[61] W. Chen, K. G. McCarthy, and A. Mathewson, "Practical considerations for measurements of test structures for dielectric characterization," in *2009 IEEE International Conference on Microelectronic Test Structures*, pp. 221–225, March 2009.

[62] S. LeFrancois, D. Pasquet, and G. Maze-Merceur, "A new model for microwave characterization of composite materials in guided-wave medium," *IEEE Transactions on Microwave Theory and Techniques*, vol. 44, pp. 1557–1562, Sep. 1996.

[63] M. N. Afsar, Yong Wang, and A. N. Andreucci, "Accurate measurement of complex permittivity of liquids using the in-waveguide technique," in *Conference Digest Conference on Precision Electromagnetic Measurements*, pp. 6–7, June 2002.

[64] X. Wang, A. Díaz-Rubio, and S. Tretyakov, "Microwave and millimeter-wave characterization of conductive ink film in rectangular waveguide," in *2017 47th European Microwave Conference (EuMC)*, pp. 843–846, Oct 2017.

[65] J. A. R. Ball and B. Horsfield, "Resolving ambiguity in broadband waveguide permittivity measurements on moist materials," *IEEE Transactions on Instrumentation and Measurement*, vol. 47, pp. 390–392, April 1998.

[66] H. Ebara, T. Inoue, and O. Hashimoto, "Measurement method of complex permittivity and permeability for a powdered material using a waveguide in microwave band," *Science and Technology of Advanced Materials*, vol. 7, no. 1, pp. 77–83, 2006.

[67] A. Sharma and M. N. Afsar, "Microwave complex permeability and permittivity measurements of commercially available nano-ferrites," *IEEE Transactions on Magnetics*, vol. 47, pp. 308–312, Feb 2011.

[68] J. L. Jordan and G. E. Ponchak, "Rectangular waveguide resonator for gas permittivity measurement at X-band," in *2018 IEEE Topical Conference on Wireless Sensors and Sensor Networks (WiSNet)*, pp. 59–62, Jan 2018.

[69] H. E. Bussey and J. E. Gray, "Measurement and standardization of dielectric samples," *IRE Transactions on Instrumentation*, vol. I-11, pp. 162–165, Dec 1962.

[70] R. M. Redheffer, "The Measurement of Dielectric Constants," in *Technique of Microwave Measurements*, pp. 561–678, C.G Montgomery ed., McGraw-Hill, 1947.

[71] T. E. Talpey, "Optical methods for the measurement of complex dielectric and magnetic constants at centimeter and millimeter wavelengths," *Transactions of the IRE Professional Group on Microwave Theory and Techniques*, vol. 2, pp. 1–12, Sep. 1954.

[72] R. Hiatt, "A study of vhf absorbers and anechoic rooms," 1963.

[73] J. Obrzut, A. M. Hassan, and E. J. Garboczi, "Free Space Microwave Non Destructive Characterization of Composite Materials — NIST," in *NDT of Composites 2015*, vol. 2015, NIST, May 2015.

[74] Ó. García-Pérez, F. Tercero, and S. López-Ruiz, "Free-space W-band setup for the electrical characterization of materials and mm-wave components," tech. rep., 2017.

[75] D. Zaluški, A. Grbic, and S. Hrabar, "Analytical and experimental characterization of metasurfaces with normal polarizability," *Physical Review B*, vol. 93, p. 155156, Apr 2016.

[76] L. E. Rickard Petersson and G. S. Smith, "On the use of a Gaussian beam to isolate the edge scattering from a plate of finite size," *IEEE Transactions on Antennas and Propagation*, vol. 52, pp. 505–512, Feb 2004.

[77] R. J. Wylde, G. S. Bell, and A. Murk, "Sample size limitations for frequency-swept free-space material characterization," in *2012 37th International Conference on Infrared, Millimeter, and Terahertz Waves*, p. 1, IEEE, Sep 2012.

[78] C. A. Balanis, *Antenna Theory: Analysis and Design.* USA: Wiley-Interscience, 2005.

[79] Z. Szabó, G. H. Park, R. Hedge, and E. P. Li, "A unique extraction of metamaterial parameters based on Kramers-Kronig relationship," *IEEE Transactions on Microwave Theory and Techniques*, vol. 58, pp. 2646–2653, Oct 2010.

[80] U. C. Hasar, G. Buldu, Y. Kaya, and G. Ozturk, "Determination of effective constitutive parameters of inhomogeneous metamaterials with bianisotropy," *IEEE Transactions on Microwave Theory and Techniques*, vol. 66, pp. 3734–3744, Aug 2018.

[81] I. T. Rekanos, T. V. Yioultsis, and C. S. Hilas, "An inverse scattering approach based on the differential E-formulation," *IEEE Transactions on Geoscience and Remote Sensing*, vol. 42, pp. 1456–1461, Jul 2004.

[82] M. Yeary, G. Crain, A. Zahrai, C. D. Curtis, J. Meier, R. Kelley, I. R. Ivic, R. D. Palmer, R. J. Doviak, G. Zhang, and T. Yu, "Multichannel receiver design, instrumentation, and first results at the national weather radar testbed," *IEEE Transactions on Instrumentation and Measurement*, vol. 61, no. 7, pp. 2022–2033, 2012.

[83] R. Cooper and R. Carter, "High power rf transmission," in *in Proceedings of the CERN Accelerator School: Radio Frequency Engineering*, CERN 2005–03, Ed.J Miles, 2005.

[84] D. K. Rytting, "An analysis of vector measurement accuracy enhancement techniques," 1982.

[85] E. Rothwell, J. Frasch, S. Ellison, P. Chahal, and R. Ouedraogo, "Analysis of the nicolson-ross-weir method for characterizing the electromagnetic properties of engineered materials," *Progress In Electromagnetics Research*, vol. 157, pp. 31–47, 01 2016.

[86] A. N. Vicente, G. M. Dip, and C. Junqueira, "The step by step development of NRW method," in *2011 SBMO/IEEE MTT-S International Microwave and Optoelectronics Conference (IMOC 2011)*, pp. 738–742, IEEE, Oct 2011.

[87] S. Arslanagić, T. V. Hansen, N. A. Mortensen, A. H. Gregersen, O. Sigmund, R. W. Ziolkowski, and O. Breinbjerg, "A review of the scattering-parameter extraction method with clarification of ambiguity issues in relation to metamaterial homogenization," *IEEE Antennas and Propagation Magazine*, vol. 55, pp. 91–106, Apr 2013.

[88] C. M. Tech, "Coppermountaintech S2VNA and S4VNA SCPI Programming Manual," Feb N/A.

[89] D. McGraw, "The measurement of the dielectric constant of three different shapes of concrete blocks," 2016.

[90] J. Zechmeister and J. Lacik, "Complex relative permittivity measurement of selected 3d-printed materials up to 10 GHz," in *2019 Conference on Microwave Techniques (COMITE)*, pp. 1–4, 2019.

[91] M. Elsallal, J. Hood, I. Mcmichael, and T. Busbee, "3d printed material characterization for complex phased arrays and metamaterials," *Microwave Journal*, vol. 59, pp. 20–34, 10 2016.

[92] F. Labs, "Form 2 Technical Specifications," Feb N/A.

# Appendices

# .1  Waveguide NRW Code

```
 function[f,mu,ep] = NRW(file,d,a,Save,name)

%    d=(6.27)*1e-3;
%    a=(72.5)*1e-3;
%    filename = 'MatCharTest.xls';
%    directory = 'C:\Users\paard\Desktop\Toms Labview';

filename = name;
directory = Save;
fileDest = fullfile(directory,filename);

File1 = importdata('test_data_1.csv');
File2 = importdata('test_data_2.csv');
File3 = importdata('test_data_3.csv');
File4 = importdata('test_data_4.csv');

f = File1(:,1);




S11Real = File1(:,2);
S11Imag = File2(:,2);
S21Real = File3(:,2);
S21Imag = File4(:,2);

s11 = S11Real + i*S11Imag;
s21 = S21Real + i*S21Imag;

%%% Constitutive Parameters based on HFSS's Model %%%%%%%%%%%%%%%%%%%%

c=3e8;
lamda=c./f;
fc=c/(2*a);
chi=(s11.^2-s21.^2+1)./(2.*s11);
rho=chi+sqrt(chi.^2-1);
rho(abs(rho)>1)=chi(abs(rho)>1)-sqrt(chi(abs(rho)>1).^2-1);
prop=(s11+s21-rho)./(1-(s11+s21).*rho);
n=floor(abs(mean(diff(unwrap(angle(prop))))*f(1)/(diff(f(1:2))*2*pi)));
prop=(real(-log(prop))+1i*(unwrap(imag(-log(prop)))+n*2*pi))/d;
mu=((1+rho)./(1-rho)).*prop.*c./(2*i*pi.*f.*sqrt(1-(fc./f).^2));
ep=((fc./c).^2-(prop/(2*pi)).^2).*lamda.^2./mu;
```

```
f = f/(1e9);

%header = {'Freq (GHz)'; 'Epsilon';'Mu';'S11';'S21'};

%data = [f ep mu s11 s21];
datTable = table(f,ep,mu,s11,s21);


writetable(datTable,fileDest,'WriteRowNames',true);

f = f';
mu = mu.';
ep = ep.';
 end
```

## .2   Anisotropic NRW Code

```
        function [frequency,mu,epsilon] = labview_test_function(file,d)

% Path
% C:\VNA\S2VNA\CSV
%  file = 'test_data_broadside';

file_1 = file + "_1.csv";
file_2 = file + "_2.csv";
file_3 = file + "_3.csv";
file_4 = file + "_4.csv";

% d=(2.3)*1e-3;

M1 = importdata(file_1);
M2 = importdata(file_2);
M3 = importdata(file_3);
M4 = importdata(file_4);

f = M1(:,1);

c=3*power(10,8);
Lamda=(c./f);
K=(2*pi)./Lamda;

Pb=K*d;
 p=exp(-1i*Pb);
% p = 1;
```

```
s11=(M1(:,2)+1i*M2(:,2));
s21=p.*(M3(:,2)+1i*M4(:,2));
c=3*power(10,8);
Lamda=(c./f);
K=(2*pi)./Lamda;

f1=f.*1e-9;
% figure; % Plot the logarithmic magnitudes of
% plot(f1,20*log10(abs(s11)),'-b','LineWidth',2.5)
% hold on
% plot(f1,20*log10(abs(s21)),'-b','LineWidth',3)
% legend('Measured','Simulated');
% legend1 = legend('show');
% set(legend1,...
%     'FontSize',20,...
%      'FontName','Times New Roman');
% grid on
% axis([7 8 -40 0]);
zNumerator=((1+s11).^2-(s21.^2));
zDenomenator=((1-s11).^2-(s21.^2));
zNumDen=zNumerator./zDenomenator;
% zNumDen=transform(zNumDen);
z=sqrt(zNumDen);


nNumerator=(1-s11.^2+s21.^2);
nDenomenator=(2*s21);
alpha=nNumerator./nDenomenator;
% alpha=transform(alpha);
n=(1./(K*d)).*acos(alpha);

epsilon=n./z;
mu=n.*z;

epsilon = epsilon.';
mu = mu.';
% figure;
% plot(f1,real(epsilon),'-b','LineWidth',2.5);
% hold on
% plot(f1,imag(epsilon),'-.k','LineWidth',3);
% legend('Re(\epsilon)','Im (\epsilon)');
% legend1 = legend('show');
% set(legend1,...
%      'FontSize',20,...
%      'FontName','Times New Roman');
```

```
% grid on
% axis([7 8 -5 5]);
% figure();
% plot(f1,real(mu),'-b','LineWidth',2.5);
% hold on
% plot(f1,imag(mu),'-.k','LineWidth',3);
% legend('Re(\mu)','Im (\mu)');
% legend1 = legend('show');
% set(legend1,...
%     'FontSize',20,...
%     'FontName','Times New Roman');
% grid on
% axis([7 8 -1.5 1.5]);
% A=[f1 real(epsilon) imag(epsilon)];
% xlswrite('ep_rohacell',A);
% B=[f1 real(mu) imag(mu)];
% xlswrite('mu_rohacell',B);


% eps = epsilon.*mu;
frequency = f1';
 end
```